



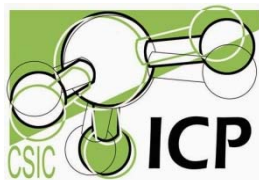
UNIVERSIDAD AUTÓNOMA DE MADRID
FACULTAD DE CIENCIAS
Dpto. de QUÍMICA FÍSICA APLICADA

Physical and chemical destabilization of ammonia borane for an
improved hydrogen storage system

Desestabilización de borano de amoníaco por métodos físicos y
químicos: hacia un mejor sistema de almacenamiento de hidrógeno

MEMORIA

Para aspirar al grado de
DOCTOR EN CIENCIAS QUÍMICAS
con Mención Doctor Internacional



MARIA JOSÉ VALERO PEDRAZA
Instituto de Catálisis y Petroleoquímica (CSIC)
Madrid, 2015

MARIA JOSÉ VALERO PEDRAZA

Physical and chemical destabilization of ammonia borane for an improved hydrogen storage system

Desestabilización de borano de amoníaco por métodos físicos y químicos: hacia un mejor sistema de almacenamiento de hidrógeno

MEMORIA

Para aspirar al grado de

DOCTOR EN CIENCIAS QUÍMICAS

con Mención Doctor Internacional

Dirigida por

Prof. Dr. Miguel Ángel Bañares González

Profesor de Investigación

Instituto de Catálisis y Petroleoquímica (CSIC)

Dr. Ángel Martín Martínez

Profesor

Universidad de Valladolid

UNIVERSIDAD AUTÓNOMA DE MADRID

FACULTAD DE CIENCIAS

Dpto. de QUÍMICA FÍSICA APLICADA

Madrid, 2015

Summary

The worldwide energy demand, estimated to be 10,000 million tonnes oil equivalent is currently covered in more than 87 % by fossil fuels such as coal, petroleum or natural gas. This strong dependency brings economic and environmental impacts and is not sustainable in the long term. Therefore, public institutions point to a necessary and controlled transition towards a clean, reliable and safe energy structure. One of the possible alternative is electrical combustion of hydrogen used as an energy vector in fuel cells. But for such transition to the so called “hydrogen economy” to be achieved, the challenge of finding efficient ways to store and deliver hydrogen to mobile devices has to be solved as; due to its low energy density, huge volumes of hydrogen would be necessary to feed high energy consuming processes. One of the most promising approaches in this sense is the solid storage of hydrogen using complex hydrides of light elements among which aminoboranes ($R(NH_2BH_3)_n$).

Up to now, ammonia borane stands as the most intensively studied compound from this group due to its high stability, easy handling and considerable hydrogen density. But ammonia borane decomposition also exhibits some drawbacks as its excessive exothermicity that hampers regeneration of the residue thus impeding reversibility of the process; low kinetics at the working temperature for fuel cells (85 °C) and the concomitant release of volatile impurities simultaneous to hydrogen as are ammonia, diborane or borazine which are highly undesirable because they can poison the catalyst from fuel cell electrodes.

But despite these hurdles, ammonia borane still remains a promising alternative for hydrogen reversible storage on account of its impressive safety features and high hydrogen content of 19.6 wt.%. Furthermore, ammonia borane offers the combination of hydridic B-H and protonic N-H bounds enclosed in the same molecule thus appearing considerably destabilized compared to the amide parent compound. Thus, many recent studies focused on reducing the decomposition temperature, improving kinetics of hydrogen release while minimizing borazine desorption during ammonia borane thermal decomposition. Some interesting works showed that hydrides with nanosized particles exhibit significantly improved kinetics properties for reversible hydrogen storage when compared to the neat material. In this context, one of the most promising approaches consists in confining ammonia borane in porous materials to reduce its particles size and fine tune thermodynamics and kinetics of thermal decomposition.

The research group in which this thesis work was carried out is strongly experienced in temperature programmed *in-situ* Raman studies with online analysis of released gases by mass spectrometry (MS) conforming the so-called *operando* Raman-MS system. Such studies allow following details of the structural evolution of the material under working conditions (*in-situ* Raman spectroscopy) simultaneously to the detection of hydrogen and volatiles release (online mass spectrometry), thus performing a real-time study of structure/activity relationship.

This Thesis focuses on the study of compounds based on ammonia borane for solid hydrogen storage by means of the *operando* Raman-MS technique, among others. This is a novel approach for investigating aminoboranes decomposition processes.

In a first part of the study, the effect of confining ammonia borane onto the pores of several porous materials such as mesoporous silica and metal oxides was investigated. Samples of ammonia borane impregnated into materials offering different porosities and compositions applying different loading levels on one the support were prepared and characterized thus evaluating both the effects of porosity and ammonia borane loading level. Previously, the effect of the solvent used during the incipient wetness impregnation to support ammonia borane on the porous materials is evaluated. It was demonstrated that recrystallization of ammonia borane from different solvents produces small morphological variations, but without changes in structural properties. The *operando* Raman-MS results corroborated a nucleation and growth mechanism for ammonia borane decomposition samples.

Several characterization techniques were used to evaluate the confinement of ammonia borane in the pores of the supports and to detect possible changes in thermodynamics of ammonia borane decomposition when impregnated to thus check which porous material can decrease dehydrogenation temperature to values below 100 °C. Impregnation of ammonia borane onto porous materials has been shown to improve the kinetic performance, but limited by the amount of ammonia borane that can be impregnated in mesoporous Ga₂O₃ as considerable improvement in H₂ desorption properties in terms of lowered temperature and kinetics were observed for the 0.5:1 AB/Ga₂O₃ samples in which decomposition proceeds to a one-step mechanism. The same effects were observed for mesoporous SBA-15 materials for an ammonia borane 1:1 loading level as the porosity of these supports is much more accessible with a higher pores volume to host ammonia borane. All the AB/Ga₂O₃ materials were shown to induce simultaneous NH₃ desorption probably due to interactions between the support surface and ammonia borane particles.

In the second part of this Thesis, another aminoborane compound, ethane 1,2-diaminebisborane ($\text{CH}_2\text{NH}_2\text{BH}_3$)₂, was synthesized and characterized. Hydrogen release features for this compound were quite different from those for ammonia borane as ethane 1,2-diaminebisborane offers a decomposition temperature higher than that of ammonia borane with faster hydrogen release and no concomitant borazine desorption. Several characterization techniques were applied to compare thermodynamics properties of ethane 1,2-diaminebisborane dehydrogenation and ammonia borane. The results show that EDAB presents a thermal stability higher than that of ammonia borane under both, vacuum and inert gas flow. Contrary to this compound, EDAB releases pure hydrogen when heated under inert flow while moderate fractions of diborane, residual tetrahydrofuran, and volatile B-N-C-H species were released under dynamic vacuum. The bonding properties of the reaction products were investigated based on the *operando* Raman-MS and NMR studies of the thermolytic decomposition of EDAB and a reaction scheme was proposed for this process which slightly differs from the one described in the literature.

In the last part of this Thesis, ammonia borane thermal decomposition in various ionic liquids was studied. Ionic liquids are solid salts with low melting temperatures that are even liquid at room temperature in some cases. Besides dissolving ammonia borane, ionic liquids offer low volatility, they are stable at high temperatures, they can be easily recovered with low activity loss and they exhibit an impressive chemical inertia that make of them a suitable environment for controlled thermal decomposition of ammonia borane. It was shown in previous studies on the thermal decomposition of ammonia borane in ionic liquids that they high polarity stabilized diammonate of diborane, the intermediate decomposition compound thus considerably reducing the induction period necessary for this species to be formed during neat ammonia borane decomposition. Besides, hydrogen yield was also enhanced in some of the tested ammonia borane/ionic liquids dissolutions under isothermal conditions close to the working temperature of fuel cells. In this Thesis work, ionic liquids that weren't previously tested were used to dissolve ammonia borane. While most of these dissolutions exhibited similar properties to those previously described in literature, it was seen that by using ionic liquids with bis(trifluoromethylsulfanyl) imide Tf_2N anion, the foaming problem was reduced and in some cases, the residue remained dissolved in the ionic liquid. This is a unique feature, never reported up to now, which may facilitate recycling of the material by rehydrogenation of ammonia borane. It was also observed that some ionic liquids, that contained choline cation (2-hydroxy-*N,N,N*-trimethylethanaminium), showed very high hydrogen yields. This may be caused by ammonia borane thermolysis proceeding through an alternative route which is supported by IR characterization of the residue.

The complete study on dehydrogenation processes for these materials based on ammonia borane should complement the data already available in literature on this trendy and relevant issue in search of a clean alternative to fossil fuels.

Resumen

La demanda energética mundial, estimada en unos 10.000 millones de toneladas equivalentes de petróleo, se ve cubierta en más de un 87% por combustibles fósiles como el carbón, petróleo y gas natural. Esta dependencia tiene importantes repercusiones tanto económicas como ambientales y no resulta sostenible a medio plazo. Se apunta por lo tanto de forma insistente desde las administraciones públicas a la necesidad de preparar una transición controlada hacia una nueva forma de producción y consumo energético que sea limpio, seguro y fiable. Una de las respuestas a esta creciente demanda es el uso de hidrógeno como vector energético y su transformación en electricidad por medio de las llamadas pilas de combustible.

Para una transición hacia la llamada “*economía del hidrógeno*”, uno de los retos más importantes es el almacenamiento/suministro de este vector energético para aplicaciones móviles ya que, debido a su baja densidad energética, se necesitan enormes volúmenes de hidrógeno para alimentar procesos con alta demanda energética. Una de las alternativas más prometedoras es el almacenamiento de hidrógeno en estado sólido usando hidruros complejos de elementos ligeros (los de baja masa atómica) entre los cuales se incluye la familia de los aminoboranos ($R(NH_2BH_3)_n$).

El borano de amoníaco (NH_3BH_3) ha sido hasta ahora el más estudiado de los aminoboranos debido a su elevada estabilidad, fácil manejo y considerables densidades gravimétrica y volumétrica de hidrógeno. Pero la deshidrogenación de este compuesto también presenta una serie de inconvenientes como son su excesiva exotermicidad que dificulta el proceso de regeneración del residuo impidiendo la reversibilidad del proceso; una cinética demasiado lenta a la temperatura de trabajo de la pila de combustible (85 °C) y la liberación de impurezas entre las cuales se cuentan el amoníaco, el diborano y la borazina como productos no deseados que impurifican el hidrógeno obtenido y son susceptibles de dañar el catalizador del ánodo de la pila de combustible.

A pesar de las desventajas descritas arriba, sus características en cuanto a seguridad y su elevado contenido en hidrógeno (19,6 % en peso) hacen del borano de amoníaco un candidato muy atractivo para el almacenamiento reversible de este vector energético. El NH_3BH_3 es además, en el marco de la desestabilización de complejos amidos por combinación de hidrógenos protónicos e hidruro, un compuesto excepcional debido a que coexisten en la

molécula el enlace hidruro B-H y el enlace protónico N-H. Se están llevando a cabo por lo tanto en la actualidad diferentes intentos de reducir la temperatura de deshidrogenación por termólisis del NH_3BH_3 , aumentar su cinética de liberación de hidrógeno y minimizar la emisión simultánea de borazina. Existen trabajos en los que se demuestra que los hidruros metálicos en partículas de tamaño nanoscópico muestran propiedades cinéticas muy buenas para el almacenamiento de H_2 en comparación con el material másico. En este sentido, una de las posibilidades más prometedoras que se han explorado en la mejora de las propiedades de deshidrogenación del NH_3BH_3 consiste en soportarlo sobre materiales porosos para reducir el tamaño de partículas de este hidruro y afinar así la termodinámica y la cinética del proceso.

El grupo dentro del cual se realizó esta tesis doctoral posee una experiencia sólida en estudios Raman *in situ* a temperatura programada con medida en línea de gases liberados por espectrometría de masas (sistema Raman-MS “*operando*”). Estos estudios permiten seguir en detalle la estructura del compuesto reactante en condiciones de operación (espectroscopia Raman *in situ*) de modo simultáneo a la evolución de hidrógeno y volátiles (espectrometría de masas en línea) y así llevar a cabo un estudio en tiempo real de la relación estructura-propiedad del sistema.

El objetivo de esta Tesis es, por lo tanto, el estudio de compuestos basados en NH_3BH_3 para almacenamiento de hidrógeno utilizando como técnica de partida la metodología *operando* Raman-MS. El empleo de esta metodología al estudio de la descomposición de aminoboranos es totalmente novedoso en bibliografía.

En una primera parte de la Tesis, se llevó a cabo un estudio exhaustivo sobre el efecto de confinar NH_3BH_3 en poros de diferentes materiales como sílices y óxidos metálicos mesoporosos. Se prepararon muestras de NH_3BH_3 soportado sobre materiales con estructuras porosas y composiciones variadas utilizando diferentes porcentajes en masa en el caso de uno de los soportes para así evaluar el efecto de la porosidad así como el de la concentración de borano de amoníaco incorporado. Se estudia previamente el posible efecto de varios disolventes susceptibles de ser utilizados durante la técnica de impregnación por humedad incipiente aplicada para confinar el borano de amoníaco en los poros de los soportes probados. Se observó que las muestras de borano de amoníaco recristalizado solo presentaban leves variaciones en la morfología con respecto al compuesto original sin que se detectaran cambios estructurales. La

metodología Raman-MS *operando* permitió además corroborar el mecanismo de inducción y crecimiento para la descomposición térmica de estos materiales.

Se aplicaron diversas técnicas de caracterización para evaluar la localización del borano de amoníaco dentro y fuera de los poros y para detectar posibles cambios en la termodinámica de deshidrogenación del borano de amoníaco soportado y así evaluar qué soportes facilitan, en mayor medida, la liberación de hidrógeno a temperaturas inferiores a 100 °C. La impregnación de borano de amoníaco sobre Ga_2O_3 resultó provocar una mejora considerable en la temperatura y cinética de descomposición del compuesto cuando la carga sobre el soporte era de 0.5:1 en peso, muestras en las cuales este proceso transcurría a través de un mecanismo diferente con una única etapa de deshidrogenación. Resultados similares se obtuvieron en el caso de las SBA-15 mesoporosas cuando la carga de borano de amoníaco sobre soporte ascendía hasta 1:1 debido a su más accesible porosidad con mayor volumen de poros para albergar a este compuesto. Se detectó además liberación de amoníaco simultánea a la de hidrógeno en el caso de las muestras soportadas sobre Ga_2O_3 , probablemente a causa de interacción del borano con el soporte.

En una segunda parte de esta tesis doctoral, se preparó y caracterizó un compuesto derivado del NH_3BH_3 , el etano 1,2-diaminadiborano $(\text{CH}_2\text{NH}_2\text{BH}_3)_2$, que presenta sin embargo propiedades de deshidrogenación muy distintas a las del borano de amoníaco. Su temperatura de descomposición es ligeramente más elevada con una cinética más interesante y sobretudo una liberación de hidrógeno exenta de borazina, su principal contaminante cuando proviene del NH_3BH_3 . Se aplicaron de igual manera varias técnicas de caracterización para comparar las propiedades termodinámicas de deshidrogenación del $(\text{CH}_2\text{NH}_2\text{BH}_3)_2$ con las del borano de amoníaco. Se observó de esta manera que el EDAB es más estable que el borano de amoníaco tanto bajo vacío dinámico como bajo atmósfera inerte. En estas condiciones, el EDAB emite un hidrógeno más puro que el borano de amoníaco mientras que bajo vacío dinámico libera fracciones de diborano, tetrahidrofurano y especies B-N-C-H volátiles. Se estudió la estructura del residuo de descomposición del EDAB por RMN y Raman-MS *operando* y los resultados permitieron proponer un mecanismo alternativo al descrito anteriormente en bibliografía.

Por último, se estudió la descomposición del borano de amoníaco en disoluciones de diferentes líquidos iónicos con variadas propiedades físicas. Los líquidos iónicos son sales iónicas con bajo

punto de fusión hasta ser líquidas a temperatura ambiente en algunos casos y que, además de la capacidad de disolver el NH_3BH_3 , presentan baja volatilidad, estabilidad a altas temperaturas, posibilidad de reciclar con baja pérdida de actividad y una gran inercia química que les hacen muy interesantes como medio para descomposición térmica de NH_3BH_3 controlada. Estudios previos sobre descomposición térmica de borano de amoníaco disueltos en líquidos iónicos demostraron que la elevada polaridad de estos compuestos estabiliza el diamoniato de diborano, compuesto intermedio de descomposición reduciendo así el tiempo de inducción necesario para la formación de esta especie intermedia durante la descomposición del borano de amoníaco sólido además de aumentar en algunos casos el rendimiento en hidrógeno obtenido en condiciones isothermas cercanas a las de trabajo de la pila de combustible.

En esta tesis doctoral, además de estudiar el efecto de líquidos iónicos no probados con anterioridad, se estudian dos mecanismos de descomposición del borano de amoníaco que se dan dependiendo del líquido iónico utilizado y que justifican las diferencias observadas en el rendimiento de hidrógeno desorbido del borano de amoníaco. La mayoría de estas disoluciones exhibían efectos muy similares a los previamente descritos en bibliografía pero se observó que en el caso de líquidos iónicos con el anión bis(trifluorometilsulfanil) imido se reducía la formación de espumas y en algunos casos el residuo seguía incluso solubilizado en el líquido iónico. Este efecto no había sido descrito hasta el momento en bibliografía y abre la posibilidad de reciclar el material por rehidrogenación del borano de amoníaco. También se detectó que en el caso de líquidos iónicos que contienen el catión colina (N,N,N-trimetiletanolamonio), se obtenía un rendimiento de hidrógeno considerablemente más elevado que en el resto de disoluciones. Esto se debe probablemente a que la descomposición térmica del borano de amoníaco en estas disoluciones transcurre a través de un mecanismo diferente lo cual se ve corroborado con lo observado por caracterización con IR del residuo.

Este exhaustivo estudio de la deshidrogenación de compuestos derivados del borano de amoníaco complementará los datos ya disponibles en bibliografía para un tema de investigación de candente actualidad y gran relevancia en la búsqueda de combustibles limpios como alternativa a los combustibles fósiles.

1.1 Current dependence on fossil fuels and its challenges

The current energy demand is almost entirely satisfied with fossil fuels, whose reserves are increasingly limited and concentrated in few countries. This dependence leads to economic and political problems. There is a real battle for oil going on as the US and western Europe's countries dependency on oil imports is increasing while developing countries such as China or India compete in the race for resources. Currently, the Middle East is the world's fueling station just as worldwide consumption of energy continues to rise while global production of energy struggles to keep pace. Figure 1.1 illustrates such unequally distributed worldwide petroleum production.

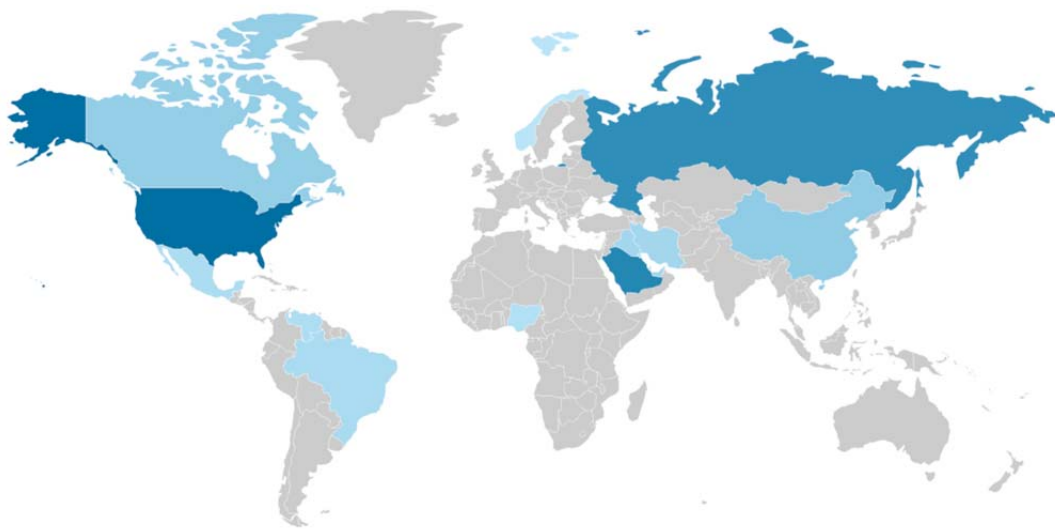


Figure 1.1 Distribution of petroleum worldwide production in 2014 [1]

Most of the energy consumed is used in the form of electric power. However, the second largest consumption sector is transportation and energy sources used for transportation include, petroleum, natural gas, and biofuels with 95 % of the consumed energy proceeding from petroleum. Domestic production, the third largest energy consumption sector, also mostly relies on crude oil. Therefore, importation of petroleum has increased to balance consumption demands. Most of the petroleum (71 %) is used in the transportation sector, mostly for light vehicles (i.e. cars and light trucks) [1] and such strong dependency of transport sector on petroleum supply is illustrated in Figure 1.2. Oil reserves will inevitably run out and fuel prices will continue to rise. To match current and future energy needs, a new energy carrier is needed.

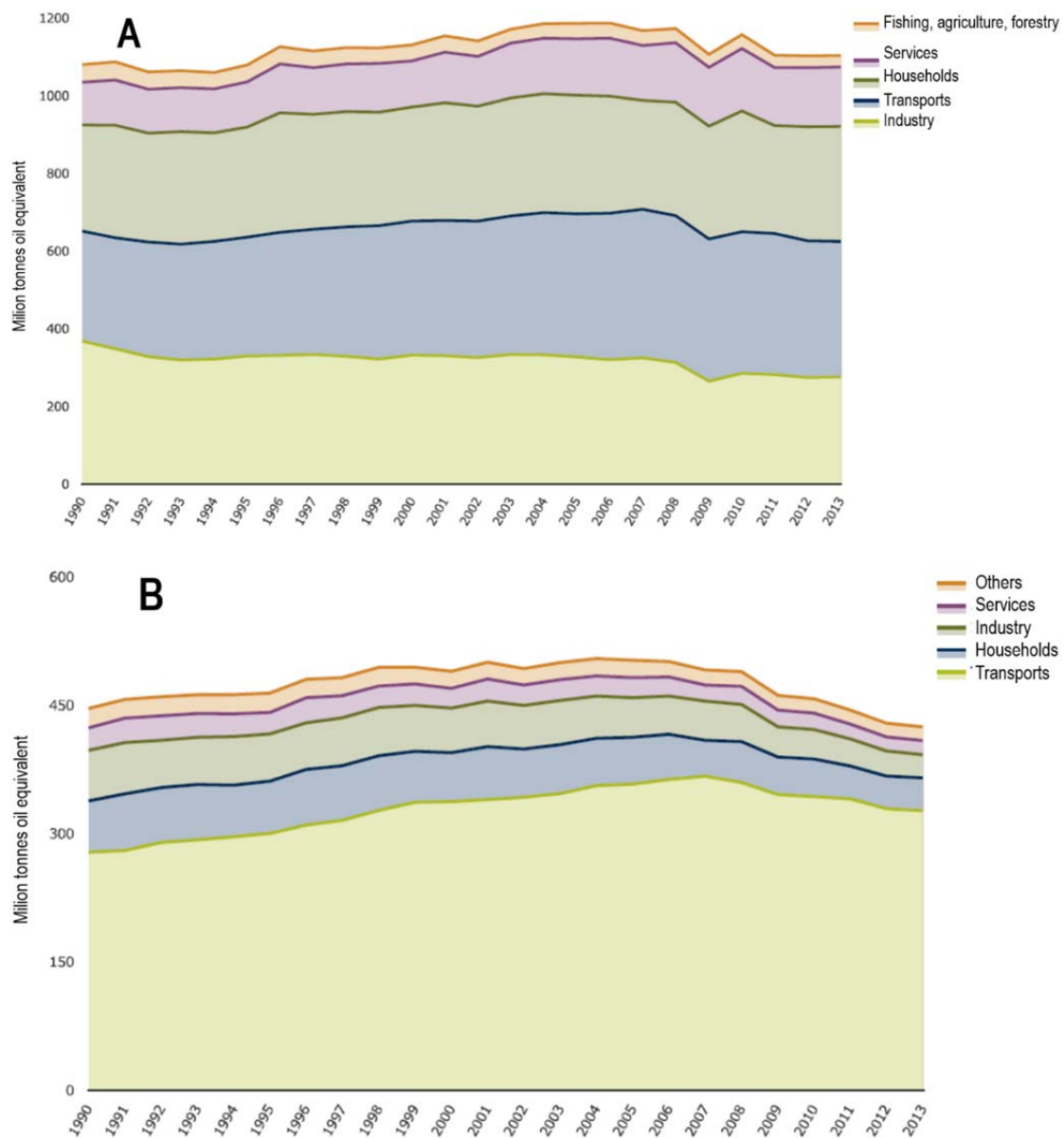
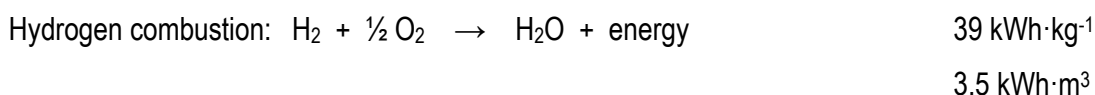


Figure 1.2 Final energy consumption (A) and final energy consumption from petroleum (B) by sector in Europe between 1990 and 2013 [2]

But there are also environmental issues due to the use of fossil fuels and specifically, due to the use of petroleum as a transportation energy carrier as it contributes on global warming caused by the CO₂ produced by petroleum combustion and the unstable energy supply as they represent the main source of greenhouse gases. Increasing environmental problems, limited fossil resources and the geopolitical dependence on crude oil are enormous challenges for our societies and it is then necessary to carry out a transition towards alternative fuels that can provide energy without pollution to solve energy shortage [1,2]. A broad basis of energy technologies focused on energy savings, efficient conversion or advanced transmission and distribution is needed combined with a balanced mix of energy sources to ensure that energy

In the next section, the many benefits of utilization of hydrogen as an energy carrier instead of petroleum will be discussed.

Hydrogen is the most abundant element in the universe and hydrogen molecule, the richest one in energy per unit mass. Hydrogen gravimetric energy capacity largely exceeds that of gasoline while H_2 volumetric density is far below the gasoline one. However, hydrogen is hardly present on Earth in its molecular form. It doesn't contain any carbon and, as long as its production doesn't involve fossil fuels in any step, it won't produce any greenhouse gas. Specifically, it can act as a clean and efficient carbon-free energy vector between renewable energy sources and final energy users, without generation of pollution as its combustion produces only water and energy [3,4].



Fuel cells used in stationary applications (i.e. for residential energy and industrial application) will use different fuels and convert them into hydrogen in situ as long as there is no hydrogen infrastructure in place. In the case of mobile applications, the more extended device is the Proton Exchange Membrane (PEM) fuel cell which schematic diagram is depicted in Figure 1.3. PEM fuel cells operate by oxidizing molecular hydrogen and allowing the protons to migrate through

the membrane while the electrons are shuffled out to do work by the catalytic electrodes. The protons recombine on the other side of the membrane with reduced molecular oxygen, typically from the air, to form water [5] as shown in the half reactions next:

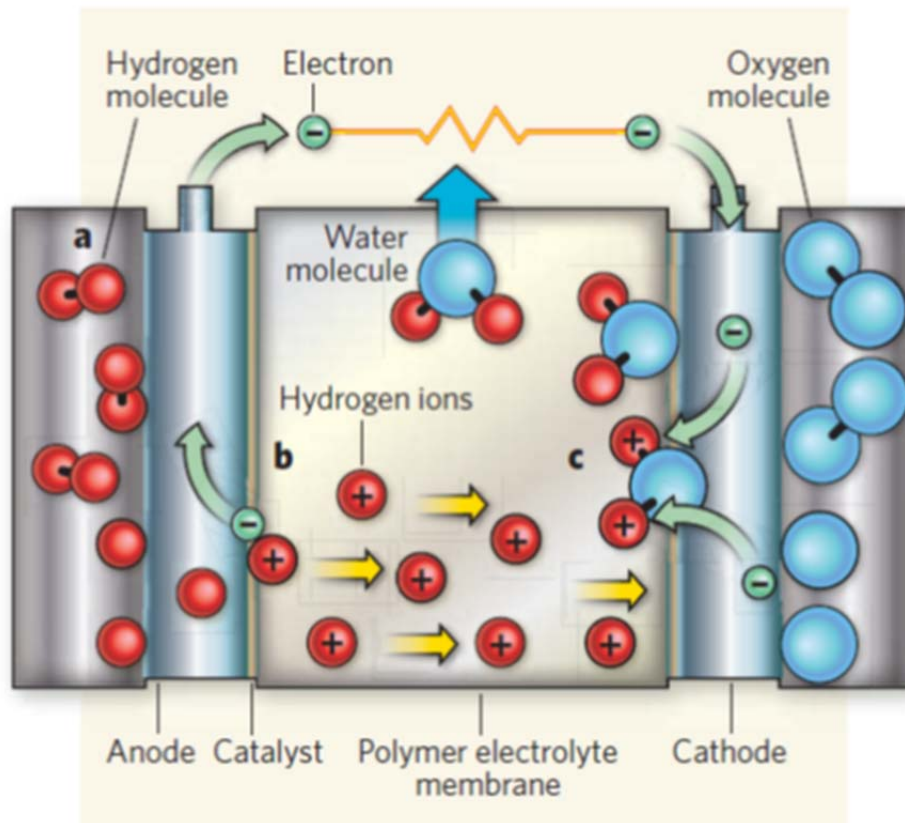
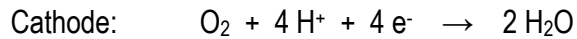
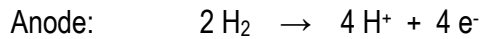


Figure 1.3 Schematic diagram of a PEM fuel cell [4]

Fuel cells have two to three times the efficiency of internal combustion engines and can be designed to power a broad spectrum of sizes of applications from a watch to a building. The benefits of the H_2 -fuel cells technology consists of higher efficiencies and zero-emissions. Fuel cells have the potential to produce excellent solutions to the ecological and economic problems provided that their development is pursued in a determined way and that their market launch is prepared. The term 'hydrogen economy' is commonly used to refer to this approach based on the generation of power not by direct combustion of fossil fuels or by nuclear fission, but by electrochemical oxidation of hydrogen in a fuel cell device. Many governmental programs focused on improving this new technology appeared in the last 15 years, one of the most famous one being that announced by President George W. Bush in 2003. The ultimate goal was to make

fuel cell powered cars competitive by 2020. In order to accomplish this goal, the hydrogen economy must be as good, if not better, than the current hydrocarbon based energy economy. However, as long as the advantages of hydrogen as a secondary energy carrier and of related technologies consist of benefits to the society instead of being determined by customer requirements, it will be difficult to establish a hydrogen economy competing with the electricity, natural gas and oil economy. In this respect, technology development seems to be the key.

There are many barriers to implementing a hydrogen economy. The biggest overarching difficulty is in replacing an energy system that has been in place for one hundred years. Gasoline is an excellent energy carrier with a high energy density, it is easy to transport and handle and inexpensive for now. Gasoline has the added benefit of one hundred years of optimization and infrastructure that hydrogen will have to overcome. Hydrogen is expected to replace this type of system in a short period of time (a few decades). The difficulties in implementing a hydrogen economy can be broken down into three areas: hydrogen production, hydrogen delivery, and hydrogen storage.

1.2.1 Hydrogen production

Hydrogen needs to be produced cost-effectively and with zero CO₂ emissions. Most hydrogen (95%) is currently produced from natural gas reforming via high temperature steam following the equation given next where steam at temperatures from 700 °C to 1000 °C split the methane into carbon monoxide and hydrogen. Another option to produce hydrogen from fossil energy carriers is coal gasification in which the gas produced is converted in to H₂ and CO₂ through steam reforming.

Natural gas reforming: $\text{CH}_4 + \text{H}_2\text{O} \rightarrow \text{CO} + 3 \text{H}_2$

If hydrogen is produced from hydrocarbons or other fossil fuels like coal, then we are still relying on geographically concentrated sources, quickly depleting hydrocarbon fuel sources, and producing large amounts of carbon monoxide. Other production methods are necessary in order to create an environmentally friendly, secure hydrogen energy supply. This is where carbon capture and storage (CCS or CO₂ sequestration) technology comes in to play. CCS is a technology that is primarily being developed for electricity generation in zero-emission power plants. At the same time, however, CCS can serve to produce an array of products, such as synthesis gas, synthetic natural gas as well as hydrogen. Indirect production of hydrogen through

electricity and electrolysis is another option. This one, however, involves heavy efficiency penalties and will only be suitable for a large market if electricity costs are low enough. The approaches of water splitting (with nuclear or solar technologies) and advanced biological processes (photo-biological production) are still in a low advancement state so that reliable statements on a potential future commercial deployment are difficult. However, they still have the potential of a direct CO₂ emission-free hydrogen production from renewables or nuclear energy without any detour over electricity. Therefore intensive research into these methods is going on. These alternative hydrogen production routes are gathered in Figure 1.4.

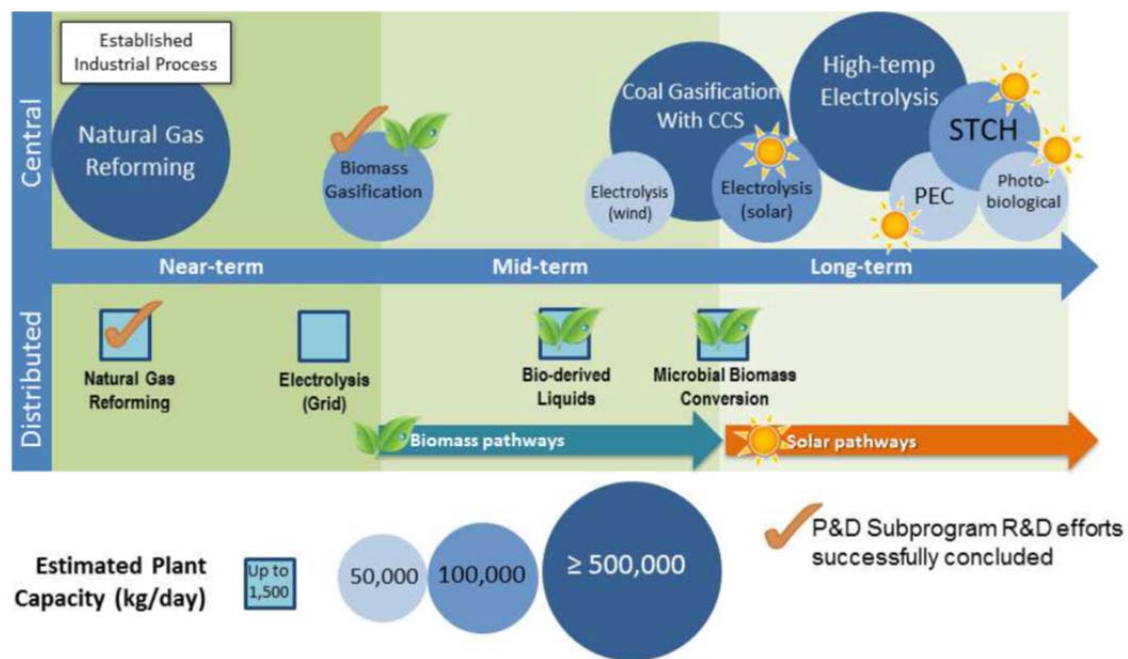


Figure 1.4 Hydrogen production technologies [6]

1.2.2 Hydrogen delivery

A viable hydrogen infrastructure requires that hydrogen be able to be delivered from where it's produced to the point of end-use, such as a dispenser at a refueling station or stationary power site. Infrastructure includes the pipelines, trucks, storage facilities, compressors, and dispensers involved in the process of delivering fuel. The problems with delivery center around what sort of infrastructure for hydrogen delivery would be needed. The existing pipelines used for moving petroleum do not work for gases. Some of the infrastructure is already in place because hydrogen has long been used in industrial applications, but it's not sufficient to support widespread consumer use of hydrogen as an energy carrier [5]. In theory, with renewable sources producing hydrogen, local fuel stations or even individuals could produce their own hydrogen. However,

depending on the hydrogen storage method used in vehicles, central processing plants may be needed and therefore transportation of gas or solid fuels would be necessary. Where the hydrogen is produced can have a big impact on the cost and best method of delivery. For example, a large, centrally located hydrogen production facility can produce hydrogen at a lower cost because it is producing more, but it costs more to deliver the hydrogen because the point of use is farther away. In comparison, distributed production facilities produce hydrogen on site so delivery costs are relatively low, but the cost to produce the hydrogen is likely to be higher because production volumes are less. Currently, hydrogen is transported from the point of production to the point of use via pipeline, over the road in cryogenic liquid tanker trucks or gaseous tube trailers, or by rail or barge. Hydrogen used in portable or stationary applications can be delivered by truck to a storage facility or in cylinders, similar to the propane used for gas grills, or in cartridges that would resemble a battery. Hydrogen used in FCEVs is dispensed very much the way gasoline is. Drivers pull into a filling station, connect the dispenser to the vehicle, fill, disconnect, pay, and then drive away with a full tank. But the type of delivery system is heavily dependent on the storage method used. Therefore, hydrogen storage and delivery remains a very challenging technical and economic issue to be resolved [5,7]. Key challenges to hydrogen delivery include reducing delivery cost, increasing energy efficiency, maintaining hydrogen purity, and minimizing hydrogen leakage. Further research is needed to analyze the trade-offs between the hydrogen production options and the hydrogen delivery options when considered together as a system.

1.2.3 Hydrogen storage

Compact, light, safe and affordable containment is a critical feature for on-board energy storage [8,9]. As already stated and shown in Figure 1.5 next, hydrogen has the highest energy per mass of any fuel however its low ambient temperature density results in a low energy per unit volume, therefore requiring the development of advanced storage methods that have potential for higher energy density. There are three main methods currently being explored for storing hydrogen for transportation purposes. The first utilizes high pressure storage tanks which have a large number of benefits. Simplicity in the overall system is the biggest benefit and compressed gaseous hydrogen is the most mature hydrogen storage technology. Using a high pressure tank delivery system in the vehicle is much simpler since the fuel is stored in the form in which it is ultimately consumed and the fuel can be transferred in the same form. There are of course drawbacks to this approach mainly due to the pressure required to make these tanks practical. Heavy and

massive storage tanks made of expensive materials are also necessary and the compression process is costly. Storage of hydrogen as a gas typically requires high-pressure tanks ranging from 350 bar to 700 bar and large-volume systems which is less of an issue for stationary applications, where the footprint of compressed gas tanks may be less critical.

A second method for storing hydrogen is in the liquid phase which gives much lower pressures for storage, as well as a higher energy density (see Figure 1.5). However, the boiling point of hydrogen at one atmosphere pressure is only of -252.8°C and so cryogenic temperatures are required for liquid hydrogen storage making this technology impractical due to considerable evaporation losses. Storage of hydrogen as a liquid also implies higher energy costs necessary to liquefy hydrogen (around 30% of the initial energy content) and the cryogenic tanks required to maintain it as a liquid. For these reasons, the energy input is greater than the efficiency gained by a higher energy density.

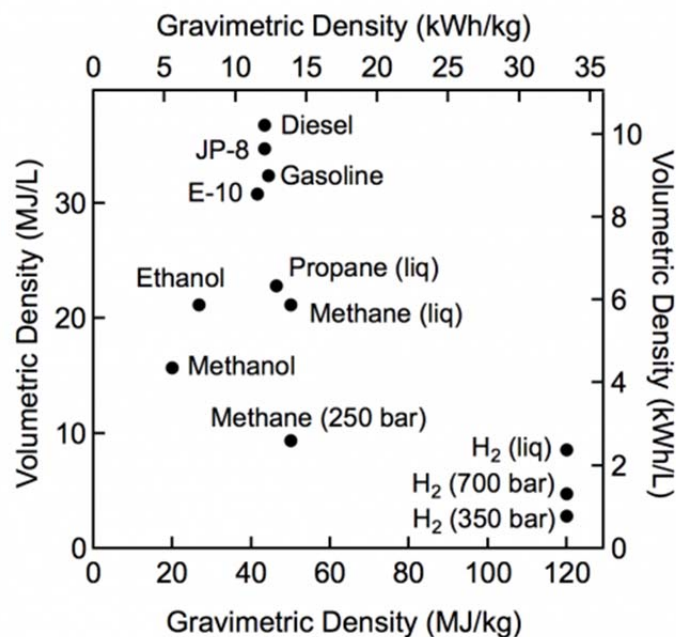


Figure 1.5 Comparison of specific energy (gravimetric density) and energy density (volumetric density) for several fuels based on lower heating values [6]

The third storage method for hydrogen consists of using solid materials containing hydrogen that may be able to store it reversibly by adsorption or absorption mechanisms. These materials can reach a higher energy density for H₂ storage than that achieved by either gas or liquid hydrogen tank systems. Three main groups of materials are considered; reversible metal hydrides, chemical hydrogen storage materials and hydrogen sorbent systems. The two first categories are based on hydrogen absorption processes while hydrogen sorbent systems obviously rely

on adsorption processes. Some examples of reversible metal hydrides include materials such as lithium aluminum hydride and lithium hydride [10]. Hydrogen sorbent systems specially focus on carbon-based adsorption materials as are carbon nanotubes and metal-organic frameworks (MOFs) [11,12]. Because of their high material weight percent, chemical hydrogen storage has mainly focused on boron hydrides, including compounds such as sodium borohydride, ammonium borohydride or ammonia borane (AB) [13,14].

High density hydrogen storage is a challenge for mobile applications and especially in the case of light-duty FCEV. The Fuel Cell Technologies Office (FCTO) is in charge of developing a hydrogen storage technology to meet the DOE requirement for fuel-cell-powered vehicles with enough hydrogen to provide a driving range of more than 300 miles with the ability to quickly and easily refuel the vehicle [6]. Onboard hydrogen storage capacities ranging from 5 kg to 13 kg will then be necessary. The low energy densities of physical hydrogen storage (that is, under gaseous and liquid form) are unlikely to overcome these challenges due to the excessive volumes and/or pressures needed and FCTO is pursuing a strategy in the long-term that focuses on materials-based hydrogen storage technologies with higher energy density having potential to meet the DOE hydrogen storage targets.

The 300 miles driving range DOE target implies further goals to be met as well and that are summarized in Table 1.1. It is important to clarify that the total system weight percent is the weight of hydrogen produced, divided by the weight of the fuel system including tanks, heaters, tubing, release compound and solvents. On the other hand, materials weight percent, is just the weight of hydrogen released divided by the weight of the compound system (including possible solvent and catalyst) doing the release. To achieve a target total system weight percent, the material weight percent must be much higher so that additional weight for tanks, etc. can be factored in.

Other important requirements set by the DOE for hydrogen-based systems are that they operate over the wide variety of environments in which gasoline operates. Fuel cell systems must work in -20 °C temperatures and survive -40 °C, while not breaking down at temperatures that exceed 50 °C. It is also essential to consider the safety aspect of onboard hydrogen storage considering that the higher the pressure being stored, the more dangerous tank imperfections are. Thus, solid-state hydrogen storage shows several advantages in terms of storage capacity, safety and costs as hydrogen in these materials is presently a safer fuel than its compressed gas or liquid counterpart.

Table 1.1 DOE Technical system targets: onboard hydrogen storage for light-duty fuel cell vehicles [6]

Storage Parameter	Units	2020	Ultimate
System Gravimetric Capacity: Usable, specific-energy from H ₂ (net useful energy/max system mass) ^b	kWh/kg (kg H ₂ /kg system)	1.8 (0.055)	2.5 (0.075)
System Volumetric Capacity: Usable energy density from H ₂ (net useful energy/max system volume) ^b	kWh/L (kg H ₂ /L system)	1.3 (0.040)	2.3 (0.070)
Storage System Cost : • Fuel cost ^c	\$/kWh net (\$/kg H ₂) \$/gge at pump	10 333 2-4	8 266 2-4
Durability/Operability: • Operating ambient temperature ^d • Min/max delivery temperature • Operational cycle life (1/4 tank to full) • Min delivery pressure from storage system • Max delivery pressure from storage system • Onboard Efficiency ^e • "Well" to Powerplant Efficiency ^e	°C °C Cycles bar (abs) bar (abs) % %	-40/60 (sun) -40/85 1500 5 12 90 60	-40/60 (sun) -40/85 1500 5 12 90 60
Charging / Discharging Rates: • System fill time (5 kg) • Minimum full flow rate • Start time to full flow (20°C) • Start time to full flow (-20°C) • Transient response at operating temperature 10%–90% and 90%–0%	min (kg H ₂ /min) (g/s)/kW s s s	3.3 (1.5) 0.02 5 15 0.75	2.5 (2.0) 0.02 5 15 0.75
Fuel Quality (H₂ from storage)^f:	% H ₂	SAE J2719 and ISO/PDTS 14687-2 (99.97% dry basis)	
Environmental Health & Safety: • Permeation & leakage ^g • Toxicity • Safety	- - -	Meets or exceeds applicable standards	
Loss of useable H₂^h	(g/h)/kg H ₂ stored	0.05	0.05

^f Useful constants: 0.2778 kWh/MJ; Lower heating value for H₂ is 33.3 kWh/kg H₂; 1 kg H₂ ≈ 1 gal gasoline equivalent (gge)

1.3 Solid hydrogen storage

Solid hydrogen storage requires materials with an optimum hydrogen gravimetric density, ease of hydrogen evolution in terms of moderate temperature decomposition and acceptable kinetics and reversibility of this process. Considering these requirements, many solid materials that can store hydrogen have been tested for reversibility [10,13,14].

Hydrogen sorbent materials have high porosity and hydrogen is stored by physisorption mechanism, in which the gas molecules accumulate at the surface of the material, but don't react chemically with it. The most extensively studied for storage purposes are carbon materials including carbon nanotubes [11,15] and (MOFs) [12,16,17] although some others have also been investigated. This is the case of inorganic nanowires and nanotubes of boron nitride (BN),

titanium disulfide (TiS_2) and molybdenum disulfide (MoS_2) [18]; polymers with intrinsic microporosity (PIMs) [19–21], clathrates [22–23] and zeolites [24]. In these materials, hydrogen is stored by different physical mechanisms like encapsulation in clathrates where it can be released by changing the pressure or temperature [23] or simple adsorption in PIMs, which are formed either by polymerisation of monomers or by cross-linking of polymeric gels, due to their microporosity which gives rise to a large surface area and low density material [19,20]. All these materials generally show very good reversibility, but the higher storage capacity is realized only at low temperatures ($-196\text{ }^\circ\text{C}$) and/or elevated pressures, due to the weak nature of interaction with hydrogen, which is far beyond the operational temperature of PEM fuel cells and so considerable improvements are needed for these systems to be operational for FCEV devices.

Certain metals, alloys and other compounds store hydrogen using chemisorption. In this process, hydrogen molecules react with the surface of the material dissociating into hydrogen atoms. Initially, the hydrogen atoms adopt random locations in the host material but eventually form metallic, covalent or ionic bonds with the metal atoms to yield a hydride compound, in which the hydrogen atoms adopt a regular arrangement [25].

Hydrogen reacts with many materials, mainly metals or alloys to form hydrides that can be used as hydrogen storage media. The reactions are often fast and reversible at practically accessible temperatures ($20\text{--}100\text{ }^\circ\text{C}$), so that large amounts of hydrogen can be absorbed and then recovered. Several kinds of materials as hydrides of elemental metals (Pd, Th); hydrides of compounds with the formula AB_5 (where A and B are usually metals such as lanthanum and nickel) (LaNi_5H_6) and complex hydrides such as barium–rhodium hydride (BaRhH_9) have been extensively studied for hydrogen storage [26]. These materials easily reach hydrogen-volume densities far above that of liquid hydrogen, and can be recharged several tens of thousands of times. But because the host materials are not light, the quantity of hydrogen stored has not exceeded 4 % by mass and most of these compounds aren't practically useful for mobile hydrogen storage, as their hydrogen storage capacities per unit mass are either too small or the temperatures required to release stored hydrogen are too high [13,14]. Taking into account gravimetric density requirements (5.5 wt% according to revised DOE targets in Table 1.1) one can easily limit attention to the elements of the first three periods of the periodic table (Li, B, Na, Mg, Al). Lighter elements chemical hydrides can deliver hydrogen contents higher than 8–20 wt.% desorbing it at temperatures ranging from $80\text{ }^\circ\text{C}$ up to $600\text{ }^\circ\text{C}$. Solid-state storage using complex

hydrides of light elements like alanates (which contain AlH_4^- anions), borohydrides (which contain BH_4^- anions), amide hydrides (which contain N-H groups) or aminoboranes (which contain the NH_2BH_3^- anion) are currently under study [13,14].

1.4 Amine-boranes as hydrogen storage materials

In this context, amine-boranes have been considered as interesting candidates as hydrogen storage material owing to their high hydrogen densities that can reach 24.5 wt.% or 19.6 wt.% in the case of ammonium borohydride (NH_4BH_4) and ammonia borane (NH_3BH_3 , AB) respectively. These materials are often considered as inorganic analogues of hydrocarbons but the different electronegativities of B and N trigger the formation of protonic N-H and hydridic B-H hydrogens that form stronger intermolecular interactions. This phenomenon makes a considerable difference as these compounds are solids rather than gases at ambient temperature and they offer far more favorable volumetric densities than hydrocarbons. Ammonium borohydride is the compound with the highest hydrogen density but its use as hydrogen storage material is hampered by its instability as this material evolves hydrogen slowly at temperatures above -40°C [27]. Ammonia borane is a far more promising candidate as it is a stable solid at room temperature and requires external heating to release H_2 [28,29,30].

Crystalline AB was first synthesized by Parry and Shore in 1955 who separated it from its ionic dimer, diammonate of diborane ($\text{DADB}, [\text{BH}_2(\text{NH}_3)_2]^+ \text{BH}_4^-$) based on AB higher solubility in ether [31]. They kept on studying both compounds until finding out the correct structures of AB and DADB [32]. Figure 1.6 next shows the solid-state structure of AB.

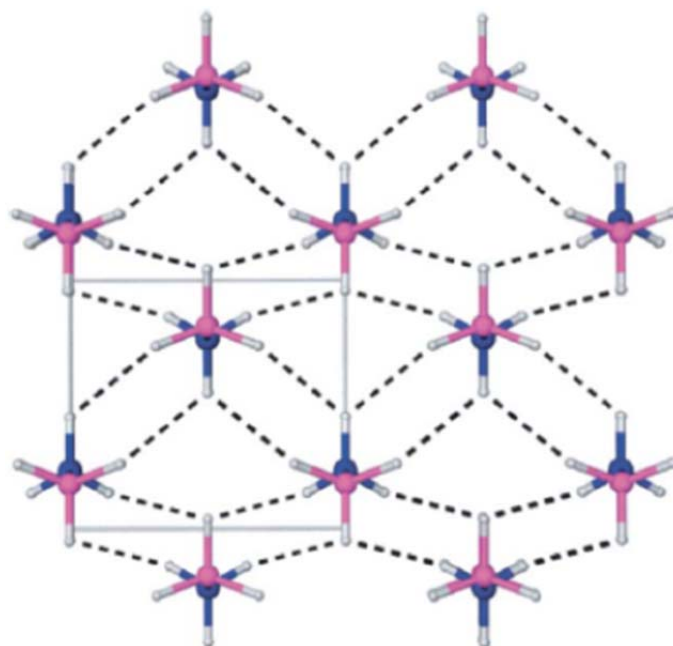
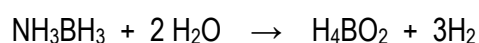


Figure 1.6 orthorhombic crystal structure of AB (up to -48 °C). Nitrogen, boron, and hydrogen atoms are depicted in blue, purple, and gray, respectively [33]

Ammonia borane is a colorless solid that melts at 110 °C – 114 °C, but is stable at room temperature due to the close BH---HN distances of 2.02 Å between adjacent molecules which remain in the Van der Waals distance range thus allowing strong intermolecular dihydrogen bonds (shown in Figure 1.6).

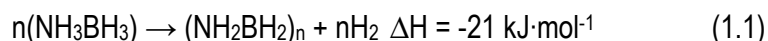
As previously stated, the requirements for a hydrogen storage materials to be used in mobile devices are a fast hydrogen release to power the vehicle when needed in times of acceleration; a controllable hydrogen release to avoid hydrogen peaks when the fuel demand decreases and a hydrogen release to a high extent as high gravimetric densities are needed to comply with the weight restraint for vehicles. Basically, there are two different ways of releasing hydrogen from ammonia borane; hydrolysis and thermolysis.

Ammonia borane will undergo hydrolysis very slowly at room temperature although the rate can be considerably accelerated by lowering the pH or increasing the temperature. Ammonia borane hydrolysis equation is given next.



Besides lowering pH of Aqueous AB dissolutions, hydrolysis rates can be improved by using catalysts [34,35] which can lower the H₂ release temperature to room temperature. If metal catalysts are used, this process can provide ultra-fast hydrogen release (in only few seconds) with very controllable rates and almost completion of AB dehydrogenation, with ~3 equivalents released [34,36]. But despite these outstanding results, ammonia borane hydrolysis is not practical as a method for hydrogen delivery in mobile devices for two main reasons. The use of water to destabilize AB considerably decreases the hydrogen weight percent by a factor of almost two as AB is only moderately soluble in water and consumes 2 waters per AB. Furthermore, the main product of AB hydrolysis are borates which make regeneration of the spent fuel more difficult due to the difficulty of reducing B-O bonds.

The simplest way to release hydrogen from ammonia borane is to just heat it up. The main advantages of thermolysis over hydrolysis is that much higher material weight percent can be achieved. It was previously stated that AB is stable at room temperature but, when heated at elevated rates, it decomposes with vigorous bubbling of hydrogen at 114 °C. However if lower heating rates are used, AB can release hydrogen at temperatures below 100 °C at very low rates. The thermal decomposition of neat NH₃BH₃ is a well-known process [29,37,38]. AB delivers H₂ forming a complex polymeric aminoborane -(NH₂BH₂)_n- (PAB) around 114 °C, below its melting point (ultra-pure material melts at 125 °C [29]:



PAB decomposes with further H₂ release above 150 °C, forming polymeric iminoborane – (NHBH)_n– (PIB) and small fractions of ammonia, diborane and borazine (c-(NHBH)₃), which are undesirable gaseous by-products:



Both reactions possess high activation barriers, which impose sluggish dehydrogenation kinetics at temperatures below 85 °C.

While thermolysis is the simplest system to release hydrogen from AB and the many benefits for engineering an end use system, there are some difficulties associated with solid-state reactions. Regarding on-board hydrogen storage, NH₃BH₃ thermal decomposition still has to overcome various hurdles. Decomposition temperature should be lowered as PEM fuel cells waste heat is ~85 °C and so to avoid the need for heaters, AB should ideally release H₂ near 85 °C. It would

also be necessary to increase hydrogen evolution rate and the extent of AB dehydrogenation at practical temperatures because the third H_2 equivalent is only released from AB above 500 °C. However, at 85 °C, less than one third (one equivalent) of the hydrogen is released from AB. These three problems seriously limit practical use of AB thermal decomposition for hydrogen storage in transportation since fast rates as well as high wt.% H_2 -materials are needed. The fourth major issue is the diversity of products formed during dehydrogenation of AB thus hampering regeneration of the spent fuel. Besides H_2 , AB also evolves some other volatile components such as ammonia (NH_3) or borazine ($N_3B_3H_6$), susceptible to poison catalysts of the fuel cell. It would also be important to prove reversibility of the process as well as suppression of foaming. AB evolves hydrogen with a high amount of energy and various volatile N-B-H compounds above 100 °C [37-39]. All these difficulties have led to extensive study to find ways to improve AB decomposition and many interesting approaches have been described. One of the most promising consisted in confinement of AB in porous materials which combines the effect of nanosizing AB particles and interaction of the host material surface with AB [40,41]. This strategy has demonstrated the reduction of activation barriers for hydrogen release upon confinement, speeding up the dehydrogenation reaction, albeit reaction rates are still low for applications. An additional advantage is that the formation of borazine is greatly reduced [39]. Finally, the exothermicity of the hydrogen desorption reactions is significantly lowered ($\Delta R_H \approx -1 \text{ kJ} \cdot \text{mol}^{-1} H_2$), due to the modification of structural and thermodynamic properties of NH_3BH_3 and the non-volatile polymeric products [39]. Another interesting alternative is the use of ionic liquids to dissolve AB which has been demonstrated to provide better rates and extent of decomposition and H_2 release [42,43]. Dissolution of AB in organic solvents that provide AB dehydrogenation at milder conditions also prove useful to improve dehydrogenation conditions but these compounds are too volatile for practical application and AB decomposition was shown to proceed through a different mechanism that leads to undesired residues [44,45]. Acid or transition metal catalysis which leads to higher decomposition rates have also been reported giving interesting kinetic improvements although the presence of metal species in the residue is undesirable for regeneration [46,47]. The addition of substances that have proven to reduce the induction period for AB dehydrogenation at mild temperature or suppressing foaming also brings interesting enhancement of hydrogen release from AB thermolysis [48] as well as mechanical treatment as could be ball milling or preheating of AB [49,50]. Chemical modification of AB molecule through replacement of one or two of the protonic H from NH_3 moiety by an alkali or alkali-earth metal or introduction of an organic group such as ethyl fragment ($-CH_2CH_3$) have shown to give more stable derivative compounds that release purer hydrogen [51,52].

This Thesis focuses on the study of three different approaches to destabilize ammonia borane and improve its dehydrogenation performance. In a first part of the study, the effect of confining ammonia borane onto the pores of several porous materials such as mesoporous silica and metal oxides was investigated. Previously, the effect of the solvent used during the incipient wetness impregnation to support ammonia borane on the porous materials is evaluated. In the second part of this Thesis, another aminoborane compound, ethane 1,2-diaminebisborane ($\text{CH}_2\text{NH}_2\text{BH}_3$)₂, was synthesized and characterized. Hydrogen release features for this compound were also investigated and compared to those from AB. The bonding properties of all these materials and their reaction products were investigated using the *operando* Raman-MS methodology which constitutes a novel approach for investigating aminoboranes decomposition processes mechanisms. Finally, AB thermal decomposition in various ionic liquids was studied employing, ionic liquids that weren't previously tested in literature. These results were compared with those previously described and AB decomposition mechanism was investigated employing IR spectroscopy.

References

- [1] U.S. Energy Administration Information
<http://www.eia.gov/>
- [2] European Environment Agency
<http://www.eea.europa.eu/>
- [3] Dunn S., *Int. J. Hydrogen Energy* 27 (2002) 235-264
- [4] Schlapbach L., *Nature* 460 (2009) 809-812
- [5] U.S. Department of Energy, hydrogen and fuel cells program/PEM Polymer Electrolyte Membrane (PEM) Fuel Cells
<http://energy.gov/eere/fuelcells/fuel-cells>
- [6] U.S. Department of Energy, Office of Energy Efficiency & Renewable Energy/
<http://energy.gov/eere/>
- [7] European Fuel cells and Hydrogen Joint Undertaking
<http://www.fch.europa.eu/>
- [8] Mandal T.K.; Gregory D.H., *RSC Publishing Annual Reports A* 105 (2009) 21-54
- [9] Schlapbach L.; Züttel A., *Nature* 414 (2001) 353-358
- [10] Chen P., Xiong Z., Luo J., Lin J. Tan K.L., *Nature* 420 (2002) 302-304
- [11] Ströbel R.; Garche J.; Moseley P.T.; Jörisen L.; Wolf G., *J. Power Sources* 159 (2006) 781-801
- [12] Rosi N.L.; Eckert J.; Eddaoudi M.; Vodak D.T.; Kim J.; O'Keeffe M.; Yaghi O.M., *Science* 300 (2003) 1127-1129
- [13] Schüth F.; Bogdanovic B.; Felderhoff M., *Chem. Commun.* (2004), 2249–2258
- [14] Züttel A.; Wenger P.; Rentsch S.; Sudan P.; Mauron Ph.; Emmenegger Ch., *J. of Power Sources* 118 (2003) 1–7
- [15] Yang Z.; Xia Y.; Mokaya R., *J. Am. Chem. Soc.* 129 (2007) 1673-1679
- [16] Wong-Foy A.G.; Matzger A.J.; Yaghi O.N., *J. Am. Chem. Soc.* 128 (2006) 3494-3495

- [17] Suh M.P.; Park H.J.; Prasad T.K.; Lim D.-W., *Chem. Rev.* **112** (2012) 782-835
- [18] Chen J.; Wu F., *Appl. Phys. A* **78** (2004) 989-994
- [19] Budd P.M.; McKeown N.B.; Fritsch D., *J. Mater. Chem.* **15** (2005) 1997-1986
- [20] Germain J.; Hradil J.; Fréchet J.M.J.; Svec F., *Chem. Mater.* **18** (2006) 4430-4435
- [21] Ghanem B.S.; Msayib K.J.; McKeown N.B.; Harris K.D.M.; Pan Z.; Budd P.M.; Butler A.; Selbie J.; Book D.; Walton A., *Chem. Commun.* **1** (2007) 67-69
- [22] Dyadin Y.A.; Larionov E.G.; Manakov A.Y.; Zhurko f.V.; Aladko E.Y.; Mikina T.V.; Komarov V.Y., *Mendeleev Commun.* **9** (1999) 209-210
- [23] Struzhkin V.V.; Militzer B.; Mao W.L.; Mao H.K.; Hemley R.J., *Chem. Rev.*, **107** (2007) 4133-4151
- [24] Weitkamp J.; Fritz M.; Ernst S., *Int. J. Hydrogen Energy* **20** (1995) 967-970
- [25] Eberle U.; Felderhoff M.; Schüth F., *Angew. Chem. Int. Ed.* **48** (2009) 2-25
- [26] Orimo S.I.; Nakamori Y.; Eliseo J.R.; Züttel A.; Jensen C.M., *Chem. Rev.* **107** (2007) 4111-4132
- [27] Parry R.W.; Schultz D.R.; Girardot P.R., *J. Am. Chem. Soc.* **80** (1958) 1-3
- [28] Marder T.B., *Angew. Chem. Int. Ed.* **46** (2007) 8116-8118
- [29] Stephens F.H.; Pons V.; Baker R.T., *Dalton Trans.* **25** (2007), 2613-2626
- [30] M. Bowden, T. Autrey, I. Brown, M. Ryan, *Current Applied Physics* **8** (2008), 498-500
- [31] Shore S. G.; Parry R. W., *J. Am. Chem. Soc.* **77** (1955) 6084-6085
- [32] Shore S. G.; Parry R. W., *J. Am. Chem. Soc.* **80** (1958) 20-24
- [33] Paolone, A.; Palumbo, O.; Rispoli, P.; Cantelli, R.; Autrey, T.; Karkamkar, A. *J. Phys. Chem. C* **113** (2009) 10319-10321
- [34] Chandra M.; Xu Q., *J Power Sources* **156** (2006) 190-194
- [35] Xu Q.; Chandra M., *J Power Sources* **163** (2006) 364-370
- [36] Chandra M.; Xu Q., *J Power Sources* **168** (2007) 135-142
- [37] Wolf G.; Baumann J.; Baitalow F.; Hoffmann F.P., *Thermochim. Acta* **343** (2000), 19-25
- [38] Baitalow F.; Baumann J.; Wolf G.; Jaenicke-Röbler K.; Leitner G., *Thermochim. Acta* **391** (2002), 159-168
- [39] Baumann J.; Baitalow F.; Wolf G., *Thermochim. Acta* **430** (2005) 9-14
- [40] Gutowska A.; Li L.; Shin Y.; Wang Ch.M.; Li X.S.; Linehan J.C.; Smith R.S.; Kay B.D. Schmid B.; Shaw W.; Gutowski M.; Autrey T., *Angew. Chem. Int. Ed.* **44** (2005) 3578-3582
- [41] Nielsen T.K.; Manickam K.; Hirscher M.; Besenbacher F.; Jensen T.R., *Nanoscale* **3** (2011) 2086-2098
- [42] Bluhm M.E.; Bradley M.G.; Butterick R.; Kusari U.; Sneddon L.G., *J. Am. Chem. Soc.* **128** (2006) 7748-7749
- [43] Himmelberger D.W.; Alden L.R.; Bluhm M.E.; Sneddon L.G., *Inorg. Chem.* **48** (2009) 9883-9889
- [44] Jaska C. A.; Temple K.; Lough A. J.; Manners I.; *J. Am. Chem. Soc.* **125** (2003) 9424-9434
- [45] Shaw W.S.; Linehan J.C.; Szymczak N.K.; Heldebrant D.J.; Yonker C.; Camaioni D.M.; Baker R.T.; Autrey T., *Angew. Chem. Int. Ed.* **47** (2008) 7493-7496
- [46] Chen Y.; Fulton J.L.; Linehan J.C.; Autrey T., *J. Am. Chem. Soc.* **127** (2005) 3254-3255

- [47] Stephens F.H.; Baker R.T.; Matus M.H.; Grant M.H.; Dixon D.A., *Angew. Chem. Int. Ed.* **46** (2007) 746-749
- [48] Heldebrant D.J.; Karkamkar A.; Hess N.J.; Bowden M.; Rassat S.; Zheng F.; Rappe K.; Autrey T., *Chem. Mater.* **20** (2008) 5332-5336
- [49] Zhang J.; Zhao Y.; Akins D.L.; Lee J.W., *J. Phys. Chem. C* **114** (2010) 19529-19534
- [50] Neiner D.; Karkamkar A.; Linehan J.C.; Arey B.; Autrey T.; Kauzlarich S.M.; *J. Phys. Chem. C* **113** (2009) 1098-1103
- [51] Spielmann J.; Jansen G.; Bandmann H.; Harder S., *Angew. Chem. Int. Ed.* **47** (2008) 6290 –6295
- [52] Neiner D.; Karkamkar A.; Bowden M.; Choi Y.J.; Luedtke A.; Holladay J.; Fisher A.; Szymczak N.; Autrey T., *Energy Environ. Sci.* **4** (2011) 4187-4193

2. EXPERIMENTAL SECTION

2.1 Materials

Neat ammonia borane (NH_3BH_3) was supplied by Sigma Aldrich (97 % purity) and used without further purification for the measurements described in the next chapters. For AB recrystallization and mesoporous materials impregnation, methanol (99.99 %, Scharlab) and tetrahydrofuran (THF) (≥ 99.9 %, Sigma Aldrich) were used as solvents.

EDAB samples were synthesized by reaction of ethylene diamine dihydrochloride (≥ 99.0 %, Sigma Aldrich) and sodium borohydride (99.0 %, Sigma Aldrich) in anhydrous THF (≥ 99.9 %, Sigma Aldrich).

For the synthesis of mesoporous Ga_2O_3 : gallium (III) nitrate hydrate (99.99 %, Strem Chemicals) was used as the inorganic precursor, Pluronic F127 ($\text{PEO}_{106}\text{PPO}_{70}\text{PEO}_{106}$) (99.9999 %, BASF) as structure directing agent and ethanol (~ 99 %, Sigma) as the solvent.

For CoAPO-5 synthesis: H_3PO_4 (85 % in aqueous solution, Sigma Aldrich), $\text{Al}(\text{OH})_3 \cdot x\text{H}_2\text{O}$ (Sigma Aldrich), $\text{Co}(\text{CH}_3\text{COO})_2 \cdot 4\text{H}_2\text{O}$ (98 %, Panreac) and N-methyldicyclohexylamine (97 %, Sigma Aldrich) (MCHA) were used.

For silica synthesis: surfactant Pluronic P123 from Sigma Aldrich, triblock poly(ethylene oxide)-poly(propylene oxide)-poly(ethylene oxide) ($\text{PEO}_{20}\text{PPO}_{70}\text{PEO}_{20}$) and Pluronic PE 10400 ($\text{PEO}_{25}\text{PPO}_{56}\text{PEO}_{25}$) from BASF, were used as structure directing agents. Tetraethoxysilane (≥ 99 %, TEOS) (Merck) and tetramethoxysilane (99 %, TMOS) (Aldrich) were used as silica sources while hydrochloric acid was purchased from Panreac.

For ionic liquids dissolutions of AB, the following ionic liquids were purchased from Iolitec Ionic Liquids Technologies GmbH (Germany): 1-butyl-3-methylimidazolium chloride (bmimCl, purity: 99 %), 1-allyl-3-methylimidazolium chloride (amimCl, purity: 98 %), 1-(2-hydroxyethyl)-3-methylimidazolium chloride (HOemimCl, purity: 99 %), 1-ethyl-3-methylimidazolium chloride (emimCl, purity: 98 %), 1-ethyl-3-methylimidazolium acetate (emimAc, purity: 95 %), tetrabutylphosphonium chloride (TbPhCl, purity: 95 %), choline dihydrogen phosphate (ChdHPh, purity: 95 %), choline acetate (ChAc, purity: 98 %), choline bis(trifluoromethylsulfonyl)imide (ChTf₂N, purity: 99 %), 1-ethyl-3-methylimidazolium triflate (emimTfO, purity: 99 %), 1-ethyl-3-methylimidazolium bis (trifluoromethylsulfonyl) imide (emimTf₂N, purity: 99 %), 1-ethyl-3-methylimidazolium ethyl sulphate (emimESO₄, purity: 99 %) and 1-ethyl-3-methylpyridium bis(trifluoromethylsulfonyl)imide (empyTf₂N, purity: 99 %).

2.2 Characterization techniques

2.2.1. Scanning electron microscopy (SEM) is a technique that allows the observation and characterization of inorganic and organic materials through the study of surfaces by imaging of a conductive sample (up to 0.8 nm resolution), hence characterizing the size, the morphology, the different phases as well as the elemental composition of nanoparticles (EDS). From the interaction of the electron beam with the sample, there are different types of signal that are used to examine many of its features.

The energy dispersive X-ray radiation used in the analyzer, is characteristic X-rays emitted from the sample as a result of electron bombardment. The analysis of this radiation provides analytical information on the composition of the total or partial areas of the sample. Normal specimens must be in a solid and dried state and, if the sample is not a good enough electrical conductor, a metallic coating is applied prior to SEM analysis.

In this study, the outer surface of neat and recrystallized AB was imaged using a Hitachi TM-1000 SEM instrument, operated at 20 kV in high-vacuum mode.

2.2.2 Transmission Electron Microscopy (TEM) permits characterizing the inner structure of very thin samples (up to 200 nm in thickness) and thus identifying crystalline, phases (up to 0.1 nm) by using a thin beam of accelerated electrons as a light source which gives the high resolution of the Electron Microscopy. TEM has thus become an indispensable tool in Materials Science. Electrons have both wave and particle properties, and their wave-like properties mean that a beam of electrons can in some circumstances be made to behave like a beam of radiation. The wavelength is dependent on their energy, and so, can be tuned by adjustment of accelerating fields, and can be much smaller than that of light, yet they can still interact with the sample due to their electrical charge. Therefore, when a beam of electrons accelerated at high speed by application of a high potential difference, passes through the sample, the electrons will be dispersed in different trajectories as a function of the ultrastructure characteristics of the material observed. By placing a physical barrier with small opening angle below the sample, electrons scattered by certain angles will be removed. The image formed will be more intense in those areas corresponding to a greater mass. The image is enlarged and projected onto a screen fluorescent display in real time and can digitally be acquired by a charge coupled detectors (CCD). The powdered material samples for study in the transmission electron microscope requires the dilution of a very small amount of sample in an organic harmless solvent, usually dichloroethane, acetone or water. It is necessary to achieve maximum dispersion by immersing the solution in an ultrasonic bath and finally, place a drop of it on a carbon grid to be directly observed in the microscope.

TEM micrographs of the porous materials used as supports in this study were taken on a 2100 JEOL electron microscope operating at 100 kV. Prior to measurements, an aliquot was prepared with a small amount of each sample that was suspended in ethanol by sonication in an ultrasonication water bath for 2 min. A drop of this suspension was then dispersed onto a holey carbon film on a copper grid, followed by drying at room temperature.

2.2.3 Powder X-ray Diffraction (XRD) is perhaps the most widely used x-ray diffraction technique for characterizing materials. As the name suggests, the sample is usually in a powdery form, consisting of fine grains of single crystalline material to be studied. Specifically, it is a non-destructive analytical characterization technique employed to identify crystalline phases and characterize crystalline structures present in a material at an atomic level. It also determines structural properties such as defect structures, crystal size or preferred orientation among others. X-rays have wavelength of ~ 0.1 nm and therefore are scattered by molecules. For molecules in ordered arrays such as crystals, X-ray scattering produces diffraction patterns. The patterns are unique to the crystal structure and act as a fingerprint of the material. In the case of materials having the same crystal structure and similar atoms sizes, the XRD patterns are very similar. The peaks in an x-ray diffraction pattern are directly related to the atomic distances and an XRD pattern can provide other important information such as lattice parameters using Bragg's Law and grain size using Scherrer's equation. By comparing the experimental diffractograms with diffraction patterns recorded in the different databases (JCPDS, CSD, ICSD, CDD, etc...) the identification of crystalline phases in the sample is possible.

XRD patterns of all the materials under study were collected using a Philips X'PERT apparatus by means of the $\text{Cu-K}\alpha$ (wavelength 1.5406 Å) radiation source. The data were collected with 2θ range of 6.00° - 90.00° , applying 2θ steps of 0.04° and accumulation times of 5 s. Diffraction patterns were plotted using Panalytical x'pert pro software and, in the case of EDAB materials, refined by the Rietveld method using Full Prof software [1]. For some of the porous supports, the 2θ range of 0.4° - 6.0° (low angle) was also covered as such data can reveal crucial information on the pores size distribution.

2.2.4 Inductively coupled plasma (ICP) has firmly consolidated as one of the techniques with the most potential to analyze trace elements and its isotopes in all kind of matrix. If fitted with an online mass spectrometer (ICP-MS), this technique allows analyzing all elements with some exceptions (H, He, C, N, O, F, Ne, Ar, Kr, Xe and Cl). The most common sample introduction system consists of a nebulizer and spray chamber. The nebulizer converts the liquid samples into

very small droplets. These droplets are carried through the spray chamber and into the torch and then into the Ar plasma at a temperature of 10000 °C. The sample is dried, vaporized, atomized and ionized. These ions pass through the interface to the mass spectrometer. The ions are focused by the ion lens and are separated by their mass-to-charge ratio in a quadrupole and finally are measured by the detector.

Mass Spectrometry is a useful technique to elucidate molecules structure through the measurement of molecular mass and the mass of characteristic fragments from the molecular structure. The technique is based upon the ionization of sample components; this process takes place in the ionization chamber. The gas phase ions produced in the ionization chamber, are accelerated towards the mass analyzer and separated according to their mass/charge ratio. This separation is achieved by means of the application of complex electric, magnetic fields or recording the different times of flight of the ions. Finally the ions strike the detector and these signals are amplified and converted into a mass spectrum which represents the ion intensities versus its mass/charge ratio.

ICP-MS can provide isotopic information giving what is sometimes referred to as the isotopic fingerprint of the element. Current equipments combine high sensitivity and low background signals to give very low detection limits (sub- $\mu\text{g/l}$ in most cases) offering a wide analytical working range up to 8 orders in a single acquisition and allowing semiquantitative and quantitative multielemental analysis.

Elemental analyses of neat and recrystallized AB samples were performed using a LECO elemental analyzer CHNS-932. They were burned in an excess of oxygen, and the mass of these combustion products (NO_2 , CO_2 and H_2O) were used to calculate the percentage of C, H and N contained in each sample. Each sample was analyzed three times and the average value is reported.

2.2.5 N_2 adsorption/desorption isotherms are a method for measuring the specific surface area and pore size distribution of adsorbents and porous materials in general as it is essential for understanding confinement effect on adsorbate molecules arrangement in their aggregates and the reactions that may take place on a phase boundary between the solid and gas phase. In this work, surface areas were measured by the Brunauer-Emmett-Teller (BET) method using N_2 as the adsorbent [2,3]. The method takes advantage of well-described equilibrium between the gas phase (i.e. partial pressure) and adsorbed N_2 on the surface of a material at the boiling temperature of N_2 . By measuring the amount of adsorbed N_2 and the equilibrium pressure of N_2

above the sample at several points, an isotherm can be fitted to the data, and surface area extracted from it, given that the size of the N₂ molecule is known.

In our study, N₂ isotherms were measured at -196 °C in a Micromeritics ASAP 2420 device to determine textural properties of the porous supports and of some of the AB impregnated samples. The specific surface area, S_{BET} , was estimated from N₂ adsorption data in the relative pressure range from 0.04 to 0.2 using the BET method as stated earlier. The total pore volume, V_p , was determined from the amount of N₂ adsorbed at a relative pressure of 0.98 [4]. Pore size distributions were obtained from the adsorption branches of the isotherms using the Barrett-Joyner-Halenda (BJH) model with cylindrical geometry of the pores [4]. The BJH pore diameter, D_p BJH, is defined as a position of the maximum on the pore size distribution. Prior to taking measurements, the porous supports were pretreated by evacuating them at 350 °C and the impregnated samples at room temperature for at least 16 hours to desorb impurities from the surface of the sample.

2.2.6 The Differential Scanning Calorimetry (DSC) measured the difference in temperature between a sample and an internal reference depending on the time and/or temperature applied. The observed temperature difference translates into heat flow. This allows measuring endothermic and exothermic transitions and is very useful in the measurement of thermal stability of materials, the moisture content and/or other volatile materials or the measurement of melting/crystallization temperatures for example. DSC measurements can be performed under temperature ramp, with different speeds or under isothermal conditions.

Calorimetric measurements were performed in a DSC from TA Instruments (mod. Q100). The experiments were carried out under N₂ flow (50 mL·min⁻¹) by using Al pans with pressed Al covers. For the isothermal experiments the samples were firstly stabilized at 20 °C and then heated by using a constant heating rate of 2 °C/min to reach the desired temperature. Then, the time evolution of the heat flow signal following AB decomposition was recorded under constant temperature. Non isothermal measurements were also performed in the same apparatus at various heating rates in the range 20-250 °C.

2.2.7 The Thermogravimetric analysis (TGA) measure the quantity and the speed of the change in weight of a sample depending on the temperature and/or time in a controlled atmosphere. It is useful for determination of the composition of materials and to predict their stability at temperatures of up to 1000 °C. This technique can, therefore, characterize materials with loss or gain of weight due to decomposition, oxidation or dehydration. It is possible to run the TGA

measurements under temperature ramps with different speeds or under isothermal conditions and, if the equipment provides high resolution, overlapping processes can be separated.

During Differential Thermal Analysis (DTA), the material under study and an inert reference are made to undergo identical thermal cycles. In this technique, the heat flow to the sample and reference is the parameter that is kept constant and any temperature difference between sample and reference is recorded. The differential temperature is then plotted against time, or against temperature to obtain the DTA curve or thermogram.

While TGA only measures changes caused by mass loss, DTA also registers changes in material where no mass loss occur, and so by combining the two techniques (TGA-DTA), a comprehensive study of a material thermal behavior can be performed. In addition, the evolved gas from the TGA-DTA system can be analyzed in a mass spectrometer attach to the oven output to complete the compositional study of the material.

In the framework of our study, combined DTA-TGA-MS measurements were performed with a Setaram Setsys Evolution 1200 apparatus coupled to a quadrupole MS (Pfeiffer). These measurements were obtained under flowing Ar gas (99.999 % purity) or under dynamic vacuum ($\sim 2 \cdot 10^{-4}$ mbar). The baselines of the DTA-TGA-MS system were obtained at the same experimental conditions. It must be noted that the MS hydrogen desorption curves are slightly shifted to higher temperatures and present a wider shape than the DTA ones. This is an experimental artifact due to the delay time between H₂ desorption at the DTA apparatus and its detection at the MS. Therefore, we will consider the DTA peak temperatures as more reliable than the MS ones in subsequent analyses.

2.2.8 Thermal Desorption Spectroscopy/Mass Spectrometry (TDS/MS) is a technique that combines thermal and compositional analyses. As the shape of the MS signal closely follows that of the DSC signal during H desorption, the decomposition heat of hydrides can be related as follows to the number of moles of hydrogen evolved (dn/dt) from the sample at temperature T per unit time through the decomposition heat of the metal hydride (ΔH), the heating rate (β), the DSC signal (W) at temperature T and the integral extending from temperature T₀, at which the reaction has not started, to temperature T_m.

$$\Delta Q = \int_{T_0}^{T_m} \frac{dn}{dt} \Delta H \frac{dT}{\beta} = \int_{T_0}^{T_m} W \frac{dT}{\beta}$$

The number of moles of hydrogen evolved from the sample at any temperature can be obtained from the MS signal and the calibration curve through:

$$\Delta n = \int_{T_0}^{T_m} \frac{dn}{dt} \frac{dT}{\beta} = g \int_{T_0}^{T_m} I_{H_2} \frac{dT}{\beta}$$

where I_{H_2} is the H_2 -ion current detected by the MS device and g is the calibration factor.

Experiments were performed by means of a differential scanning calorimeter (Perkin Elmer DSC-4) connected through a thin capillary tube to a vacuum chamber equipped with a quadrupole mass spectrometer (QMS 200 Balzers), a penning gauge and a turbomolecular pump for gas analysis. The sample (10 mg) is held in an aluminum pan located in a double-furnace system for DSC measurements while an empty aluminum pan is used as a reference. A controlled flux of carrier gas (Ar) is passed through the DSC system while a linear heating ramp is imposed on both aluminum pans. The DSC furnace provides the linear heating ramp needed in a TDS system and good isolation which, combined with the low sample mass allows very good linear heating ramps. During normal operation, the carrier gas, Ar, and the gas evolved from the sample, H_2 are extracted from the DSC system by a vacuum gradient imposed in the capillary tube. Most of the Ar- H_2 mixture (99 %) is evacuated by a rotary pump, while 1 % is conducted through a dosing valve to the high vacuum chamber. The instantaneous H_2 -ion current measured by the MS is proportional to the hydrogen desorption rate from the sample and so this equipment conforms to a TDS system allowing the acquisition of simultaneous thermodynamic and kinetic properties of the sample [5,6]. Data acquisition from the DSC and MS systems was accomplished with Balzers Quadstar 422 acquisition software.

2.2.9 Isothermal H_2 release measurements were carried out on the AB/ionic liquids samples. Figure 2.1 shows a scheme and a photograph of the glass pressure reactor used in such experiments. Prior to every analysis, ionic liquids were dried at 90 °C in a vacuum oven (model VACIOTEM-T9 from J. P. Selecta) for at least 24 h. Working inside a glove box inertized with N_2 , a solution of ammonia borane in the ionic liquid of known composition was then prepared by weighing, and a weighed amount of this solution was loaded inside the glass pressure reactor (model Q-Tube, manufactured by Q Labtech). The glass reactor was sealed and subjected to vacuum down to an absolute pressure of 10 mbar using a vacuum pump (model FB6545 manufactured by ILMVAC GmbH). The reactor was then introduced in an oven (model DIGITRONIC from J.P. Selecta) thermostated at 85 °C (with an uncertainty of ± 1 °C). All

experiments were conducted at the fixed temperature of 85 °C because this is a typical operational temperature of polymer electrolyte membrane (PEM) fuel cells. Therefore at this temperature, it could be possible to use excess heat from the fuel cell to decompose the hydride [7]. The evolution of pressure inside the reactor during heating due to the release of hydrogen was measured during a period of at least 8 h with a certified pressure gauge (model DRUCK DPI 104, manufactured by General Electric Measurement & Control) (with an uncertainty of ± 1 mbar), connected to a computer using the SiCal Pro data acquisition software for acquisition. The evolution of the sample along the experiment was also video recorded with a digital camcorder. At the end of the measurement, the glass reactor was cooled down to ambient temperature, H₂ inside the reactor was purged, and in selected experiments a sample of the solution was retrieved from the reactor working inside the glove box. After the experiment, the amount of H₂ released was calculated from pressure recordings and fixed conditions of temperature and glass reactor volume (calculated from the difference of weight between the empty reactor and the reactor filled with water), employing the Hydrogen Reference Equation of State [8] implemented in the Reference Fluid Thermodynamic and Transport Properties Database (REFPROP) software developed by the National Institute of Standards and Technology (NIST) [9]. Some experiments where visualization of the sample evolution was not necessary were carried out in an equivalent reactor made of stainless steel instead of glass to improve isolation of the system.

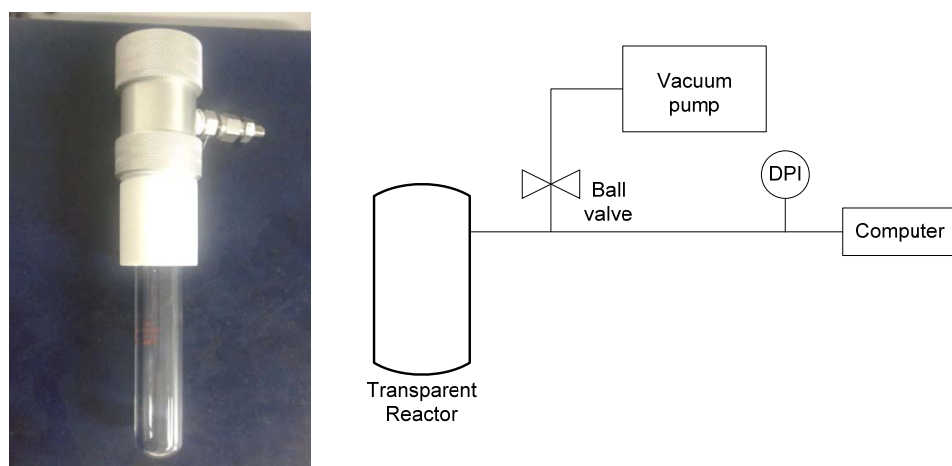


Figure 2.1: Photograph and schematic diagram of the hydrogen release cell

2.2.10 The Nuclear magnetic resonance (NMR) studies the behavior of atomic nuclei with spin different from zero under the influence of an external magnetic field. Each nuclei is affected by this field, as well as the fields created in their environment by the nearby nuclei and electronic distribution. These nuclear interactions will depend on the relative orientation of the molecules

thus providing information about the chemical surrounding of the resonating nuclei, such as chemical bonds, coordination numbers and bond angles. Therefore, NMR proves to be a useful technique with a high sensitivity for chemical bonds in the local structure of resonating nuclei.

In our study, NMR spectroscopic experiments were performed on the EDAB samples to identify chemical bonds in the molecule. Such analyses were run in D₂O solution, at 20 °C, on a Bruker Avance spectrometer (500 MHz for ¹H). Chemical shifts (δ) in D₂O were referenced to CDCl₃ in the case of ¹H and ¹³C signals and to BF₃OEt₂ for ¹¹B experiments. NMR Data: ¹H NMR (500 MHz) δ: 2.95 (4H, s), 1.67-1.13 (6H, q JH-B 86 Hz) ppm; ¹³C NMR (125 MHz) δ: 45.66 ppm; ¹¹B NMR (167 MHz) δ: - 20.90 ppm (1B, q JB-H = 95 Hz).

2.2.11 Raman Spectroscopy is a useful technique for studying the vibrational motions of molecules in molecular systems. It is based on the Raman effect; when photons impact onto a molecule, most of them interact elastically with the electron cloud, i.e. the molecule becomes excited and then goes back to the original state or light is scattered at the same wavelength as incident light via Rayleigh Scattering or elastic radiation. However, in some excitation events, a change in the polarizability of the molecule during vibration is involved giving rise to an inelastic scattering of electromagnetic radiation. This is the Raman scattering, during which the Raman photons are shifted in frequency (energy) from the frequency of the incident radiation with a shift that corresponds to the vibrational energy that is gained or lost in the molecule, the Raman shift. Thus, Raman scattering affords information about the structure and properties of molecules from their vibrational transitions. A Raman spectrum shows the intensity of the dispersion versus the Raman shift.

Raman spectrometers are constituted by an excitation source (laser), sample illumination, and collection of scattered radiation. The collected radiation is taken to the spectrometer, giving rise to Raman signal. Raman lasers typically work in the UV, visible, NIR, and IR and it is necessary to remove the elastic dispersion radiation (Rayleigh) from the inelastic one (Stokes) since the former is more than 6 orders of magnitude stronger than the latter. This is done by means of Rayleigh filters which allow using a single monochromator (see Figure 2.2). After removing the elastic dispersion, which determine the resolution and the signal-to-noise ratio, the detectors are ready to register the Raman signal.

Because of the weak Raman signal, the main problem is the detection of a significant amount of Raman photons. This is solved by the use of charge coupled detectors (CCD) that consist of bidimensional arrangements of ~6–30 μm pixels. They possess high quantum efficiency and sensitivity in a wide spectral window (120–1000 nm) but their very high sensitivity detectors

makes them sensitive to interference. Most Raman system have then a software option to discriminate interferences, typically based on comparing several spectra.

In the case of this study, Raman measurements were carried out using a $\lambda=785$ nm excitation line of 350 mW, set to deliver 100 mW to the sample. Spectra were collected in a frequency range of 95-3500 cm^{-1} Raman shift, using a RamanStation 400F model of PerkinElmer spectrometer equipped with a cooled open electrode CCD, 1.024x256 pixels sensor, hermetically sealed vacuum and air-cooled, operated at -50 $^{\circ}\text{C}$. The spectral resolution was 2 cm^{-1} FWHM and spectra acquisition consisted of different numbers of accumulations of 10 seconds spectra depending on the sample. The acquisition software used was Spectrum and spectra were analyzed using Omnic and Origin Labs software.

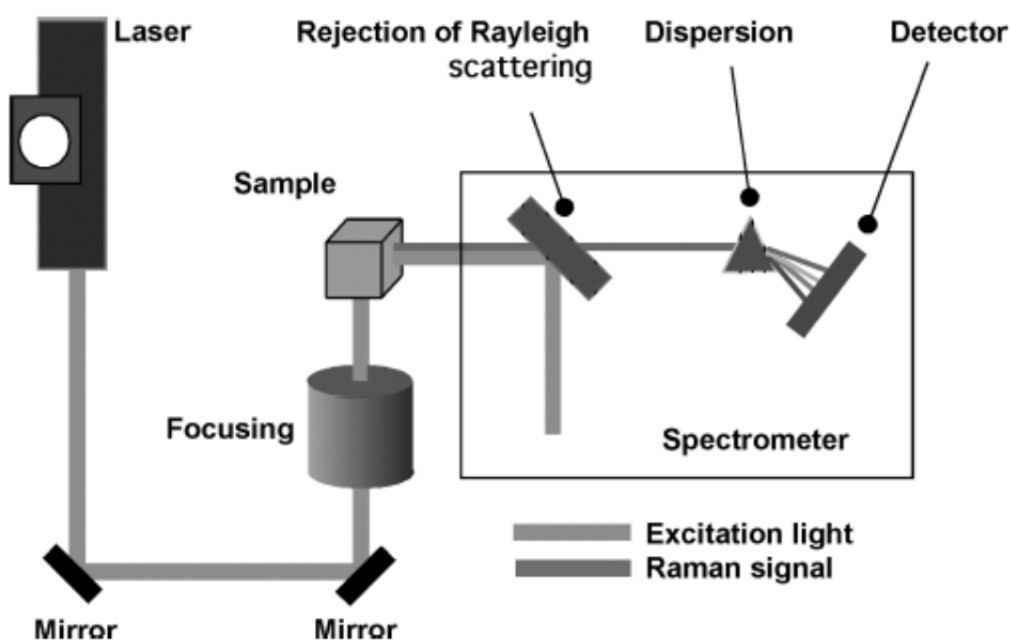


Figure 2.2: Schematic diagram of the Raman Spectrometer (extracted from *In-situ Spectroscopy of Catalysts*, American Scientific Publishers, 2004)

2.2.12 Operando Raman- Mass Spectrometry. Thermal decomposition of some of the studied materials was real-time monitored by *Operando* methodology which combines in situ Raman spectroscopy during real working conditions with online analysis of effluents by mass spectrometry (MS) in the case of this study [10]. Such *Operando* Raman- Mass Spectrometry analyses were run fitting downstream the Raman spectrometer previously described a HIDEN HPR20 mass spectrometer equipped with a quadrupole (QMS), a Faraday type detector and a turbomolecular pump, installed in series with a vacuum pump. The system was evacuated and flooded with high purity nitrogen, introduced into the lines by mass flow controllers, and a residual

pressure of $2.5 \cdot 10^{-5}$ mbar was maintained in the MS chamber. This pressure was controlled with an automatic valve connected to the pressure reading. During thermal decomposition of AB materials, H_2 and other volatile components release was followed by using time-resolved gas phase analysis by means of the QMS while structural changes of the material were simultaneously monitored by Raman spectroscopy. This methodology allows a detailed study of structure-property relationships for the decomposition process.

In these experiments, 0.075 g of the studied sample were introduced in a tailor-made quartz catalytic reactor that is also a spectroscopic Raman cell, tailor-made for us by Hellma TM, to allow acquisition of high-quality spectra with simultaneous mass spectrometric analysis of outlet gas stream. The material was previously sieved to 250-420 μm particle size range and, to prevent void volume, SiC (99 % from Technical with $d_p=0.5$ mm) was placed upstream and downstream the sample fix-bed as an inert packing, thus delivering homogeneous temperature in the reactor, as described elsewhere [11]. This system is heated with an ad-hoc oven also designed by Catalytic Spectroscopy Laboratory group and tailor-made for us by Ramen S.L. (Figure 2.3). Two K-type thermocouples introduced into the sample bed are used to monitor/control the reactor temperature using a Toho TC-22 controller and to deliver an auxiliary temperature reading in the online mass spectrometer. The ad-hoc oven containing the spectroscopic cell is placed in the Raman spectrometer (see Figure 2.3).

Two different kinds of *Operando* Raman-MS measurements were performed to follow the evolution of hydrogen and other volatile components during the thermal decomposition of neat, recrystallized and supported samples. On one hand, isothermal measurements were carried out at 80 °C, 85 °C and 90 °C to evaluate the possibility of using such materials at 85 °C, the working temperature of fuel cells. On the other hand, 1 °C \cdot min $^{-1}$ ramp *Operando* analysis were run on supported AB materials to evaluate confinement effect on AB thermal decomposition. All measurements were performed under 200 mL/min of carrier gas namely, 99.9995 % N_2 . Again, spectra acquisition consisted of different numbers of accumulations of 10 seconds spectra depending on the sample with a spectral range of 95-3500 cm^{-1} Raman shift. The peak resolution was 2 cm^{-1} FWHM.

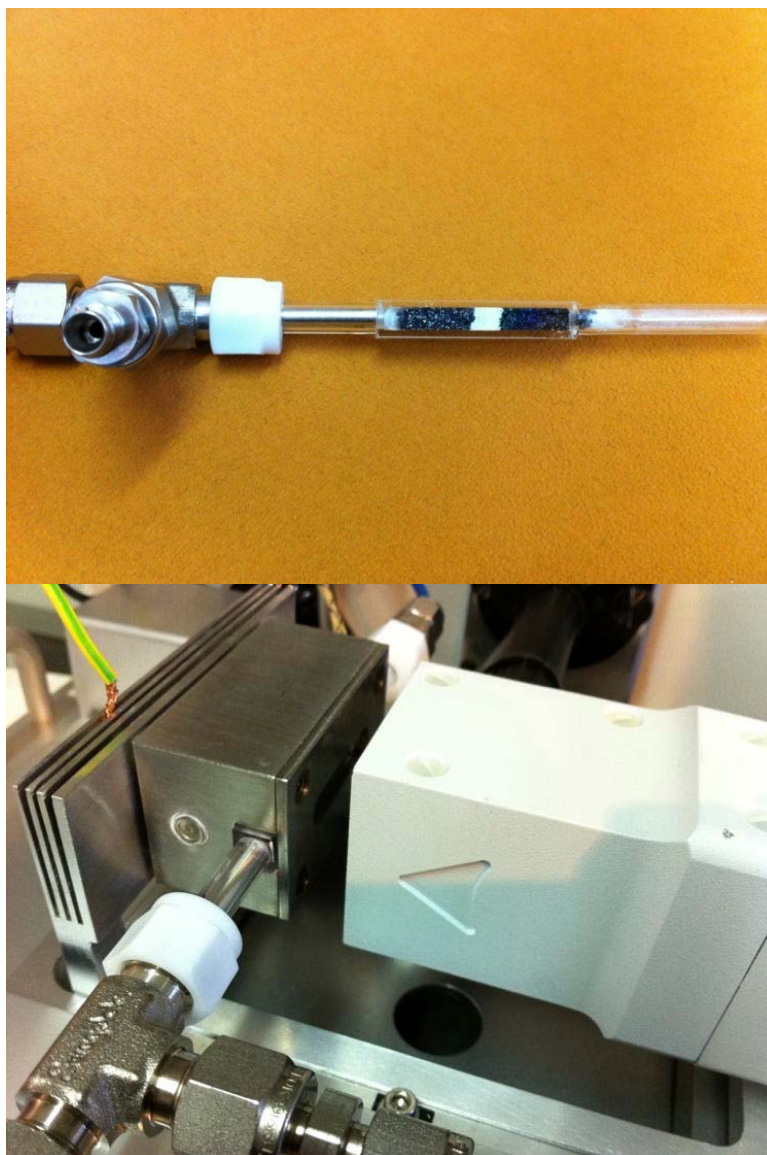


Figure 2.3: Reactor cell (top) and equipment used during Raman-MS *Operando* analyses (bottom)

2.2.13 Infrared spectroscopy (IR) is a very powerful tool for the characterization of the main functional groups and the structure of materials, as well as the study of solid surfaces. It is another vibrational technique which fundamentals share many similarities with those defining Raman spectroscopy. As already stated, molecular spectroscopy comprises the study of the interaction between the electromagnetic radiation and matter. In the case of IR, a given molecule absorbing infrared radiation changes its vibrational and rotational states of energy. Unlike Raman spectroscopy, the IR absorption is linked to a direct resonance between the frequency of the IR radiation and the vibrational frequency of a specific vibration mode. Thus, transitions that involve changes in the dipole moment of the molecule during vibration are active in IR. IR spectroscopy can be performed by two separate technical modes, transmission of the light through the sample or collection of the light diffused by the surface of the powder.

In our study, IR measurements for AB/ionic liquids materials were carried out by means of a spectrometer Bruker ALPHA with a sampling module Platinum ATR from Bruker.

-
- [1] Rodríguez Carvajal J., *Phys. B: Condensed Matter* **192** (1993) 55–69
- [2] Sing K.S.W.; Everett D.H.; Haul R.A.W.; Moscou L.; Pierotti R.A.; Rouquerol J.; Siemieniowska *Pure & Appl. Chem.* **57** (1985) 603–619
- [3] Brunauer S.; Emmett P.H.; Teller E., *J. Am. Chem. Soc.* **60** (1938) 309–319
- [4] Barrett E.P.; Joyner L.G.; Halenda P.P., *J. Am. Chem. Soc.* **73** (1951) 373–380
- [5] Fernández J.F.; Cuevas F.; Sánchez C., *J. Alloys Comp.* **298** (2000) 244–253
- [6] Leardini F.; Fernández J.F.; Bodega J.; Sánchez C., *J. Phys. Chem. Solids* **69** (2008) 116–127
- [7] Smitha B.; Sridhar S.; Khan A.A. *J Membr Sci.* **259** (2005) 10–26
- [8] Leachman J.W.; Jacobsen R.T.; Penoncello S.G.; Lemmon E.W., *J. Phys. Chem. Ref. Data* **38** (2009) 721–748
- [9] Lemmon E.W.; Huber M.L.; McLinden M.O.; NIST standard reference database 23-REFPROP, version 9.1. *Standard Reference Data Program* (2013)
- [10] Bañares M.A.; *Catal. Today* **100** (2005) 71–77
- [11] Guerrero-Pérez M.O.; Bañares M.A., *Catal. Today* **96** (2004) 265–272

Chapter 3

Ammonia Borane recrystallization and confinement: solvent effect

Summary

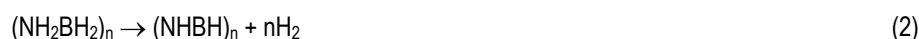
Hydrogen thermal desorption from ammonia borane (NH_3BH_3 , hereafter AB) has been investigated by means of Thermal Desorption Spectroscopy coupled with a mass spectrometer (TDS-MS), Differential Scanning Calorimetry (DSC) and Operando Raman-MS methodology. The effect on the dehydrogenation conditions of recrystallizing AB in methanol and tetrahydrofuran as the first step in scaffolding AB into porous materials by incipient wetness impregnation has been evaluated as well as the effect of AB impregnation onto mesoporous gallium oxide. AB releases hydrogen by a series of moderately exothermic reaction pathways hindered by slow kinetics and volatile impurities released simultaneously to hydrogen. Recrystallization of AB from different solvents produces small morphological variations, but without changes in structural properties at room temperature. Impregnation of AB onto porous materials has been shown to improve AB kinetic performance, but limited by the amount of AB that can be impregnated without formation of segregated AB crystals outside the pores of gallium oxide and with evolution of some NH_3 simultaneously to H_2 release.

3.1. Introduction

As previously mentioned in chapter 1, ammonia borane (AB, NH_3BH_3) is a promising chemical hydride which releases hydrogen by thermal decomposition. The thermal decomposition of neat NH_3BH_3 is a well-known process that has been recently investigated by several groups [1-5]. At temperatures below melting ($T < 114^\circ\text{C}$), ammonia borane (AB) yields H_2 and a complex polymeric aminoborane $-(\text{NH}_2\text{BH}_2)_n-$ (PAB):



In turn, PAB decomposes above 150°C with further H_2 loss, forming polymeric iminoborane $-(\text{NHBH})_n-$ (PIB) and small fractions of ammonia (NH_3), diborane (B_2H_6) and borazine ($\text{c}-(\text{NHBH})_3$), which are undesirable gaseous by-products:



However, both reactions are stabilized by high activation barriers, which impose sluggish dehydrogenation kinetics at temperatures below 100°C . Therefore, in a first approach to enable AB as a compound for on-board hydrogen storage, the sluggish dehydrogenation kinetics at temperatures below 100°C have to be improved. Other hurdles of AB dehydrogenation to be overcome are the concurrent release of volatile impurities (ammonia and borazine) at higher temperatures and the moderate exothermicity that prevents reversibility, which have both been previously reported [2,5].

To solve such difficulties, a promising route consisting of confining AB into mesoporous scaffolds has been recently proposed [5]. This strategy has demonstrated the reduction of activation barriers for hydrogen release upon confinement, speeding up the dehydrogenation reaction, albeit reaction rates are still low for applications. In addition, the formation of borazine is greatly reduced. Finally, the exothermicity of the hydrogen desorption reactions is significantly lowered ($\Delta_R H \approx -1 \text{ kJ} \cdot \text{molH}_2^{-1}$), due to the modification of structural and thermodynamic properties of AB and the non-volatile polymeric products [5].

In this context, the first step to confine AB into porous materials is the dissolution of AB in polar solvents to fill the pores of the host material prior to solvent removal. It is then crucial to find out if the solvent has an effect per se on AB dehydrogenation characteristics before carrying out confinement into porous materials. AB generally offers low solubility with some exceptions as in

the case of water, methanol or THF [6]. Methanol and THF were chosen for this study to confine AB into porous materials through prior dissolution as both solvents are highly volatile allowing easy solvent removal at room temperature to prevent damaging NH_3BH_3 by heating. Actually, methanol and THF have already been used to this purpose [5,7]. We aim investigating the effect of dissolving AB into both solvents as the previous step for AB impregnation into porous materials. As a second part of this chapter, the effect of impregnation onto mesoporous gallium oxide (Ga_2O_3) by incipient wetness impregnation using Methanol and THF dissolution of AB will also be reported.

3.2. Experimental methods

3.2.1 Recrystallization of Ammonia Borane

One gram of AB was dissolved in 15 mL of solvent (methanol or tetrahydrofuran) and left to dry overnight in a hood at room temperature. When recovered, the samples were further dried in a desiccator connected to a vacuum pump for four hours and kept under static vacuum afterwards. The materials thus obtained were labeled as AB-Met and AB-THF for the methanol- and THF-recrystallized AB, respectively.

3.3.2 Ga_2O_3 synthesis

Crystalline mesoporous gallium oxide was synthesized in the presence of non-ionic structure directing agent Pluronic F127 via Self-Assembly Hydrothermal-Assisted (SAHA) method [8]. The mass synthesis ratio was 1: Gallium nitrate hydrate: 0.5 Pluronic F127: 10 Ethanol. The reaction mixture was vigorously stirred (280 rpm) and homogenized for 30 min at 40 °C. The homogeneous gel was then transferred to a 45 mL Teflon®-lined stainless steel vessel and heated under autogenous pressure in static conditions in a conventional oven at 180 °C for 20 h. The resultant white solids were separated from the solution by centrifugation (4.000 rpm, 20 min), washed three times with deionized water and dried overnight at 60 °C. The fine powder was then calcined in air at 350 °C for 6 h yielding mesoporous hollow nanocrystalline gallium oxide spheres displaying cubic-spinel type structure. This sample was provided by prof. Moisés Carreón, at the University of Kentucky (Louisville, USA).

3.2.3 AB Impregnation

AB was impregnated on Ga_2O_3 materials using the same solvents that were used for recrystallization. Prior to impregnation, the Ga_2O_3 materials were dried at 120 °C for 2 hours.

AB-Ga 0.5:1 (Met) preparation: 0.5 g of AB were dissolved in 10 mL of methanol. 1 g of the Ga_2O_3 support was then added to the solution under stirring in an ice bath to prevent the solvent

from evaporating before impregnation. The solution filled the pores of Ga_2O_3 by capillary action. The white solid thus obtained was dried at room temperature in a hood for 24 hours.

AB-Ga 0.5:1 (THF) and AB-Ga 1:1 (THF) preparation: 100 or 200 mg of AB were dissolved in 4 mL of THF. Every 30 minutes, the solution was added stepwise to 200 mg of the Ga_2O_3 support for the porous channels to be filled by capillary action. After each addition, the solid was dried under vacuum for one hour and a new solution aliquot was added. After the last solution addition, the samples were dried under vacuum overnight in a desiccator.

3.2.4 Samples characterization

All the characterization techniques and equipments used in this chapter were previously described in chapter 2.

N_2 adsorption-desorption isotherm analyses were run to compare the textural properties of mesoporous Ga_2O_3 before and after AB impregnation under the conditions described in section 2.2.5. The specific surface area was calculated using the Brunnauer-Emmett-Teller (BET) method [9,10] and pore size distributions were obtained through the Barrett-Joyner-Halenda (BJH) model from the adsorption branches of the isotherms [11]. Before measurements, the samples were pretreated for 16 h under high vacuum at 350 °C for porous Ga_2O_3 and room temperature for impregnated samples, with a final pressure of 7 μm of Hg.

To study the surface and particles characteristics, SEM pictures of AB, AB-Met and AB-THF were obtained.

For compositional analysis of the samples, X-ray intensity data were collected for all the AB samples as well as for Ga_2O_3 support before and after AB impregnation using the Cu-K α (wavelength 0.5406 Å) radiation with $2\theta = 4.0^\circ \sim 90.0^\circ$. Diffraction analyses were scanned with 0.04° steps and accumulation times of 5 s. Crystallites size was obtained in the case of AB materials by Scherrer formula for AB molecules for comparison [12]. ICP/MS analyses of AB samples were also performed by means of a LECO elemental analyzer CHNS-932. Each sample was analyzed three times and the average value is reported. Carbon content is considered as it could reveal possible changes in the composition of AB after being dissolved in methanol or THF. Raman spectra of all the studied materials were acquired using the 785 nm excitation line with 350 mW with a PerkinElmer RamanStation 400F spectrometer.

Thermal analyses of AB materials and their decomposition was also conducted. DSC measurements were performed for AB materials under N_2 flow ($50 \text{ mL} \cdot \text{min}^{-1}$) by using Al pans with pressed Al covers under various heating rates in the range 20-250 °C or under isothermal conditions at 80 °C, 85 °C and 90 °C. TDS/MS analyses were also applied to neat AB to relate thermal events to compositional changes in the sample during thermal decomposition at 0.5

°C·min⁻¹ ramp. These measurements were performed at the Servicio Interdepartamental de Investigación (SIdi) at Universidad Autónoma de Madrid (UAM), some of them being provided by Dr. Fabrice Leardini from the group of Materials for Energy at the Department of Physics (UAM, Madrid). Finally, Operando Raman/MS analyses were performed to further study the thermal decomposition of all the studied materials. 0.075 g of each sample were introduced in the quartz spectroscopic Raman cell previously described in section 2.2.12 (see Figure 2.3 in chapter 2) to run these measurements under 200 mL·min⁻¹ of carrier gas namely, 99.9995 % N₂. Spectra consisted of 30 and 6 accumulations of 10 s acquisition for AB materials and AB impregnated Ga₂O₃ samples respectively, with a spectral range of 95-3500 cm⁻¹ Raman shift. The peak resolution was 2 cm⁻¹ full width half maximum (FWHM).

3.3 Results

3.3.1 N₂ adsorption/desorption isotherms

Textural properties of empty and AB-impregnated samples are reported in Table 3.1, and the pore size distribution and cumulated pore volume of Ga₂O₃ and AB/ Ga₂O₃ (THF) samples are plotted in Figure 3.1.A and Figure 3.1.B, respectively. All isotherms belong to type IV, according to IUPAC classification [9], with clear hysteresis loops, at relative pressures between 0.5 and 0.9, indicative of the mesoporosity of the Ga₂O₃ structure. The support material isotherm presents an adsorption curve rising at relative pressures below 0.4 and its hysteresis loop ranges from 0.5 to 0.9 relative pressures, which illustrates a broad pore size distribution. BJH pore size confirms such broad pore size distribution (Figure 3.1.B), with a maximum near 9.0 nm. The BET specific surface area observed for this mesoporous phase is 150 m²·g⁻¹.

The isotherm curves of the impregnated samples show the general characteristics of mesoporous Ga₂O₃, and the mean pore size remains around 9 nm for all materials. However, through impregnation of AB, the textural properties are significantly reduced (Table 3.1). It can be seen that BET specific surface area decreases from 150 m²·g⁻¹ for mesoporous Ga₂O₃ to 35 m²·g⁻¹ and 29 m²·g⁻¹ for AB/Ga₂O₃ 0.5:1 (THF) and AB/Ga₂O₃ 1:1 (THF), respectively, while the total adsorbed N₂ volume drops from 0.29 cm³·g⁻¹ STP for the support to 0.07 cm³·g⁻¹ STP and 0.09 cm³·g⁻¹ STP for 0.5:1 and 1:1 impregnated samples, respectively. These trends suggest that mesoporous Ga₂O₃ structure is preserved through impregnation but is consistent with pores filling by AB.

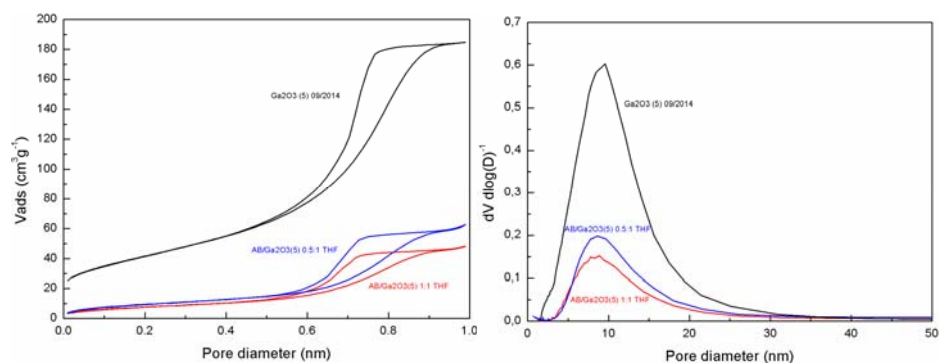


Figure 3.1: (A) N₂ adsorption/desorption isotherms at -196 °C and (B) Pore size distribution for mesoporous Ga₂O₃ and AB/Ga₂O₃ (THF) materials

Table 3.1: Textural Properties of mesoporous Ga₂O₃ and AB/Ga₂O₃ samples

	BET area (m ² ·g ⁻¹)	Pore Volume (cm ³ ·g ⁻¹)	N ₂ ads. Volume (cm ³ ·g ⁻¹)	Pore Diameter (nm)
Ga ₂ O ₃	150	0.29	185	9
AB-Ga 0.5:1 (THF)	29	0.09	63	9
AB-Ga 1:1 (THF)	36	0.07	48	9

3.3.2 Morphological and compositional characterization of ammonia borane samples

Figure 3.2 shows SEM micrographs of the three samples of AB: neat AB and AB recrystallized from THF and methanol solutions. Picture A (1000 magnifications), corresponding to neat AB, shows bonded particles with varied shape and size. A typical particle with flat, hexagonal face can be observed in micrograph B (5000 magnifications). In the case of recrystallized samples (pictures C to F), particles present a flake-like morphology which produces a marked decrease of the apparent density of the material. A hollow aggregate of flat particles can be observed in picture C (AB-Met, 1000 magnifications) while micrograph D (AB-Met, 10000 magnifications) depicts some of the small and flat particles that conform aggregates of AB-Met. Picture E shows the “flake” shape of some particles and micrograph F, the squared flat faces of one particle of AB-THF.

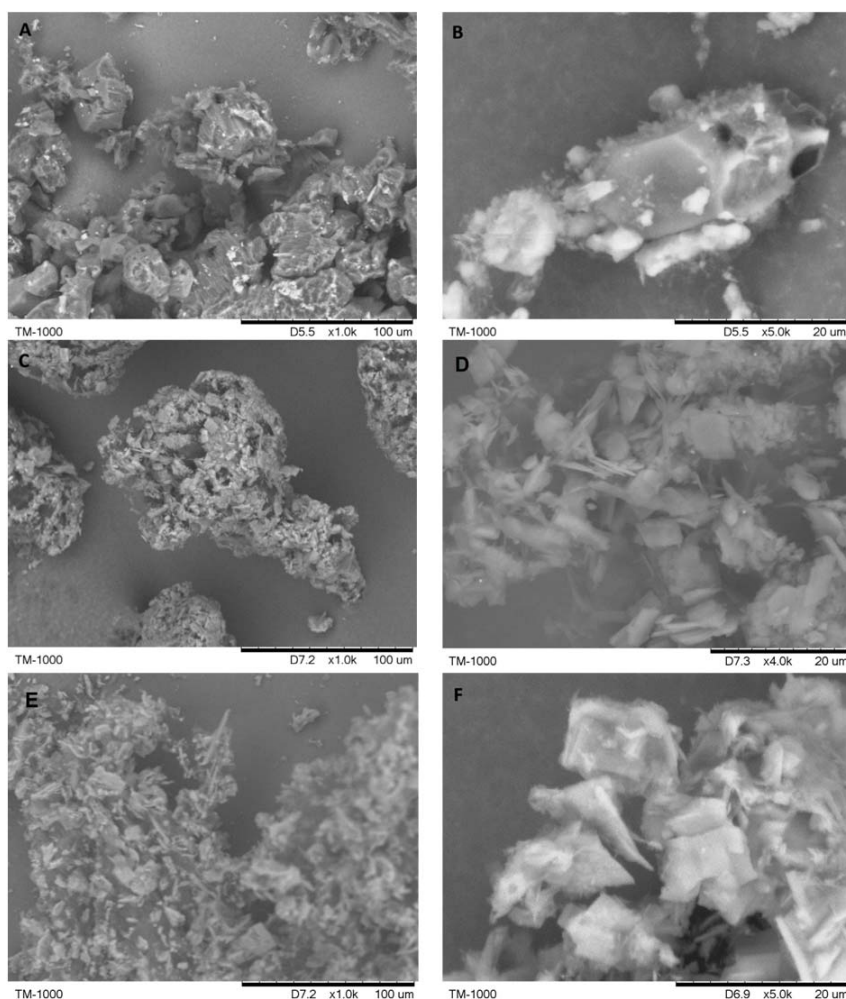


Figure 3.2: SEM micrographs of neat ammonia borane (A,B); AB recrystallized from methanol, AB-Met (C,D) and AB recrystallized from THF, AB-THF (E,F)

The samples structure and composition was further investigated by means of XRD. As it can be seen in Figure 3.3, the diffraction patterns of the three AB samples reveal the main presence of NH_3BH_3 phase (tetragonal $I4mm$ space group). Besides, the main NH_3BH_3 peaks (related to (110) and (200) diffraction planes) in AB-THF sample are shifted to lower diffraction angles ($\sim 0.20^\circ$) compared to the other samples indicating a bigger cell volume in AB-THF sample. Shift could be due to the presence of small amounts of ammonium borane hydrate in sample AB-THF. Concerning the microstructure, AB and AB-THF samples exhibit crystallite size around $\sim 500 \pm$

200 nm estimated with the Scherrer equation [12], while AB-Met shows slightly bigger crystallite sizes of $\sim 800 \pm 300$ nm.

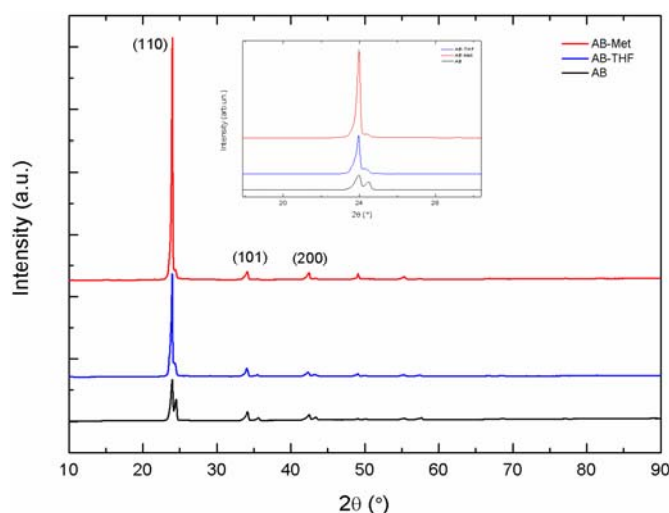


Figure 3.3: XRD pattern of commercial AB (black), AB recrystallized from methanol, AB-Met (red) and AB recrystallized from THF, AB-THF (blue)

On the other hand, Figure 3.4 depicts the XRD patterns of AB/Ga₂O₃ samples and the porous support Ga₂O₃. XRD pattern of the support is formed by two broad peaks at 2θ below 40° and above 60° corresponding to the (311) and (440) planes of spinel-type cubic Ga₂O₃ respectively [8]. It can be seen in the right figure that AB/Ga₂O₃ 1:1 (THF) exhibits NH₃BH₃ peaks with the peaks at $2\theta = 23.88^\circ$ and 24.38° slightly attenuated and partially merged and with no relevant change caused by the support while AB/Ga₂O₃ 0.5:1 (THF) combines diffraction peaks of both NH₃BH₃ and porous Ga₂O₃. Finally, AB/Ga₂O₃ 0.5:1 (Met) XRD pattern is very similar to that of the porous Ga₂O₃ phase with no apparent diffraction caused by NH₃BH₃. This fact suggests that in AB/Ga₂O₃ 0.5:1 (Met), AB particles are too small to produce diffraction which may be due to AB being confined inside Ga₂O₃ pores and forming small aggregates that cannot produce diffraction. On the left figure of Figure 3.4, low angles XRD patterns of the same materials are plotted showing the main diffraction peak around $2\theta = 1^\circ$ characteristic of Ga₂O₃ phase, which seems to be preserved through impregnation.

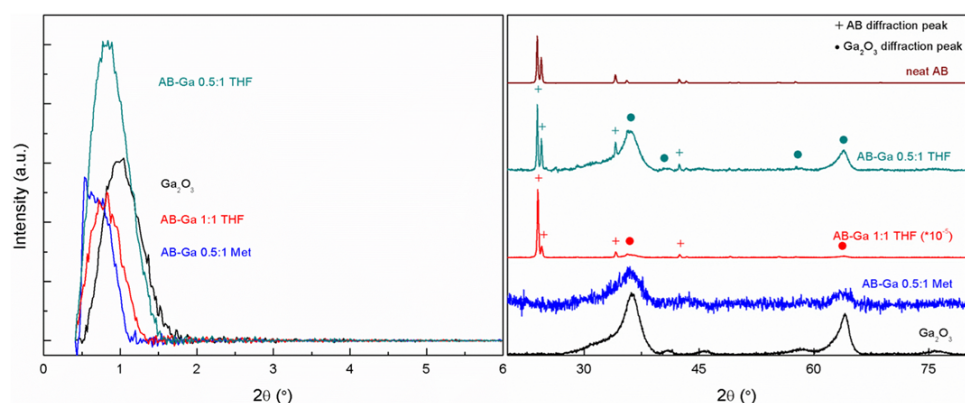


Figure 3.4: Low angles (left) and High angles (right) X-ray Diffraction patterns of neat AB and AB/Ga₂O₃ materials

The resulting values of determining nitrogen and hydrogen content by elemental analysis (ICP/MS) are reported in Table 3.2. It can be seen than for the three materials, carbon content is negligible and Nitrogen and Hydrogen contents are very similar suggesting that none of the solvents introduce impurities upon AB recrystallization.

Table 3.2: N and H content (wt.%) in neat AB, AB-Met and AB-THF samples. In all samples, C content presents residual values below 0.6 wt.%

	%N	%H
AB	41.20 ± 0.3	15.82 ± 0.1
AB-Met	44.56 ± 0.3	16.95 ± 0.1
AB-THF	39.56 ± 0.3	15.18 ± 0.1

To complete compositional study, the Raman spectra of the three AB samples presented in Figure 3.5.A exhibit very similar features to those of AB/Ga₂O₃ materials (Figure 3.5.B), excepting sample AB/Ga₂O₃ 0.5:1 (Met) that presents higher signal-to-noise ratio. Five clearly different spectral regions can be observed in AB Raman spectrum and are present in the spectra from Figure 3.5 [13]. In the N-H stretching zone that lays between 3150 cm⁻¹ and 3350 cm⁻¹, the asymmetric mode is centered at 3321 cm⁻¹, while the symmetric ones appear at 3253 cm⁻¹ and 3175 cm⁻¹. The B-H stretching region, between 2250 cm⁻¹ and 2400 cm⁻¹, shows two modes centered at 2381 cm⁻¹ and 2281 cm⁻¹ for asymmetric and symmetric stretches respectively. A poorly resolved intermediate shoulder can be discerned at 2331 cm⁻¹. N-H deformation region, between 1350 cm⁻¹ and 1600 cm⁻¹, exhibits a band centered at 1600 cm⁻¹, for asymmetric deformation modes and a band at 1377 cm⁻¹ assigned to symmetric deformation modes. The B-H deformation region spreads between 1100 cm⁻¹ and 1275 cm⁻¹. The more intense band at 1189

cm^{-1} is assigned to asymmetric bending modes while that centered at 1161 cm^{-1} corresponds to symmetric ones. Deformation modes in NH_3 and BH_3 groups are primarily caused by umbrella and scissors like movements of hydrogen atoms [13]. The B-N stretching region, between 750 cm^{-1} and 850 cm^{-1} , exhibits two major stretches, the ^{10}B -N one centered at 799 cm^{-1} and the ^{11}B -N one at 783 cm^{-1} . Additionally, a weaker band can be observed at close frequency shifts, 727 cm^{-1} , caused by N-B-H rocking modes.

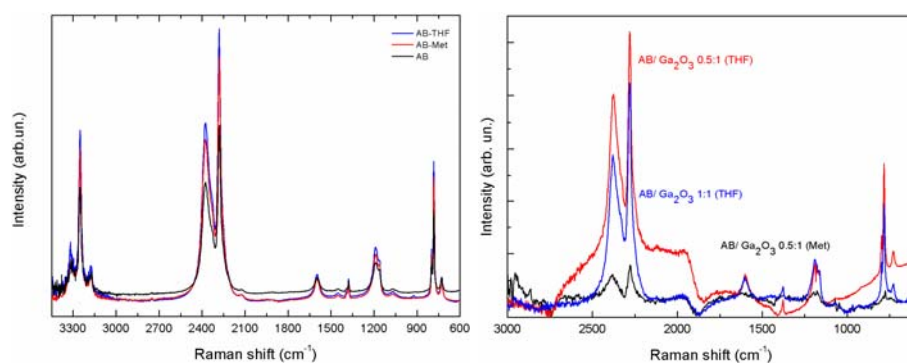


Figure 3.5: (A) Raman spectra of commercial AB (black), AB-Met (red) and AB-THF (blue). (B) Raman spectra of AB/Ga₂O₃ 0.5:1 (Met) (black), AB/Ga₂O₃ 0.5:1 (THF) (red) and AB/Ga₂O₃ 1:1 (THF) (blue)

3.3 Thermal analyses

3.3.1 Thermolysis of ammonia borane

Thermolysis of AB has been investigated by means of DSC and TDS through non isothermal experiments at constant heating rates of $0.5\text{ }^{\circ}\text{C}\cdot\text{min}^{-1}$ and $5\text{ }^{\circ}\text{C}\cdot\text{min}^{-1}$. Figure 3.6 shows the DSC curves recorded at $0.5\text{ }^{\circ}\text{C}\cdot\text{min}^{-1}$ for neat and recrystallized AB while Figure 3.7 displays $0.5\text{ }^{\circ}\text{C}\cdot\text{min}^{-1}$ and $5\text{ }^{\circ}\text{C}\cdot\text{min}^{-1}$ DSC profiles for neat AB. The DSC signal presents two endothermic peaks and two exothermic ones which can be easily observed on the $5\text{ }^{\circ}\text{C}\cdot\text{min}^{-1}$ DSC profile of neat AB in Figure 3.7. These peaks can be de-convoluted from the experimental heat flow for $0.5\text{ }^{\circ}\text{C}\cdot\text{min}^{-1}$ ramp, as shown in Figure 3.8. Table 3.3 summarizes the characteristics of such peaks obtained by this procedure, as well as the underlying processes associated to them.

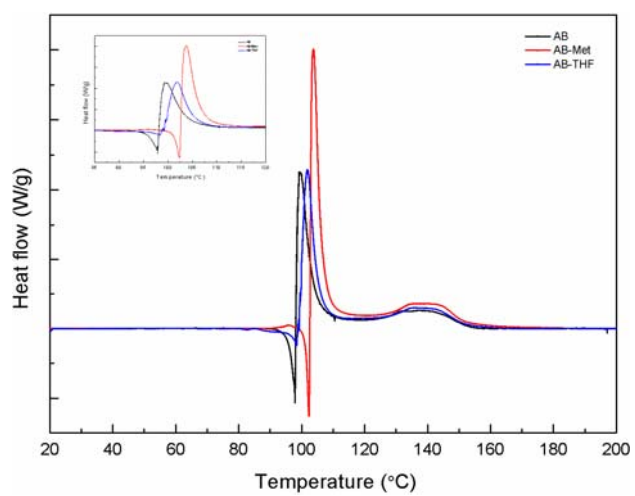


Figure 3.6: DSC curves of AB recorded at a constant heating rate of $0.5\text{ }^{\circ}\text{C}\cdot\text{min}^{-1}$: neat AB (black), AB-Met (red) and AB-THF (blue)

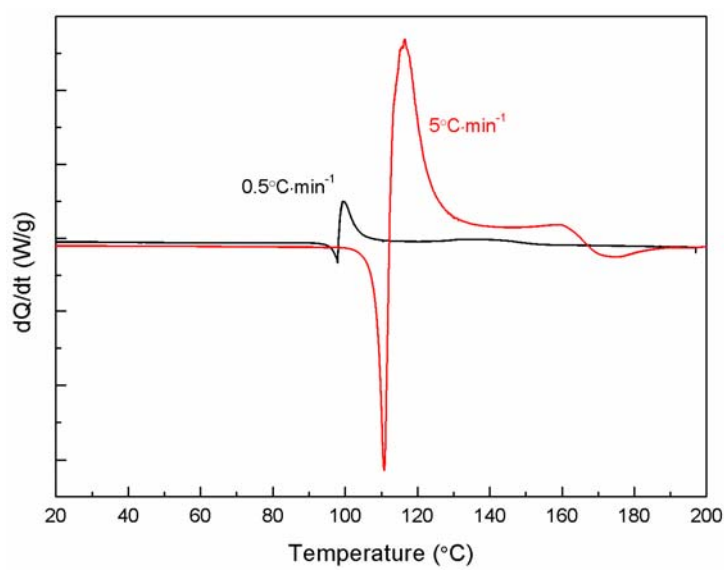


Figure 3.7: DSC curves of neat AB recorded at constant heating rates of $0.5\text{ }^{\circ}\text{C}\cdot\text{min}^{-1}$ (black) and $5\text{ }^{\circ}\text{C}\cdot\text{min}^{-1}$ (red)

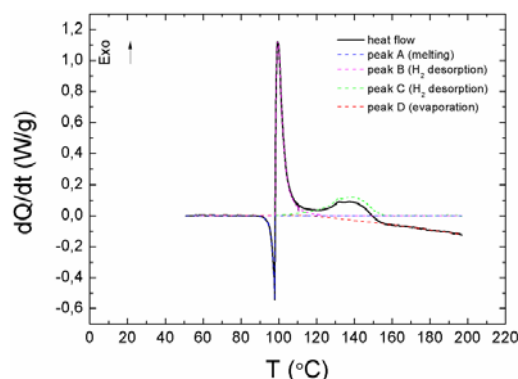


Figure 3.8: DSC curves of AB recorded at a constant heating rate of $0.5\text{ °C}\cdot\text{min}^{-1}$. Four peaks (labelled A-D) have been identified

Table 3.3: Characteristics of the DSC peaks measured at $0.5\text{ °C}\cdot\text{min}^{-1}$ and $5\text{ °C}\cdot\text{min}^{-1}$

Peak label	Tmax (°C)		ΔH (kJ·mol ⁻¹ AB ⁻¹)		Process
	$0.5\text{ °C}\cdot\text{min}^{-1}$	$5\text{ °C}\cdot\text{min}^{-1}$	$0.5\text{ °C}\cdot\text{min}^{-1}$	$5\text{ °C}\cdot\text{min}^{-1}$	
A	97.9	110.8	-3.0 ± 0.1	-6.9 ± 0.2	AB melting
B	99.4	116.5	19 ± 2	-	Reaction (1)
C	141	159.1	10.5 ± 0.9	24.3 ± 0.6	Reaction (2)
D	-	174.8	-	2.0 ± 0.1	Cross linking

The first endothermic peak (labeled as A) is related to AB melting. It is observed in Table 3.3 that the heat associated to this process depends on the applied heating rate as can also be easily seen in Figure 3.7. This could be related to the fact that the heat flow is affected by two simultaneous processes, namely, melting of AB and H₂ desorption. The presence of several exothermic processes in this first step of AB decomposition has already been observed [3]. In fact, peak A occurs simultaneously to the onset of H₂ release, indicating that the kinetics of such process are faster from the liquid than from the solid AB phase.

The two exothermic peaks (labeled as B and C) are related to H₂ desorption by reactions (1) and (2) (see Figure 3.8), respectively and could be completely separated if a suitable heating ramp is applied [1]. The obtained enthalpy for reaction (1) (see Table 3.3) is close to that obtained from isothermal desorption experiments (see next section), and in good agreement with previously reported values [1]. The observed enthalpy of reaction (2) is about $-10\text{ kJ}\cdot\text{mol}^{-1}$ of AB. The observation of a smaller exothermic enthalpy for reaction (2) as compared to (1) is consistent with the higher stability of PAB relative to AB. However, the obtained value is less exothermic than indicated in previous reports [1]. This could be related to the fact that previous determinations of the enthalpy of PAB decomposition were done with samples prepared by slowly decomposing AB

at temperatures below 97 °C [3]. In contrast, the present results have been acquired with a PAB sample obtained by applying a constant heating rate to an AB sample, which melts before decomposing into PAB. Therefore, it is possible that the starting PAB samples have different microstructural properties; thus having an impact on the thermodynamics of H₂ desorption. It is not possible to de-convolute peaks B and C from the DSC run recorded at 5 °C·min⁻¹. Therefore, we can only obtain the whole enthalpy of reactions (1) and (2). The observed value is lower than the sum of those obtained at 0.5 °C·min⁻¹. This effect has been also observed by other authors. Previous calorimetric studies on PAB decomposition (reaction (2)) show that experimental desorption enthalpies decrease with increasing the heating rate [3]. In particular, the enthalpy of reaction (2) is decreased a factor of about 1.5 when comparing measurements performed at 0.1 and 5 °C·min⁻¹ [3]. If we apply this correction factor to the data obtained for reactions (1)+(2), we reach a reasonable agreement with the expected value (of about -45 kJ·mol⁻¹).

The rate of H₂ release calculated by TDS from the MS H₂-ion current I_{H_2} as described in the Experimental section (see section 2.2.8) is plotted in Figure 3.9 as a function of the sample temperature. The hydrogen desorption curve presents three different peaks (labeled 1-3) coming from different reactions. Table 3.4 summarizes the peak temperatures and the hydrogen desorption yields of each one of the three peaks. The obtained data suggest that peak 1 is related to hydrogen desorption by reaction (1) whereas peak 2 corresponds to H₂ release through reaction (2). These peaks occur at temperatures close to those observed for peaks B and C in the DSC experiments. The yield of H₂ released in peak 3 is much lower than those of peaks 1 and 2. This process occurs after the endothermic peak D observed by DSC which has been related to cross linking between PIB molecules [14]. Therefore, peak 3 could be ascribed to H₂ release from PIB formation and PIB cross linking which take place in parallel. At the same time, foaming is observed when removing the samples from the TDS-DSC apparatus.

Table 3.4: Characteristics of the desorption peaks observed in TDS experiments of AB

Peak	Tmax (°C)		Yield (moles desorbed·mol AB ⁻¹)		Process
	0.5 °C·min ⁻¹	5 °C·min ⁻¹	0.5 °C·min ⁻¹	5 °C·min ⁻¹	
H ₂ -peak 1	99.4±0.5	108.2	1.02±0.05	1.02±0.05	Reaction (1)
H ₂ -peak 2	139.0±0.5	149.8	1.10±0.05	1.05±0.05	Reaction (2)
H ₂ -peak 3	162.0±0.5	175.7	0.26±0.02	0.20±0.02	H ₂ release from PIB
B ₂ H ₆	142±1	153±1	~0.05	~0.07	PAB decomposition
C-(NHBH) ₃	148±2	157±2	~0.02	~0.03	PAB decomposition

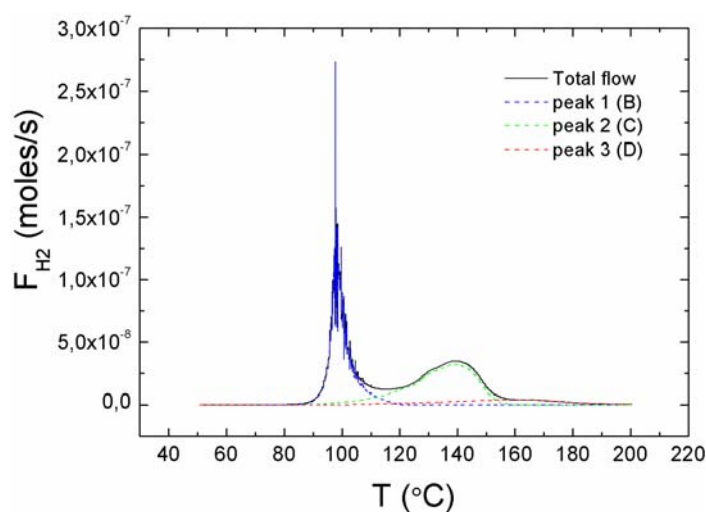


Figure 3.9: Hydrogen flow (expressed in moles of H_2 per second per mol of AB) desorbed from neat AB heated at a constant rate of $0.5\text{ }^{\circ}\text{C}\cdot\text{min}^{-1}$. The curves have been de-convoluted in three peaks (1-3) corresponding to different reactions

Activation energies of reactions (1) and (2) have been obtained by analyzing the dependence of the temperatures of DSC and TDS peaks with the applied heating rate, according to the Kissinger method [15,16], as shown in Figure 3.10. The obtained activation energies for reactions (1) and (2) are $150\pm 10\text{ kJ}\cdot\text{mol}^{-1}$ and $155\pm 10\text{ kJ}\cdot\text{mol}^{-1}$, respectively. There are still some discrepancies on the activation energy for AB thermal decomposition reaction [17] and the result for the first step is very close from some previously reported values [18,19] but slightly lower than others [5,20,21]. These calculations were provided by Dr. Fabrice Leardini from the group of Materials for Energy at the Department of Physics (UAM, Madrid).

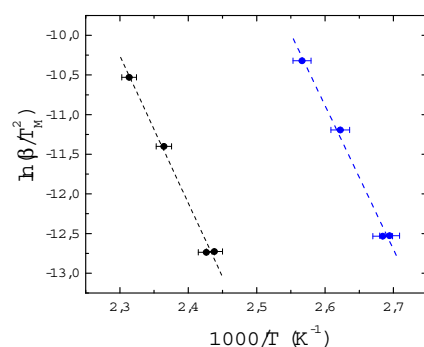


Figure 3.10: Kissinger plots of TDS and DSC peaks corresponding to reactions (1) (blue points) and (2) (black points). The slopes of the least square fit of the experimental data (dashed lines) are proportional to the apparent activation energy of AB and PAB decompositions

3.3.2 Influence of the recrystallization from different solvents (methanol and THF) on decomposition of AB

Thermal decomposition of recrystallized AB samples has also been studied by DSC through ramp experiments at $0.5\text{ }^{\circ}\text{C}\cdot\text{min}^{-1}$. The DSC curves for neat and recrystallized AB at $0.5\text{ }^{\circ}\text{C}\cdot\text{min}^{-1}$ are represented in Figure 3.6 and show the two expected exothermic events that correspond to the two consecutive steps of decomposition of AB as stated earlier. At temperatures below $120\text{ }^{\circ}\text{C}$, the tendency of the three curves confirms in general what was reported elsewhere [1]. Specifically, the calorimetric curves for the three materials show first an endothermic event, related to melting prior to the exothermic processes due to first decomposition step and polymerization of aminoborane [1]. In the case of AB-Met, the endothermic effect preceding the main exothermic event is much more pronounced and starts at higher temperature than for neat AB and AB-THF while such endothermic peak is hardly appreciable for AB-THF. For the second thermal event between $120\text{ }^{\circ}\text{C}$ and $160\text{ }^{\circ}\text{C}$, there is apparently no difference between the three compounds.

Enthalpies calculated for the three materials are listed in Table 3.5. For the first decomposition step, corresponding to reaction (1), AB-Met exhibits a higher enthalpy than neat AB and AB-THF. In the case of the second decomposition step through reaction 2, the three materials show similar enthalpy values which are smaller than those corresponding to the first decomposition step. This is consistent with the higher stability of PAB as compared to AB.

The high similarity in calorimetric results for the second hydrogen loss step of the three samples suggests the three decomposed materials exhibit very similar features after the first decomposition step. Moreover, for a practical use of AB as a hydrogen storage material, the decomposition temperature would ideally be of $85\text{ }^{\circ}\text{C}$, the working temperature of fuel cells [22]. Therefore in next section, a detailed analysis will be focused on thermal behavior and hydrogen release of neat and recrystallized AB at temperatures below $100\text{ }^{\circ}\text{C}$.

Table 3.5: Characteristics of the DSC peaks observed during $0.5\text{ }^{\circ}\text{C}\cdot\text{min}^{-1}$ ramp DSC experiments of neat and recrystallized AB

	Tmax ($^{\circ}\text{C}$)	ΔH ($\text{kJ}\cdot\text{mol}^{-1}\text{ AB}^{-1}$)	Tmax ($^{\circ}\text{C}$)	ΔH ($\text{kJ}\cdot\text{mol}^{-1}\text{ AB}^{-1}$)
neat AB	99.4	19.0 ± 2.0	141	10.5 ± 0.8
AB-Met	103.4	29.7 ± 3.0	141.7	8.0 ± 0.8

AB-THF	101.9	24.8±2.0	140.5	6.7±0.7
--------	-------	----------	-------	---------

3.3.3 Isothermal hydrogen release at temperatures below the melting temperature of ammonia borane

The thermal decomposition of AB under isothermal conditions has been studied by MS coupled with TGA at 80 °C, 85 °C and 90 °C. Figure 3.11 represents MS H₂ profiles for the three samples. As was to be expected in this temperature range, only one step is observed for hydrogen release, corresponding to reaction (1). H₂ desorption is slower as temperature decreases from 90 °C to 80 °C for each sample. At 90 °C, H₂ desorption rate is quite similar for the three materials, whereas at 85 °C and 80 °C, AB-Met desorbs H₂ slower than neat AB and AB-THF.

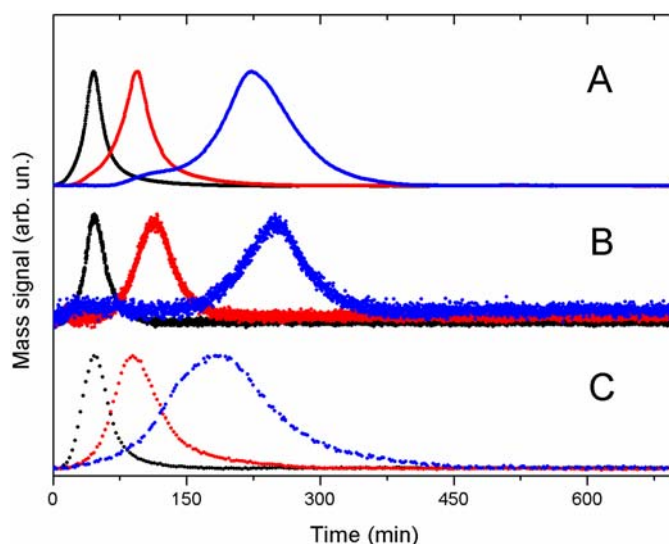


Figure 3.11: MS curves registered for neat AB (A), AB-Met (B) and AB-THF (C) at 80 °C (blue), 85 °C (red) and 90 °C (black)

Additionally, the decomposition of the three AB samples to yield PAB (reaction (1)) has been investigated by means of DSC under isothermal conditions at 80, 85 and 90 °C and DSC curves are plotted in Figure 3.12. As was to be expected, a single H₂ desorption peak is observed at each temperature, which is related to reaction (1) and kinetics of this process has been investigated by assuming a constant enthalpy of H₂ desorption. Under this assumption, the time integrals of the heat flow signals are directly proportional to the reacted fraction and Arrhenius treatment is applied to DSC isothermal data to provide the activation energy for reaction (1) as shown in Figure 3.13. The activation energy thus obtained as well as the enthalpy from

integration of the DSC peaks at 90 °C are listed in Table 3.6 where it can be observed that activation energies are lower for neat AB than for recrystallized samples. As can be seen in Figure 3.12, the thermal event is slower as temperature decreases from 90 °C to 80 °C. At each temperature, the time corresponding to the maximum in the DSC curve is very similar for neat AB and AB-THF. In the case of AB-Met, lower times are observed for the maximum in the DSC curve to be reached at 85 °C and 80 °C compared to the others. For neat AB, once the reaction get started, it proceeds faster and so a lower E_{act} is obtained for neat AB compared to AB-Met and AB-THF. From isothermal MS and TGA decomposition data, an extent of reaction-time relationship was obtained in each case and Arrhenius treatment was applied to determine the value of activation energy. The results are also given in Table 3.6 where it can be seen that MS and TGA activation energies are very similar in each case.

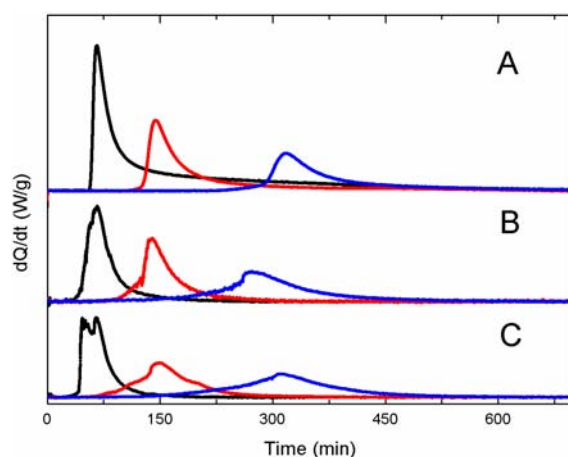


Figure 3.12: Isothermal DSC curves for neat AB samples (A), AB-Met (B) and AB-THF (C) at 80°C (blue), 85°C (red) and 90°C (black)

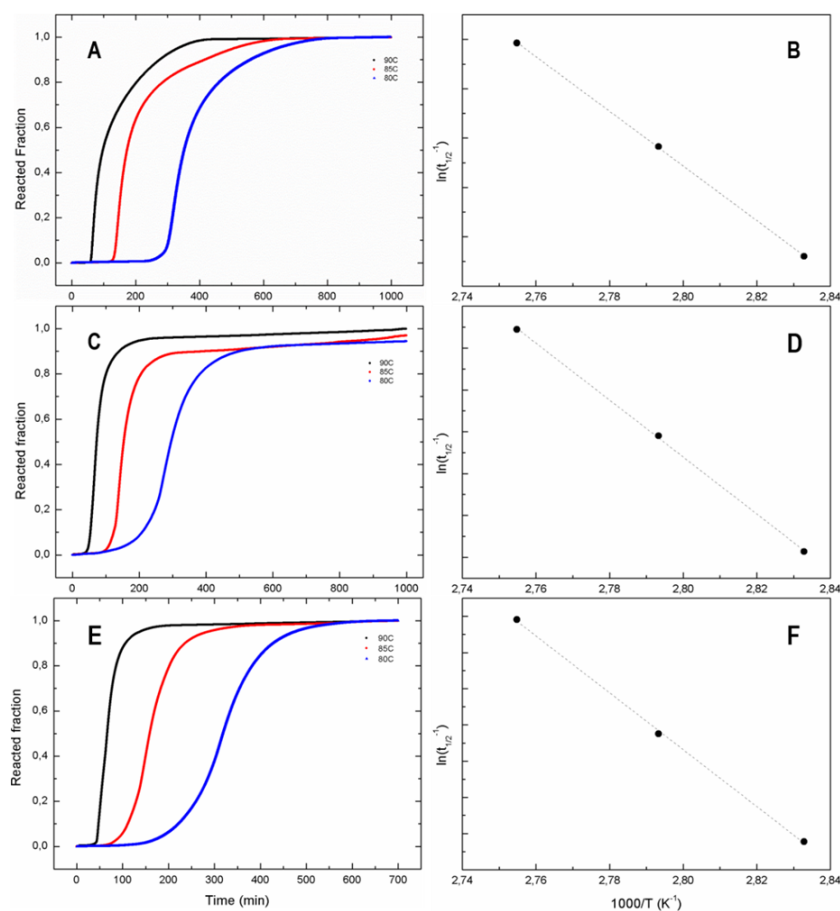


Figure 3.13: (left) Time evolution of the reacted AB fraction at different temperatures obtained from the time integral of DSC curves shown in Figure 3.12 and (right) Arrhenius plot of the time for half conversion of AB-material into PAB versus the inverse of the absolute temperature for neat AB (A and B), AB-Met (C and D) and AB-THF (E and F)

Table 3.6: Activation energy ($E_{act}(DSC)$) and enthalpy (ΔH) obtained from the isothermal DSC experiments shown in Figure 3.12. Activation energy obtained from applying Arrhenius treatment to MS ($E_{act}(MS)$) and TGA data ($E_{act}(TGA)$)

	ΔH (kJ·mol AB ⁻¹)	$E_{act}(DSC)$ (kJ·mol AB ⁻¹)	$E_{act}(MS)$ (kJ·mol AB ⁻¹)	$E_{act}(TGA)$ (kJ·mol AB ⁻¹)
neat AB	28.64±3	113±11	165	177
AB-Met	22.60±2	150±15	183	183
AB-THF	18.72±2	167±17	180	190

3.3.4 H₂ release from ammonia borane loaded inside Ga₂O₃

Figure 3.14 shows the H₂ MS profiles acquired at a 1 °C·min⁻¹ ramp for the AB/Ga₂O₃ materials, which exhibit varied evolutions. AB/Ga₂O₃ 0.5:1 (Met) MS profile displays only one desorption

peak between 30 °C and 90 °C with a very high raising stretch up to 71 °C. The AB/Ga₂O₃ 1:1 (THF) curve shows a H₂ desorption profile very similar to that of neat AB also plotted on Figure 3.14, exhibiting two clearly separated dehydrogenation steps that spread between 60 °C and 125 °C and 125 °C and 170 °C. The only observable differences with respect to neat AB profile are the lower temperature onset of the first dehydrogenation and the bigger amount of desorbed H₂ during the second step relative to the first step for Ga₂O₃ 1:1 (THF). Somewhere in between, the H₂ desorption curve obtained for AB/Ga₂O₃ 0.5:1 (THF) exhibits only one hydrogenation event between 20 °C and 120 °C with a slower raising stretch than AB/Ga₂O₃ 0.5:1 (Met) MS profile. Impregnation of AB on porous Ga₂O₃ with a 0.5:1 mass ratio seems to have an important destabilizing effect as H₂ desorption for AB/Ga₂O₃ 0.5:1 (Met) and AB/Ga₂O₃ 0.5:1 (THF) starts at temperatures as low as 20 °C taking place through a one-step mechanism. When impregnation mass ratio is raised to 1:1, almost no changes are observed with respect to neat AB dehydrogenation profile as shown in Figure 3.14. This may probably be due to excessive AB blocking the pores entrance on Ga₂O₃ surface.

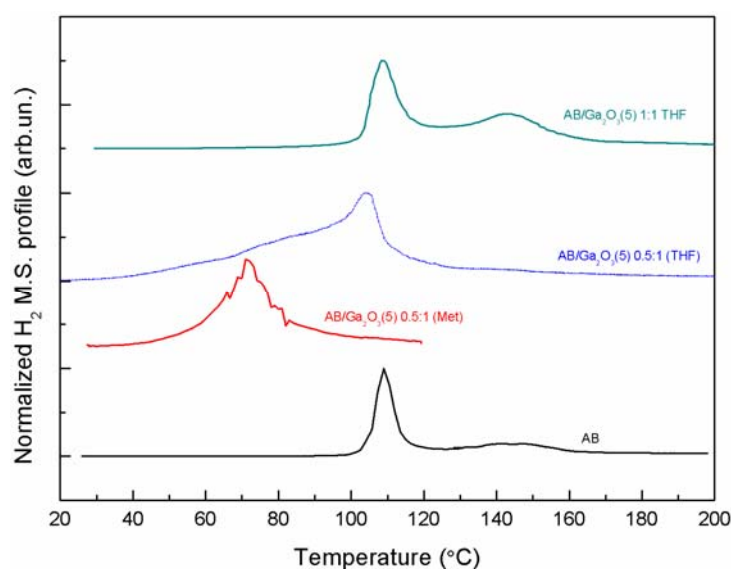


Figure 3.14: Normalized H₂ mass profiles corresponding to thermal decomposition of AB/Ga₂O₃ samples under a ramp of 1°C·min⁻¹

3.3.4 Operando Raman-MS

The Raman spectra of the neat and recrystallized AB samples were acquired after 30 minutes at 90 °C and are represented in Figure 3.15. On one hand, acquiring spectra after 30 minutes allows to make sure the material temperature is homogeneous at 90 °C and no gradient occurs along

the spectroscopic cell axis and, secondly, they are still identical to those acquired at room temperature (see Fig. 3.5), except for a slight change in the BN stretching band described next. As it can be seen in Figure 3.15, there is no noticeable difference between the spectra of the three materials. As described earlier, each spectrum can be divided in five regions defined by their molecular nature: the N-H stretching region (3150 cm^{-1} - 3350 cm^{-1}), B-H stretching region (2250 cm^{-1} - 2400 cm^{-1}), N-H rock and bends (1350 cm^{-1} - 1600 cm^{-1}), B-H rock and bends (1100 cm^{-1} - 1275 cm^{-1}) and B-N stretching region (750 cm^{-1} - 850 cm^{-1}) [13].

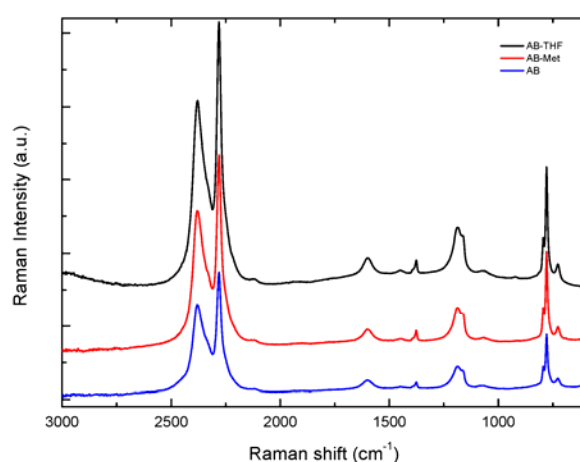


Figure 3.15: Raman spectra for neat AB (black), AB-Met (red) and AB-THF (blue) after 30 minutes at 90 °C

Operando Raman-MS technique allows studying the thermal decomposition of the samples. Few differences are observable in the tendency of the Raman spectra throughout thermal decomposition and structural evolution seems very similar for the three materials. As structural changes seem easier to detect from AB-Met spectra, these are more thoroughly described next. Figures 3.16 to 3.18 represent Raman spectra, Raman intensity contour and hydrogen, diborane (B_2H_6) and ammonia (NH_3) MS profiles simultaneously acquired for neat AB, AB-Met and AB-THF during thermal decomposition at 90 °C. Diborane and ammonia represent volatile impurities that have been reported to be released during AB decomposition as well as borazine ($\text{N}_3\text{N}_3\text{H}_6$) as described earlier. But no trace of this last compound has been detected in the 90 °C isothermal experiments as this gaseous impurity is usually released during reaction (2). Figure 3.17.A shows that the AB-Met spectra only exhibit slow intensity loss until 180 minutes after reaching 90 °C. Very quick spectral changes take place between 180 minutes and 200 minutes as all the Raman bands, following a general tendency, swiftly loose intensity. Such transformations are simultaneous to the steeper raising stretch of the unique desorption peak of H_2 MS profile which

takes place between 66 minutes and 212 minutes after reaching 90 °C. Spectral changes simultaneous to the decreasing stretch of H₂ MS profile, between 212 minutes and 400 minutes, are much weaker. Besides the desorption step observed for H₂, a small NH₃ release can be seen to take place 35 min after reaching 90 °C in Figure 3.16.B while no clear tendency is shown by B₂H₆ MS profiles.

For comparison purposes, Raman spectra of DADB, provided by Autrey's group from Pacific Northwest National Laboratory and fresh and spent AB-Met are plotted in Figure 3.19.

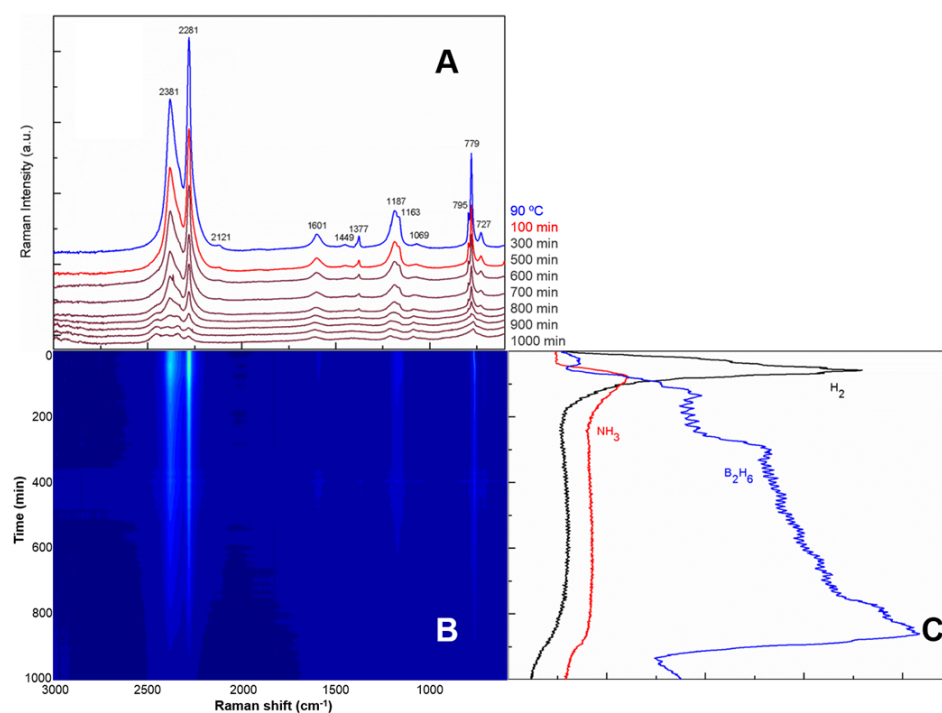


Figure 3.16: Representative Raman spectra (A), Raman intensity contour vs temperature (B) and simultaneous MS profiles for H₂ and other volatile components (C) acquired during neat AB thermal decomposition at 90 °C

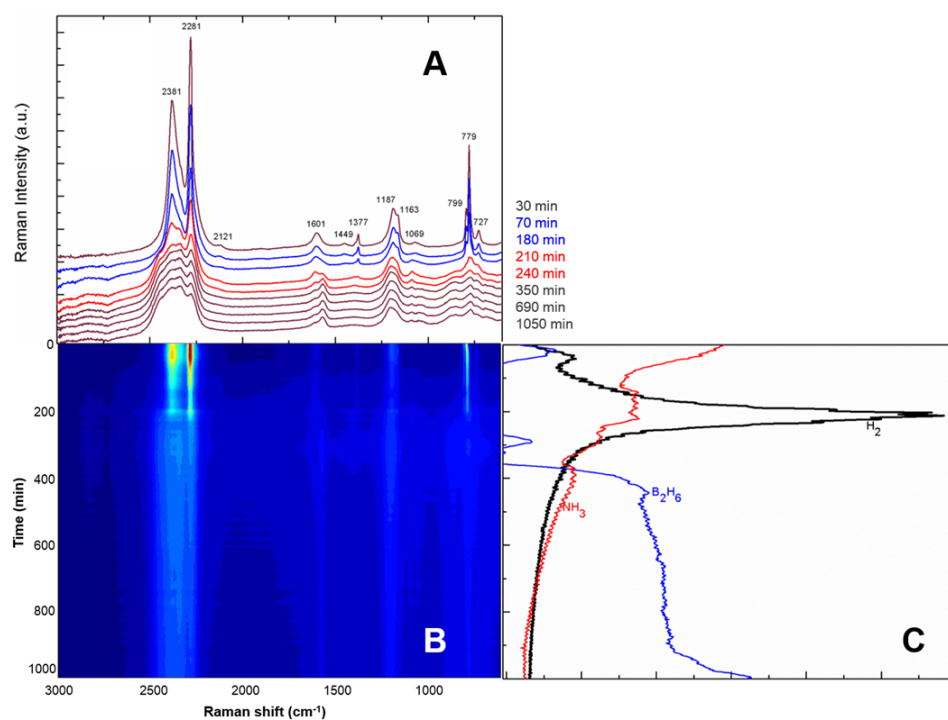


Figure 3.17: Representative Raman spectra (A), Raman intensity contour vs temperature (B) and simultaneous MS profiles for H₂ and other volatile components (C) acquired during AB-Met thermal decomposition at 90 °C

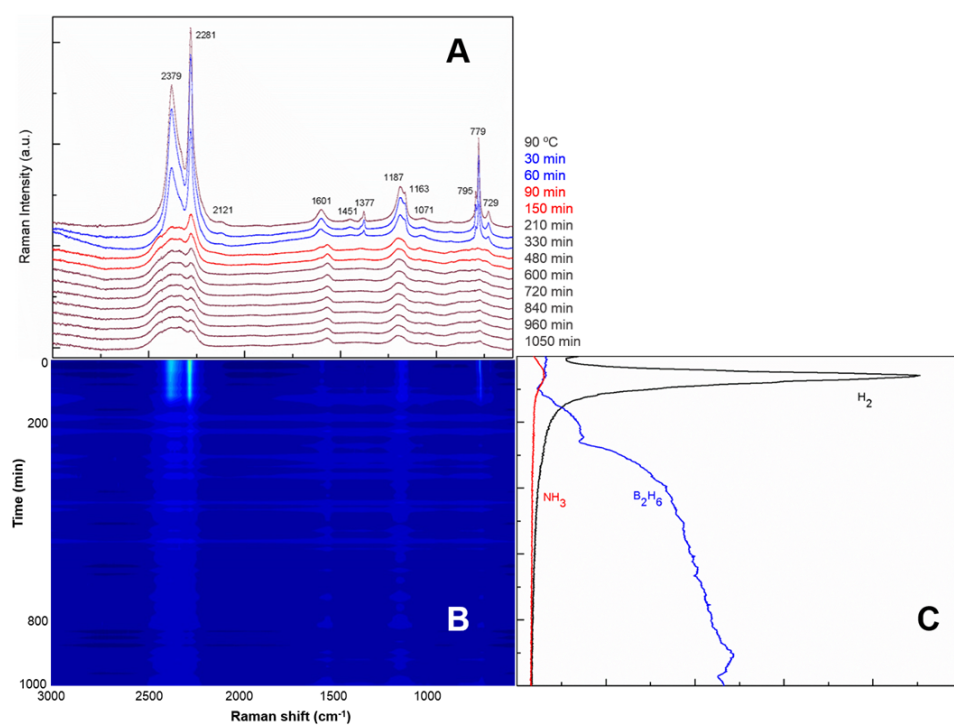


Figure 3.18: Representative Raman spectra (A), Raman intensity contour vs temperature (B) and simultaneous MS profiles for H₂ and other volatile components (C) acquired during AB-THF thermal decomposition at 90 °C

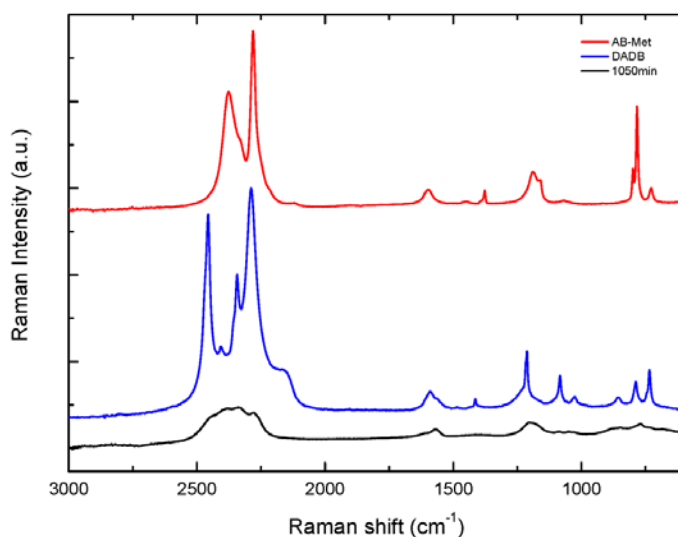


Figure 3.19: Raman spectra for AB-Met (red), DADB from PNNL (blue) and spent AB-Met (black)

In the B-H stretching region, the shoulder centered at 2341 cm⁻¹ gets higher in intensity relative to $\nu_{as}(B-H)$ at 2381 cm⁻¹ and $\nu_s(B-H)$ at 2281 cm⁻¹ [23,13,24] and a shoulder appears at 2449 cm⁻¹ after 210 minutes. The band $\nu_{as}(B-H)$ centered at 2381 cm⁻¹ disappears after 300 minutes while the shoulders at 2449 cm⁻¹ and 2341 cm⁻¹ and the band $\nu_s(B-H)$ at 2281 cm⁻¹ persist for longer. These final modes suggest the presence of DADB (see Figure 3.19) or B=N bounds [25].

In the N-H deformation region, the band $\delta_{as}(N-H)$ at 1601 cm⁻¹ [13,24] first exhibits a red shift to 1599 cm⁻¹ after 180 minutes which is close to that observed at 1595 cm⁻¹ for DADB spectrum (see Figure 3.19). 200 minutes after reaching 90 °C, the band splits into two others modes centered at 1605 cm⁻¹ and 1569 cm⁻¹. After 300 minutes, the band at 1605 cm⁻¹ disappears while the one centered at 1569 cm⁻¹ gets higher in intensity. This remaining mode is consistent with the presence of NH₂ from PAB molecules. The overtone centered at 1450 cm⁻¹ and the band $\delta_s(N-H)$ at 1377 cm⁻¹ disappear completely after 210 minutes.

In the B-H deformation region, the bands $\delta_{as}(B-H)$ and $\delta_s(B-H)$ centered at 1187 cm⁻¹ and 1163 cm⁻¹ respectively quickly loose intensity and broaden from 180 minutes after reaching 90 °C until merging completely 30 minutes later. The new band that remains at 1193 cm⁻¹ is typical of BH₂ groups from PAB [26]. The vibrational mode $\delta_{as}(N-B-H)$ centered at 1067 cm⁻¹ shows a blue shift to 1087 cm⁻¹ after 180 minutes and remains unchanged afterwards while the bending mode

centered at 1193 cm^{-1} remains and blueshifts (1205 cm^{-1}). Again, this suggests two different environments for B-H groups and the presence of cyclic B-N-H groups [27,28].

In the B-N stretching region, an early shift is observable for both the band $\nu(^{10}\text{B-N})$, at 799 cm^{-1} , and the band $\nu(^{11}\text{B-N})$, centered at 783 cm^{-1} . Both vibrational modes show first a red shift to 797 cm^{-1} and 781 cm^{-1} , respectively, between $35\text{ }^{\circ}\text{C}$ and $55\text{ }^{\circ}\text{C}$ (Figure 3.20). Such an early transformation in the spectrum could be due to the apparent contraction of B-N distance, which takes place when the temperature increases above room temperature [29,30]. Further red shift to 795 cm^{-1} and 779 cm^{-1} is observable between $58\text{ }^{\circ}\text{C}$ and $81\text{ }^{\circ}\text{C}$, and both bands remain centered at these Raman shifts until 180 minutes after reaching $90\text{ }^{\circ}\text{C}$. The band $\nu(^{10}\text{B-N})$, at 795 cm^{-1} which is very close to that at 790 cm^{-1} in DADB spectrum (see Figure 3.19) loses intensity from 180 minutes until disappearing 20 minutes later. The band $\nu(^{11}\text{B-N})$, at 779 cm^{-1} , also starts losing intensity after 180 minutes. 30 minutes later, the only bands that remain are the one centered at 773 cm^{-1} , suggesting that the B-N bond may considerably weaken. A weak shoulder at 857 cm^{-1} , which may be caused by the remaining AB molecules polymerization, has also been observed by IR spectroscopy [25] and the presence of PAB [Supp. Inf. In 26]. The vibrational mode $\delta_{\text{as}}(\text{N-B-H})$ at 727 cm^{-1} also disappears between 180 and 200 minutes at this temperature. During the decrease of H_2 MS profile, there is further red shift of the main band to 769 cm^{-1} .

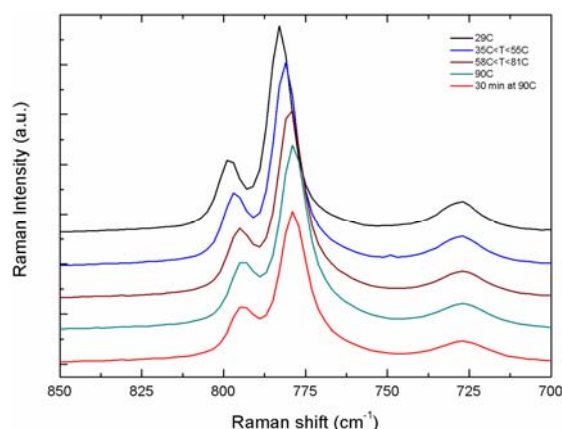


Figure 3.20: First changes for B-N stretching mode in AB-Met during thermal decomposition

In the case of neat AB, the changes described for AB-Met spectra are also detected, excepting the appearance of the bands at 1069 cm^{-1} and the shoulder at 857 cm^{-1} (see Figure 3.16.A), but mainly take place between 500 min and 700 min after reaching $90\text{ }^{\circ}\text{C}$, at much longer times than for AB-Met. On the other hand, the only dehydrogenation step observed by MS starts before reaching $90\text{ }^{\circ}\text{C}$ and lasts up to 200 min, in a very similar time range than for AB-Met while a small

NH₃ release can be seen to take place 35 min after reaching 90 °C in Figure 3.16.B and no clear tendency is shown by B₂H₆ MS profiles. During AB-THF decomposition, Raman spectra evolution in Figure 3.18.A is very similar to that happening for AB-Met but mainly taking place between 60 min and 90 min after reaching 90 °C, at much shorter times. The only observable H₂ desorption happens between 10 min and 200 min after reaching 90 °C, in a similar way to neat AB and AB-Met and nor B₂H₆ neither NH₃ are registered during the measurement.

AB/Ga₂O₃ materials deliver very similar behaviors but at a 1 °C·min⁻¹ ramp. The results are plotted in Figures 3.21 to 3.23. Room temperature Raman spectra for these materials show the features described for AB samples but exhibiting considerable distortion due to Ga₂O₃ presence. For AB/Ga₂O₃ 0.5:1 (THF) Raman spectra in Figure 3.21, noticeable changes can be seen at temperatures as low as 38.5 °C, simultaneously to the quick raise in H₂ MS profile between 30 °C and 140 °C. Around 80 °C, when H₂ release speed seems to be highest, resolution in Raman acquisition gets lost and only CSi signal can be registered from then on. Considering the usual impurities released during neat AB thermal decomposition, only a small NH₃ desorption simultaneous to H₂ release can be detected while nor B₂H₆ neither N₃N₃H₆ are registered during the measurement. The Raman spectra corresponding to AB/Ga₂O₃ 1:1 (THF) in Figure 3.22 do not show any change up to 97.5 °C, just when H₂ MS profile starts increasing very quickly to give rise to two consecutive desorption steps, very similar to those observed during neat AB decomposition (see section 4.3.2.1). The MS profiles for B₂H₆ and N₃N₃H₆ are completely flat during the whole temperature range while NH₃ curve exhibits a small desorption event between 100 °C and 120 °C, simultaneously to the first H₂ peak. AB/Ga₂O₃ 0.5:1 (Met) room temperature Raman spectrum in Figure 3.23 is the one that displays the strongest distortion due to Ga₂O₃ phase, as already mentioned, and little change with temperature raise. The most intense bands caused by B-H stretching modes at 2387 cm⁻¹ and 2375 cm⁻¹ lose intensity from room temperature to 72.5 °C while a shoulder concomitantly raises near 1975 cm⁻¹. In the corresponding MS plot, the NH₃ profile shows considerable desorption through one step simultaneous to H₂ release while the curves corresponding to B₂H₆ (diborane) and N₃N₃H₆ (borazine) remain flat during acquisition.

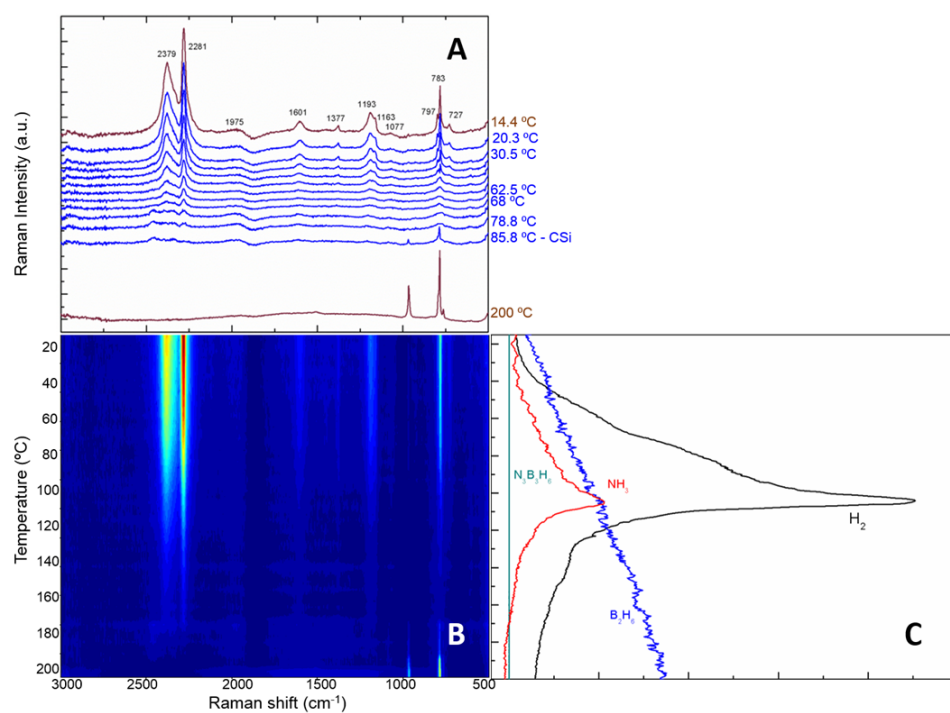


Figure 3.21: Representative Raman spectra (A), Raman intensity contour vs. temperature (B) and simultaneous MS profiles for H₂ and other volatile components (C) acquired during thermal decomposition of AB/Ga₂O₃ 0.5:1 (THF) under a ramp of 1 °C·min⁻¹

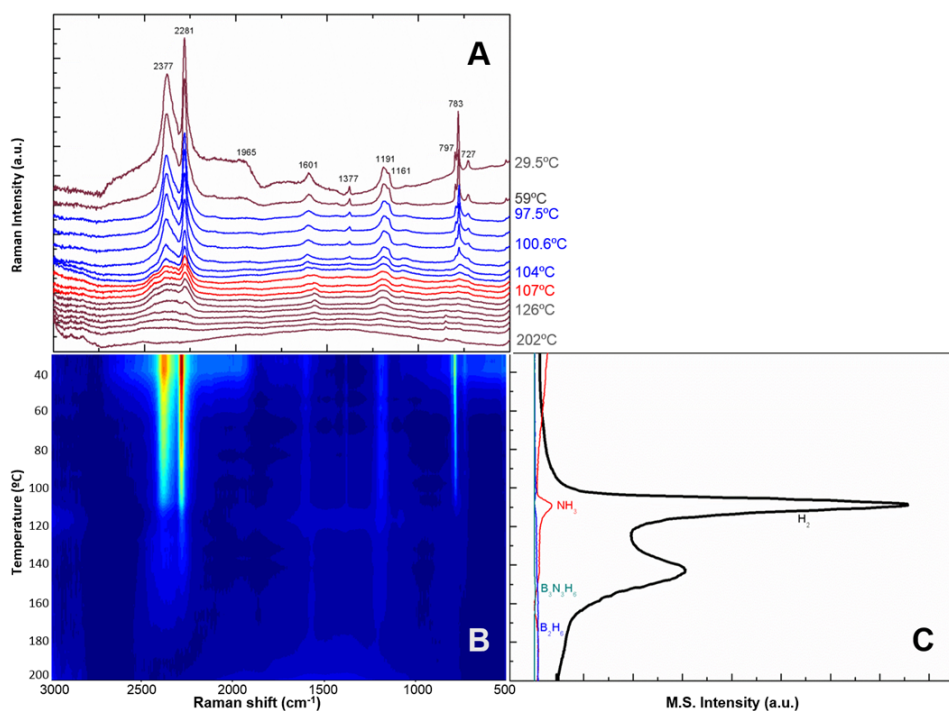


Figure 3.22: Representative Raman spectra (A), Raman intensity contour vs. temperature (B) and simultaneous MS profiles for H₂ and other volatile components (C) acquired during thermal decomposition of AB/Ga₂O₃ 1:1 (THF) under a ramp of 1 °C·min⁻¹

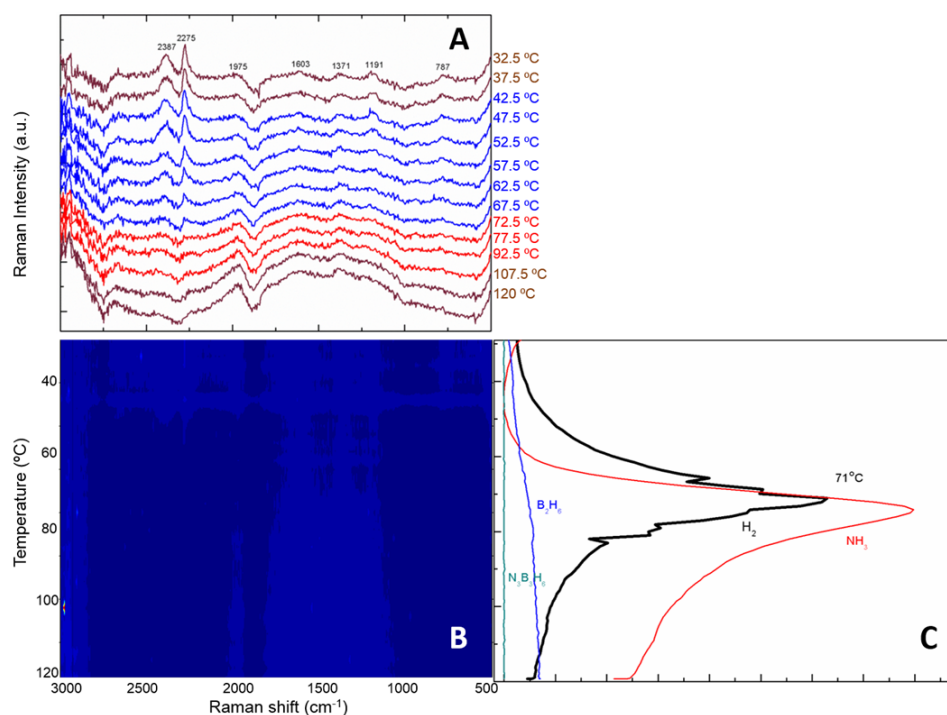


Figure 3.23: Representative Raman spectra (A), Raman intensity contour vs. temperature (B) and simultaneous MS profiles for H₂ and other volatile components (C) acquired during thermal decomposition of AB/Ga₂O₃ 0.5:1 (Met) under a ramp of 1 °C·min⁻¹

3.4. Discussion

The results above indicate that only subtle differences can be observed between recrystallized and neat AB regarding thermal behavior as these materials seem nearly identical at room temperature. There are apparently no structural differences between the AB samples as these deliver the same XRD patterns of NH₃BH₃ and ICP/MS and Raman spectroscopy measurements reveal that composition and structure do not change upon recrystallization. However, SEM pictures show an apparently lower density for recrystallized AB particles which seem to offer a less compact texture. This may be due to some lixiviation effect caused by the solvent on AB.

The more noticeable differences on the effect of both solvents is apparent during thermal analyses as AB-Met displays different decomposition properties either under ramp or isothermal measurements. As previously mentioned, during the first ramp decomposition step, AB-Met seems to be stable up to 100 °C, unlikely neat AB and AB-THF. Then, a much stronger endothermic event previous to decomposition reactions occurs, it has been assigned to melting. The first decomposition step for AB-Met analysis exhibits a higher exothermic character than neat

AB and AB-THF DSC profiles. In the case of AB-THF, the endothermic effect associated to melting is hardly observable. During isothermal DSC measurements, it seems that at temperatures under 90 °C, AB-Met exothermic peak raises more quickly than in the cases of neat AB and AB-THF. On the other hand, MS isothermal profiles on Figure 3.10 shows that H₂ desorption takes longer at 85 °C and 80 °C for AB-Met compared to neat AB and AB-THF, which is consistent with the higher melting temperature observed for AB-Met as AB dehydrogenation seems to be favored from the melted phase. This suggests that some other physical process may take place prior to dehydrogenation reactions during AB-Met decomposition which also justifies the differences observed in the DSC profiles obtained at a 0.5 °C·min⁻¹ ramp (see Figure 3.6). The occurrence of several thermal processes during AB decomposition that seems more obvious during AB-Met decomposition has already been reported elsewhere [1]. The Raman spectra during isothermal decomposition at 90 °C for the three AB samples offer small differences while the simultaneous H₂ MS profiles are almost identical, showing a unique desorption step that ends around 200 minutes. AB-THF structural changes happen much quicker, between 60 min and 90 min, which may be related to the low melting enthalpy detected by DSC for this sample. These Raman changes are in contrast observed at much higher time for neat AB, happening between 500 and 700 min after reaching 90 °C and between 180 and 200 min for AB-Met. The mechanism proposed by Autrey et al. [31,32] includes an induction period during which AB gives rise to a more mobile ammonia borane species AB*, a nucleation event that is the formation of diammoniate of diborane (DADB), more reactive than AB and a growth period where DADB reacts with unreacted AB to form a mixture of polyaminoborane oligomers [31,32]. The *operando* results may be representative of such mechanism as, before H₂ release gets started, the gradual loss of intensity of AB Raman bands could be caused by the transformation to amorphous AB* and, more specifically, the early change in B-N stretching modes may be caused by B-N bond reordering necessary for the formation of DADB. *In situ* NMR and XRD data by Shaw et al. [29] show the existence of the mobile new phase AB*, essential for hydrogen release, which is a solid with rapidly moving AB molecules. That work suggests that the electron density at the N and B atoms in such a new phase would be more similar to that of an isolated AB molecule than that of its molecular crystal counterpart. Such a phase would involve a relaxation of the extensive dihydrogen bonding structure, thus allowing easy B-N axis rotation and this phenomenon may be the cause for such early shifts in B-N stretching modes represented in Figure 3.20. In the time ranges indicated before for each AB sample, some of the sudden Raman changes have been identified as the shift from DADB bands to PAB bands, simultaneously to the maximum H₂

release. After the maximum in H₂ MS profile is reached, the remaining Raman bands suggest a mixture of polymeric and cyclic poliaminoborane.

Regarding the AB supported materials, considerable differences can be seen. On the structure point of view; XRD patterns for AB/Ga₂O₃ 0.5:1 (Met) only shows the diffraction peaks corresponding to the porous support which suggests that AB particles are too small to generate diffraction probably because they are confined inside the narrow Ga₂O₃ pores. On the other hand, Ga₂O₃ peaks can be seen combined to that of NH₃BH₃ in the pattern corresponding to AB/Ga₂O₃ 0.5:1 (THF). This may be caused by some AB particles being loaded onto the Ga₂O₃ surface. In the case of AB/Ga₂O₃ 1:1 (THF), Ga₂O₃ diffraction peaks aren't observed anymore probably because the support surface is covered by AB particles. This fact is also consistent with N₂ adsorption/desorption results as total N₂ adsorbed volume and BET area decrease are nearly the same for both AB/Ga₂O₃ (THF) materials, showing little difference regarding pores filling is caused by increasing the loading ratio from 0.5:1 to 1:1. The excessive Ga₂O₃ surface coverage is also observable in Raman-MS results as previously mentioned. Little effect can be attributed to confinement onto Ga₂O₃ on the decomposition behavior for 1:1 mass ratio as AB/Ga₂O₃ 1:1 (THF) as this sample shows the same H₂ MS profile during decomposition than neat AB with a lower threshold temperature that may be due to some AB being actually confined in Ga₂O₃ porosity. In contrast, both 0.5:1 mass ratio samples exhibit a one-step decomposition mechanism with AB/Ga₂O₃ 0.5:1 (Met) showing a tremendous destabilization effect in accordance with the XRD results which seem to indicate the presence of very small AB aggregates that may release H₂ more readily than larger AB particles on the surface or the neat compound. There is then a considerable destabilization effect on AB by impregnation onto Ga₂O₃ if the suitable level of AB loading is applied. Optimal AB impregnation mass ratio on Ga₂O₃ seems to be under 1:1 as already reported elsewhere for other porous supports [33,34].

It is also worth mentioning that NH₃ desorption concomitant to H₂ release during dehydrogenation is detectable during thermal decomposition of AB/ Ga₂O₃ samples regardless of the mass ratio or the employed solvent while the formation of B₂H₆ and N₃N₃H₆ seem to be hindered. This facts suggest an interaction between Ga₂O₃ surface and AB particles. Such NH₃ desorption appears much more diluted in the case of AB/Ga₂O₃ 1:1 (THF) because the volume of desorbed H₂ is much bigger in this case.

5. Conclusions

Thermolysis of Ammonia Borane (AB) has been investigated by means of DSC, TDS and *operando* Raman-MS experiments. Small differences regarding H₂ yield are observed between

neat AB and recrystallized AB while some changes in the thermal behavior for AB-Met suggest AB particles suffer some surface transformation. The melting temperature seems to be a key parameter for understanding AB thermal decomposition under 100 °C as AB dehydrogenation seems to be favored in the molten phase in general.

Structural changes appear much quicker in the case of AB-THF, which melting event proved to be a smaller barrier at 90 °C while they take a little longer for AB-Met and much longer for neat AB. The three materials present the same unique H₂ desorption event at 90 °C and the *operando* Raman-MS results corroborate a nucleation and growth mechanism for AB decomposition samples.

For Ga₂O₃-supported AB materials, there is a considerable enhancement in H₂ desorption properties in terms of lowered temperature and kinetics for the 0.5:1 AB/Ga₂O₃ samples in which decomposition proceeds through a one-step mechanism. Dehydrogenation temperature is specially lowered in the case of AB/Ga₂O₃ 0.5:1 (Met). All the AB/Ga₂O₃ materials induce NH₃ desorption simultaneously to dehydrogenation during thermal decomposition which may be caused by interactions between the support surface and AB molecules.

References

- [1] Wolf G.; Baumann J.; Baitalow F.; Hoffmann F.P., *Thermochim. Acta* **343** (2000) 19-25
- [2] Baitalow F.; Baumann J.; Wolf G.; Jaenicke-Rößler K.; Leitner G., *Thermochim. Acta* **391** (2002) 159–168
- [3] Baumann J.; Baitalow F.; Wolf G., *Thermochim. Acta* **430** (2005) 9–14
- [4] Baitalow F.; Wolf G.; Grolier J.-P. E.; Dan F.; Randzio S.L., *Thermochim. Acta* **445** (2006) 121–125
- [5] Gutowska A.; Li L.; Shin Y.; Wang C.M.; Li X.S.; Linehan J.C.; Smith R.S.; Kay B.D.; Schmid B.; Shaw W.; Gutowski M.; Autrey T., *Angew. Chem. Int. Ed.* **44** (2005) 3578 –3582
- [6] Raissi A.T. Proceedings of the 2002 U.S. DOE Hydrogen Program Review NREL/CP-610-32405
- [7] Kim H.; Karkamkar A.; Autrey T.; Chupas P.; Proffen T., *J. Am. Chem. Soc.* **131** (2009) 13749–13755
- [8] Deshmane C.A.; Jasinski J.B.; Carreon M.A., *Eur. J. Inorg. Chem.* **2009**, 3275–3281
- [9] Sing K.S.W.; Everett D.H.; Haul R.A.W.; Moscou L.; Pierotti R.A.; Rouquerol J.; Siemieniowska *Pure & Appl. Chem.* **57** n°4 (1985) 603-619
- [10] Brunauer S.; Emmett P.H.; Teller E., *J. Am. Chem. Soc.* **60** (1938) 309-319
- [11] Barrett E.P.; Joyner L.G.; Halenda P.P., *J. Am. Chem. Soc.* **73** (1951) 373-380
- [12] Azaroff L. V.; *Mac Graw Hill*, Tokyo 1968 p.549
- [13] Hess N.J.; Bowden M.E.; Parvanov V.M.; Mundy C.; Kathmann S.M.; Schenter G.K.; Autrey T., *J. Chem. Phys.* **128** (2008) 034508 1-11
- [14] Karkamkar A.; Aardahl C.; Autrey t., Material Matters Volume 2 Article 2, SIGMA ALDRICH (2007) - See more at: <http://www.sigmaaldrich.com/technical-documents/articles/material-matters/recent-developments.html#sthash.cVfyUPAf.dpuf>

Código de campo cambiado

- [15] Kissinger H.E.; *J. Research Natl Bur. Standards* **57** (1956) 217-221
- [16] Kissinger H.E.; *Anal. Chem.* **29** (1957) 1702-1706
- [17] Gangal A.C.; Sharma P.; *Int. J. Chem. Kinet.* **45** (2013) 452-461
- [18] Al-Kukhun A.; Hwang H.T.; Varma A.; *Int. J. Hydrog. Energy* **38** (2013) 169-179
- [19] Sepehri S.; Garcia B.B.; Cao G.; *J. Mater. Chem.* **18** (2008) 4034-4037
- [20] Kang X.; Fang Z.; Kong L.; Cheng H.; Yao X.; Lu G.; Wang P.; *Adv. Mater.* **20** (2008) 2756-2759
- [21] Si X.L.; Sun L.X.; Xu F.; Jiao C.L.; Li F.; Liu S.-S.; Zhang J.; Song L.F.; Jiang C.H.; Wang S.; Liu Y.L.; Sawada Y.; *Int. J. Hydrog. Energy* **36** (2011) 6698-6704
- [22] Stowe A.C.; Shaw W.J.; Linehan J.C.; Schmid B.; Autrey T.; *Phys. Chem. Chem. Phys.* **9** (2007) 1831-1836
- [23] Custelcean R.; Dreger Z.A.; *J. Phys. Chem. B* **107** (2003) 9231-9235
- [24] Allis D.G.; Kosmowski M.E.; Hudson B.S.; *J. Am. Chem. Soc.* **126** (2004) 7756-7757
- [25] Frueh S.; Kellett R.; Mallery C.; Molter T.; Willis W.S.; King'onde C.; Suib S.L.; *Inorg. Chem.* **50** (2011) 783-792
- [26] Chellappa R.S.; Autrey T.; Somayazulu M.; Struzhkin V.V.; Hemley R.J.; *Chem. Phys. Chem.* **11** (2010) 93-96
- [27] Bøddeker K.W.; Shore S.G.; Bunting R.K.; *J. Am. Chem. Soc.* **88** (1966) 4396-4401
- [28] Weismiller M.R.; Wang S.Q.; Chowdhury A.; Thynell S.T.; Yetter R.A. *Thermochim. Acta* **551** (2013) 110-117
- [29] Shaw W.J.; Bowden M.; Karkamkar A.; Howard C.J.; Heldebrant D.J.; Hess N.J.; Linehan J.C.; Autrey T.; *Energy Environ. Sci.* **3** (2010) 796-804
- [30] Hess N.J.; Schenter G.K.; Hartman M.R.; Daemen L.L.; Proffen T.; Kathmann S.M.; Mundy C.J.; Hartl M.; Heldebrant D.J.; Stowe A.C.; Autrey T.; *J. Phys. Chem. A* **113** (2009) 5723-5735
- [31] Stowe A.C.; Shaw W.C.; Linehan J.C.; Schmid B.; Autrey T.; *Phys. Chem. Chem. Phys.* **9** (2007) 1831-1836
- [32] Bowden M.; Autrey T.; Brown I.; Ryan M.; *Current Applied Physics* **8** (2008) 498-500
- [33] Kim H.; Karkamkar A.; Autrey T.; Chupas P.; Proffen T.; *J. Am. Chem. Soc.* **131** (2009) 13749-13755
- [34] Stowe A. C.; Schmid B.; Karkamkar A.; Shaw W.; Linehan J. C.; Li L.; Autrey T. *Prepr. Pap.-Am. Chem. Soc., Div. Fuel Chem.* (2006) **5**, 584

Chapter 4

Ammonia Borane recrystallization and confinement: support effect

Summary

Ammonia borane is a promising hydrogen storage material, but its application is hurdled by the slow hydrogen release kinetics among other factors. Nanoconfinement of ammonia borane in scaffolding porous materials improves the hydrogen release kinetics and lowers the decomposition temperature as shown in Chapter 3 but the mechanisms through which nanoconfinement promotes these effects are still unclear. In this chapter, hydrogen thermal desorption from ammonia borane impregnated into various mesoporous carriers has been investigated by means of *operando* Raman - Mass Spectrometry methodology. In order to evaluate the influence of the properties of the host on AB nanoconfinement, four different scaffolds with different chemical composition and textural properties (pore diameter and volume) have been studied after loading of 1:1 AB/scaffold mass ratio: Cobalt-substituted $\text{AlPO}_4\text{-5}$ having intercrystalline mesoporosity, a mesoporous gallium oxide and two SBA-15 type materials. Results indicate the presence of crystalline ammonia borane in all impregnated hosts. By thermolysis, all nanoconfined samples begin to evolve hydrogen at a lower temperature than neat ammonia borane, although this effect is much more pronounced on SBA-15 samples. Furthermore, Raman spectra indicate a modification in the mechanism of decomposition in ammonia borane-loaded SBA-15 materials that suggests a combined effect of nanoconfinement and chemical interaction between hydride and host.

4.1. Introduction

As already introduced in chapter 3, a very interesting approach in this sense consists in confining NH_3BH_3 into mesoporous scaffolds [1,2]. This strategy has demonstrated the reduction of activation barriers for hydrogen release upon confinement, speeding up the dehydrogenation reaction and the formation of borazine is dramatically reduced [8]. Furthermore, the exothermicity of the hydrogen desorption reactions is significantly lowered ($\Delta R_H \approx -1$ kJ/mol H_2), due to the modification of structural and thermodynamic properties of AB [1,3].

In this chapter, the role of nanoconfinement of ammonia borane on different porous host materials has been studied employing the *operando* Raman-MS methodology already described in section 2.2.12. This technique allows to simultaneously evaluating differences in structural/compositional changes of AB as well as on its hydrogen desorption properties due to its dispersion and destabilization by nanoconfinement. Four different host materials have been tested to this aim: two different SBA-15 materials, which were the first type of reported materials for hosting of AB [1,2], mesoporous Ga_2O_3 material for comparison purpose as its use has already been studied in chapter 3, and mesopores-containing CoAPO-5 microporous materials [4]. These four materials have been selected in order to analyze the influence of the textural properties of the host on AB nanoconfinement employing a 1:1 mass ratio loading of AB on the support which was shown to be excessive for porous Ga_2O_3 . SBA-15 materials are characterized by high pore volumes and an ordered mesopore structure, while the mesoporous Ga_2O_3 presents lower pore volume with a disordered pore structure. A CoAPO-5 microporous material was also studied, which possesses hierarchical porosity with two kinds of pores conceptually different to the previous ones: (i) the micropores that would extremely confine amino borane, and (ii) a scarcely ordered intercrystalline mesoporosity. Such structure allows to evaluate the possible effect of a much more confined space with presumed diffusion problems. Additionally, experiments with Ga_2O_3 and CoAPO-5 can shed light on the influence of chemical composition of the support (as compared to SBA-15) and its possible catalytic effect, and to the best of authors' knowledge these materials have not been tested before as hosts for nanoconfined AB.

4.2 Experimental

4.2.1 Synthesis of supports

Co-substituted microporous material $\text{AlPO}_4\text{-5}$, CoAPO-5, containing intercrystalline mesoporosity was synthesized by direct incorporation of Co into the AlPO_4 framework resulting in an isomorphous substitution of Al ions by Co^{2+} , as described elsewhere [4]. First, cobalt acetate was dissolved in a phosphoric acid aqueous solution under stirring to form a pink solution. Then, a

suitable amount of $\text{Al}(\text{OH})_3$ was slowly added to the mixture. Finally, the amine MCHA, used as a structure directing agent, was added to the gel and the mixture was stirred for an hour at room temperature. The resulting pink mixture was sealed into a Teflon-lined stainless steel autoclave and statically heated at 180 °C for 18 h. The resulting gel composition was: 0.09 Co : 0.65 Al : 1.0 P : 1.36 MCHA : 3,73 H_2O (mass ratio). The recovered blue solid was filtered, washed with abundant deionized water and dried at room temperature. Before using as host of NH_3BH_3 , CoAPO-5 was calcined at 550 °C (heating rate 3 °C·min⁻¹) for 1 h under N_2 flow and subsequently for 5 h under air flow.

SBA-15 was synthesized using Pluronic PE-10400 as structure directing agent, instead of the more frequently used P123, and with HCl (1.6 M) to provide the adequate acid medium. Tetramethylorthosilicate (TMOS) was used as the silica source. This porous material is denoted in this study as SBA-15-L [5,6]. The mass ratio of the reagent solution was: 1 PE-10400: 23.44 H_2O : 15.62 HCl: 1.52 TMOS. PE-10400 was dissolved at room temperature in 1.6 M aqueous HCl solution, in a closed Teflon container, under magnetic stirring at 55 °C. Then, TMOS was added and the solution was stirred for 24 h. The container was then transferred to an oven and aged at 80 °C for 24 h under static conditions. The obtained solution was filtered over a Whatman-541 filter paper, and the precipitate was washed with ethanol and air-dried at room temperature. Finally, the surfactant template was removed by calcination at 550 °C for 5 h.

Another pure silica SBA-15 was synthesized by using Pluronic P123 triblock copolymer, according to methods described by Zhao and coworkers [7], being labeled as SBA-15-Z in this work. 4 g of Pluronic P123 were dissolved at room temperature in 125 mL of 1.9 M HCl in aqueous solution. TEOS was then added to the solution and the resulting mixture was vigorously stirred at 40 °C for 20 h. The mass ratio of the reagent solution was: 1 P123: 28.50 H_2O : 2.16 HCl: 2.156 TEOS. Aging was then performed at 100 °C under static conditions for 24 h in a closed Teflon container. The solid product was recovered by filtration and the template was removed by calcination in air at 550 °C for 5 h. The porous materials described above were made in the Group of Molecular Sieves at Instituto de Catálisis y Petroleoquímica (CSIC, Madrid).

Crystalline mesoporous gallium oxide was synthesized as previously described in section 3.3.2 and reported elsewhere [8] by the group of prof. Moisés Carreón, at the University of Kentucky (Louisville, USA).

4.2.2 AB impregnation on the supports

Chapter 3 illustrates that THF proves to be more appropriate than methanol as a solvent for AB impregnation on porous support; this is mainly because the latter slightly alters the thermal

decomposition properties of AB. Therefore, THF was used to dissolve AB prior to impregnate the porous supports as described next and in section 3.2.3 by incipient wetness impregnation. The supports were previously dehydrated at 120 °C for 2 h.

200 mg of NH_3BH_3 were dissolved in 4 mL of THF. The solution was stepwise added to 200 mg of the calcined support every 30 minutes in order to facilitate filling the porous channels by capillary action. After each addition, the solid was dried under vacuum for one hour and a new solution portion was added. After the last solution addition, the samples were dried under vacuum overnight. The samples then offered a 1:1 AB loading and were called AB-Co, AB-L, AB-Z and AB-Ga respectively.

4.2.3 Characterization techniques

All the techniques and equipments used to characterize the samples are described in detail in section 2.2.

Structural analysis of the samples was performed by X-ray diffraction. XRD for both neat and impregnated NH_3BH_3 samples and for Ga_2O_3 and CoAPO-5 supports before and after impregnation. The 2θ range was of 0.4° - 6.0° (low angle) for SBA-15 supports either before or after impregnation.

Textural properties of the studied porous supports were determined by transmission electron micrographs (TEM) and scanning electron microscopy (SEM). To get further understanding on textural properties of the porous materials, Nitrogen adsorption-desorption isotherms were measured at -196 °C in a Micromeritics ASAP 2420 device. The specific surface area, S_{BET} , was once more estimated from nitrogen adsorption data in the relative pressure range from 0.04 to 0.2 using the Brunnauer-Emmett-Teller (BET) method [9,10] while pore size distributions were obtained from the adsorption branches of the isotherms using the Barrett-Joyner-Halenda (BJH) model with cylindrical geometry of the pores [11]. Calcined silicas, CoAPO-5 and Ga_2O_3 were pretreated at 350 °C for at least 16 h under high vacuum, and impregnated silica-samples were pretreated at room temperature for 16 h with a final pressure of 7 μm of Hg.

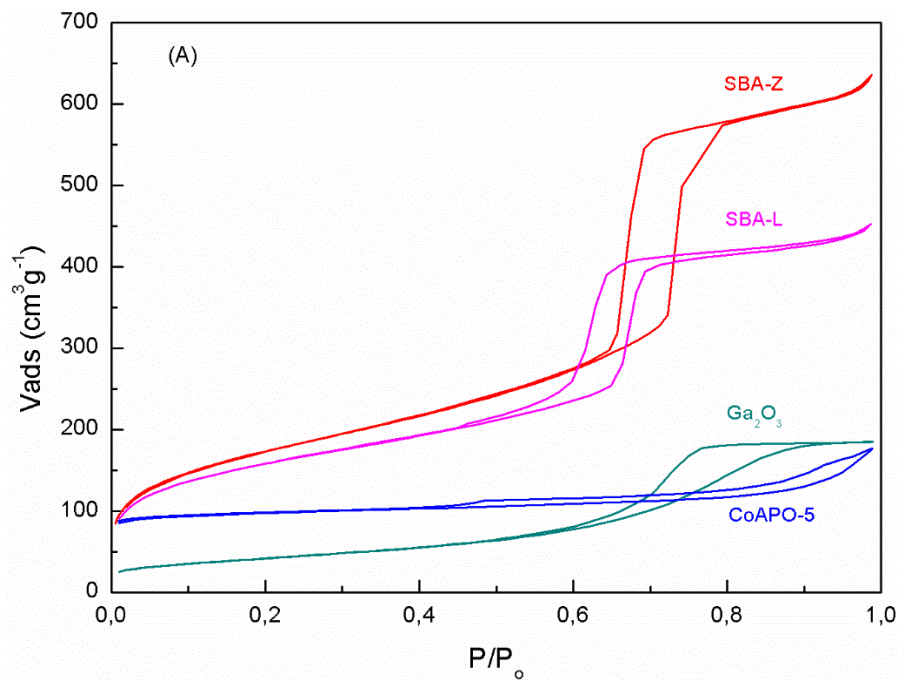
Operando Raman-MS was once more used to get information on molecular changes in neat AB and AB-impregnated supports, during thermal decomposition while simultaneously registering H_2 and other volatiles impurities release. The system was linearly heated at $1^\circ\text{C}\cdot\text{min}^{-1}$ up to 200 °C under $50\text{ mL}\cdot\text{min}^{-1}$ of 99.9995 % N_2 during *operando* Raman-MS analyses; Raman spectra were acquired every 600 seconds (acquisition of 30 accumulations of 10 seconds with a pause of 300 seconds between consecutive acquisitions) or every 60 seconds in the case of neat and Ga_2O_3 impregnated AB samples (6 accumulations of 10 seconds with no pause).

4.3 Results

4.3.1 Characterization of empty and ammonia borane-loaded supports

4.3.1.1 Textural properties

Figure 4.1.A shows the nitrogen adsorption/desorption isotherm curves at $-196\text{ }^{\circ}\text{C}$, along with the pore size distribution of CoAPO-5, SBA-15-L, SBA-15-Z and Ga_2O_3 (Figure 4.1.B). The isotherms of the four supports are of *type IV*, according to IUPAC classification [9], which confirms their mesoporous structure. These isotherms illustrate clear hysteresis loops in the region with p/p_0 higher than 0.15 which is typical of mesoporous materials, but displaying very different characteristics depending on the material. At the same time, the presence of microporosity cannot be discarded in SBA-15 and is evident in the CoAPO-5 microporous material, whose isotherm is a mixture between *types I* and *IV*. Table 4.1 reports the values extracted from the isotherms. Both SBA-15 silicates present BET areas three times higher than that of Ga_2O_3 and twice as high as that of CoAPO-5, whose surface area and pore volume are mainly due to its micropores. Pores volume follows a similar trend, those of Ga_2O_3 and CoAPO-5 being quite similar. Therefore, these later materials possess smaller porosity than the silica-based ones, which also show higher pore size diameters.



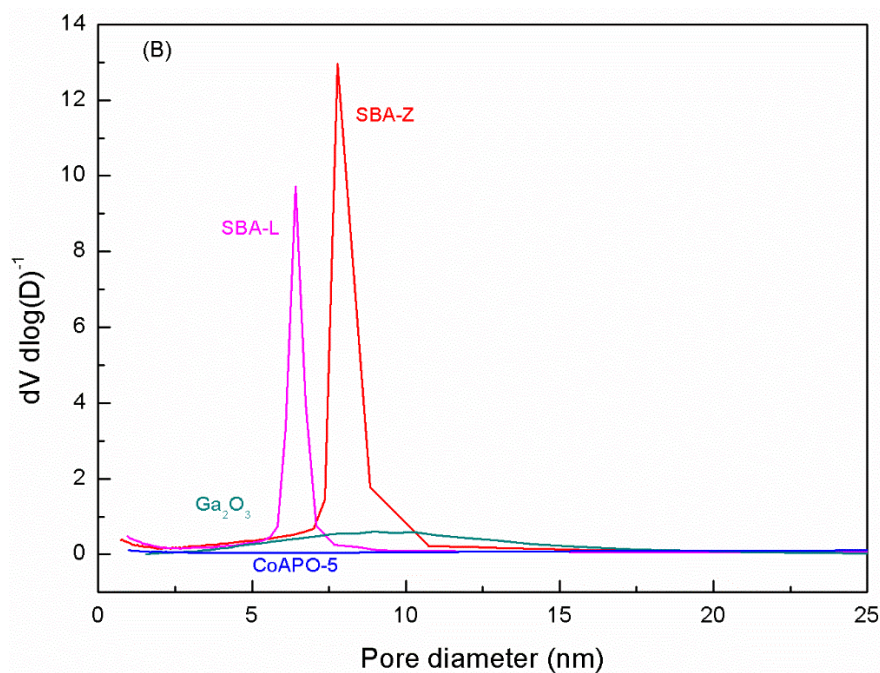


Figure 4.1: N₂ adsorption/desorption isotherms at -196 °C (A) and pore size distribution (B) for SBA-15-Z, SBA-15-L, mesoporous Ga₂O₃, and CoAPO-5

Table 4.1: Textural properties of empty and ammonia borane-loaded supports

Support/simple	S_{BET} (m ² g ⁻¹)	V_p (cm ³ g ⁻¹)	$D_{p\ BJH}$ (nm)
Ga ₂ O ₃	150	0.29	9.0
AB-Ga	29	0.07	8.9
CoAPO-5	300	0.26	34.4
AB-Co	50	0.03	4.4
SBA-15-Z	609	0.96	7.8
AB-Z	135	0.26	6.0
SBA-15-L	550	0.69	6.4
AB-L	34	0.07	4.9

Table 4.1, and Figure 4.1.A illustrate that the N₂ adsorption-desorption isotherm for mesoporous Ga₂O₃ presents an adsorption curve rising at relative pressures below 0.4 as already described in section 3.3.2; its hysteresis loop ranges from 0.5 to 0.9 relative pressures, which corresponds to a broad pore size distribution and, in accordance, BJH pore size diagram of this material exhibits a broad distribution with a maximum near 9.0 nm. The BET specific surface area observed for this mesoporous Ga₂O₃ phase was of ~150 m²·g⁻¹.

N₂ isotherm of CoAPO-5 sample shows an even broader pore size distribution, with a hysteresis loop in the 0.45 to 0.99 relative pressures range. This material displays a broad variety of wide mesopores and typical microporosity of a crystalline CoAPO-5. BJH pore size distribution curve

exhibits a broad mesopore distribution with a maximum near 40 nm. In addition to the intercrystalline mesoporosity found in CoAPO-5 [4] its microporous character is made clear by the substantial N₂ adsorption below relative pressures of 0.1.

In contrast, SBA-15-L and SBA-15-Z isotherms reveal a narrow pore size distribution with a similar slope for the adsorption curve and a hysteresis loop located between relative pressures of 0.6 and 0.8 (Figure 4.1.A), resulting in narrow unimodal pore size distributions (Figure 4.1.B). Comparing the results obtained with the two supports, SBA-15-L shows smaller pore sizes than SBA-15-Z as well as lower BET area and pore volume (Table 4.1).

Figure 4.2 shows the isotherms of the AB-impregnated SBA-15, Ga₂O₃ and CoA-PO5 materials, also exhibiting the hysteresis loop characteristic of type IV isotherms. However, the textural properties are significantly reduced (Table 4.1). The isotherm for AB-Ga shows that no adsorption takes place up to a relative pressure range between 0.55 and 0.9, at slightly higher values than for the host material. The drop in the BET area and the pore volume caused by impregnation of the supports with AB (Table 4.1) suggest that host pores were filled or blocked by AB aggregates. The maximum of the BJH pore size distribution falls in the same value as for the neat support (9.0 nm) suggesting the structure of the material is preserved through AB impregnation.

The CoAPO-5 AB impregnated isotherm shows the corresponding support pore distribution even broadens as the hysteresis loop spreads throughout the whole relative pressure range. This is in accordance with the undefined pore size distribution plot for AB-Co in Figure 4.2.B and may indicate that CoAPO-5 structure collapse after AB impregnation. BET area and pore volume also fall considerable with respect to the corresponding support.

In the case of SBA-15 materials, substantial changes can be observed in the textural properties after loading with ammonia borane. For SBA-15-L (sample AB-L), a drastic reduction of BET area from 550 to 34 m²·g⁻¹ is observed, and the pore volume decreases from 0.69 to 0.07 cm³·g⁻¹. AB-L isotherm displays a broad hysteresis loop ranging from 0.4 to 0.95 relative pressures. Therefore, the SBA-15-L material has undergone considerable changes upon AB impregnation, as can be deduced from the relatively broad pore size distribution corresponding to the pores that remain void after AB impregnation with a maximum at 4.9 nm, a significantly lower value compared to the mean pore diameter of 6.4 nm observed in the empty support. Equivalent variations in textural properties of SBA-15-Z due to loading with ammonia borane are observed, with an important drop of surface area (from 609 to 135 m²·g⁻¹), of pore diameter (from 7.8 to 6.0 nm) and of pore volume (from 0.96 to 0.26 cm³·g⁻¹). On the other hand, the AB-Z hysteresis loop ranges from 0.45 to 0.8 relative pressures, rather close to those of the unloaded support. This result is consistent with the higher pore volume of the empty SBA-15-Z matrix that indicates a

higher capacity for confining compound without significant pore blockage. A similar reduction of BET area was reported elsewhere for mesoporous SBA-15 with a loading of 1 g of AB : 1 g of host [1].

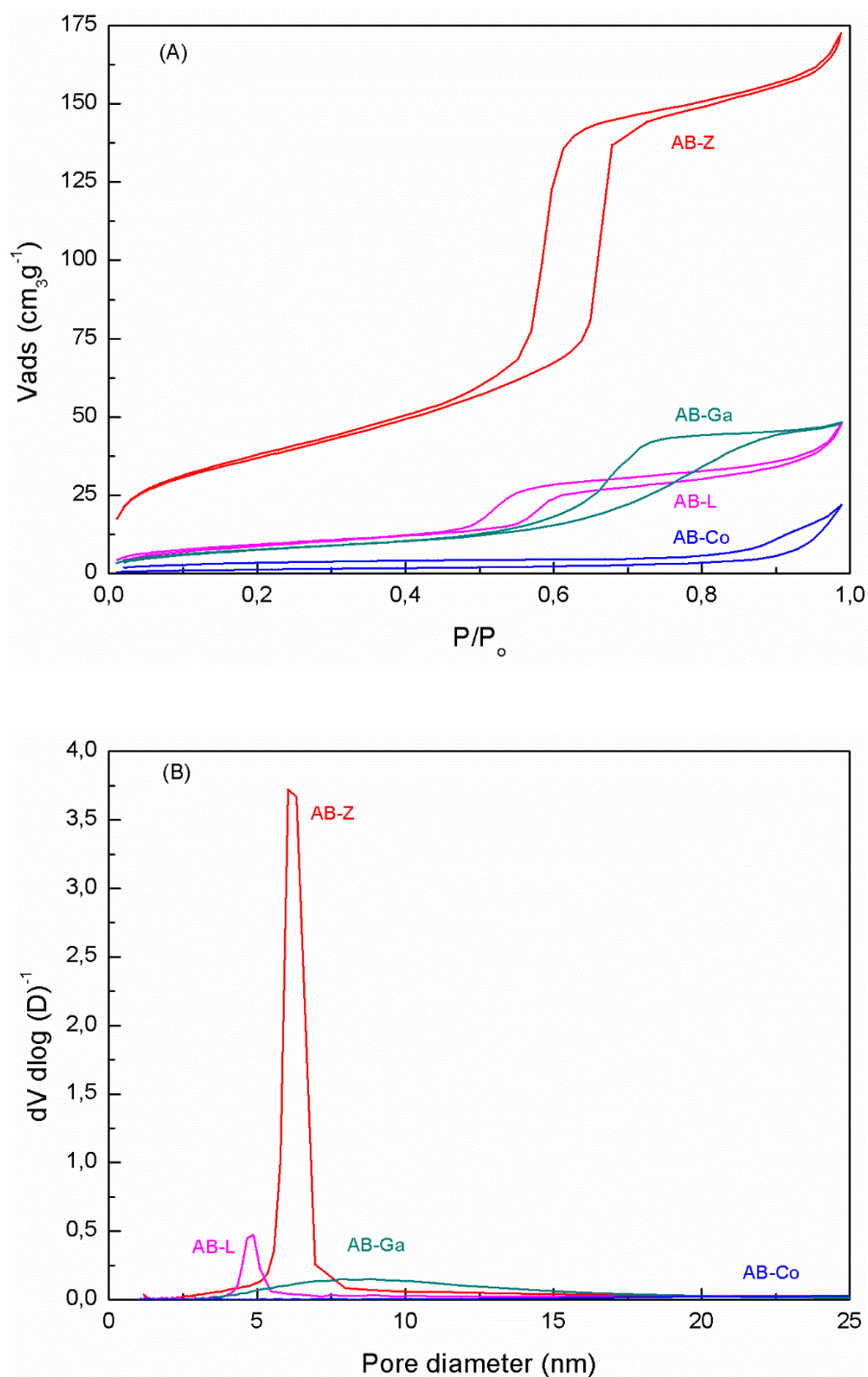


Figure 4.2: N₂ adsorption/desorption isotherms at -196 °C (A) and pore size distribution (B) for AB-Z, AB-L, AB-Ga and AB-Co

4.3.1.2 Morphology

Figure 4.3 shows HR-TEM images of the four porous materials. In the case of mesoporous gallium oxide, the HR-TEM image (Figure 4.3.A) shows several nanocrystals present on the surface of the material. Lattice fringes are clearly visible confirming the crystallinity of the material. The insert shows a Selected Area Electron Diffraction (SAED) pattern with diffraction rings corresponding to spinel cubic Ga_2O_3 . Other areas show “wormhole” type structures typical of mesoporous transition metal oxides (Figure 4.3.B).

Figure 4.3.C shows two different kinds of particle morphologies observed in CoAPO-5 samples. A crystal with dimensions of approximately $200 \times 350 \text{ nm}^2$ can be observed, together with some non-crystalline agglomerates surrounding the crystal. At higher magnifications, parallel pores can be seen within the crystal (Figure 4.3.D).

TEM images of SBA-15 materials reveal highly-pore ordered structured materials. Figure 4.3.E, with lower magnification, shows mesoscopic structure of SBA-15-Z. TEM pictures show lengthwise distribution of long, unidirectional channels of the mesostructure that are highly ordered. The projection along perpendicular direction to channels axis also exhibits a compact hexagonal array of pores, which looks similar to a honeycomb, in agreement with the morphology of this material [7]. Figure 4.3.E displays a particle with hexagonal array with pore diameter below 10 nm, which is consistent with those obtained by textural analyses. Figure 4.3.G, at higher magnification, illustrates a big particle of SBA-15-L containing different domains with clearly distinguishable channels orientation while Figure 4.3.H shows some pores oriented in a direction parallel to that of the impinging beam. These pores display a hexagonal array and a very clear circular shape, typical of SBA-15 type materials [12]. From this image, the pore diameter of SBA-15-L can be estimated by image analysis giving a value of approximately 7 nm, which is consistent with those obtained by textural analyses.

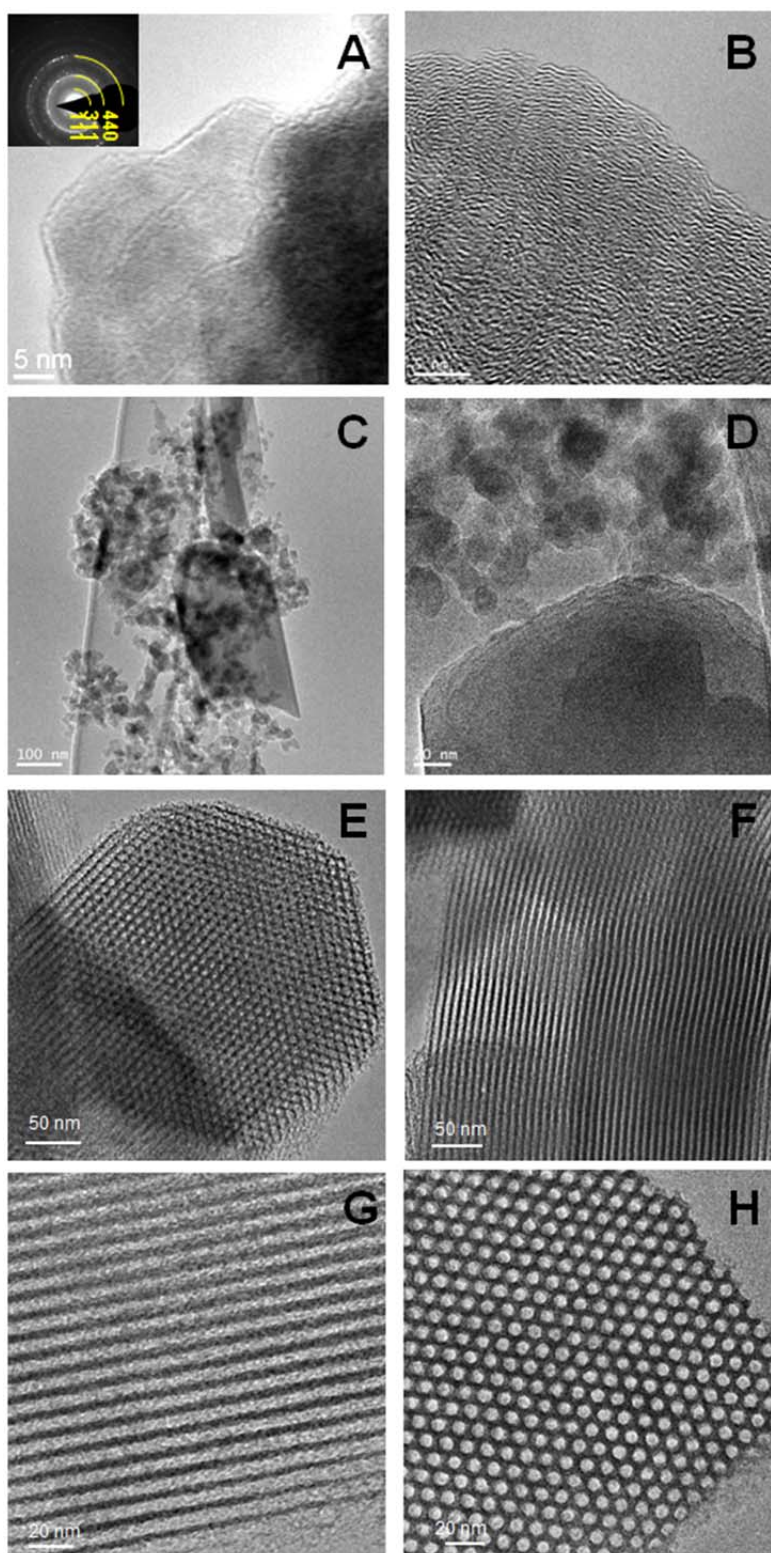


Figure 4.3: (A, B) TEM images of Ga_2O_3 , (C, D) TEM images of CoAPO-5, (E, F) TEM images of SBA-15-Z and (G, H) TEM images of SBA-15-L. Inset in Figure 4.3(A) shows a Selected Area Electron Diffraction (SAED) pattern

To complement the information provided by TEM micrographs, Figure 4.4 shows SEM micrographs of the supports. As can be seen, the structure of SBA-15-Z is fiber-like or elongated rod, formed by aggregates of rods connected into ropelike macrostructures. The average particle

size is 0.75-1 μm in length and about 2 μm in width. SBA-15-L particles exhibit hexagonal dish-shaped morphology or short rod. The average particle size is 5 μm in diameter and 0.2 μm width. In contrast, Ga_2O_3 is constituted by highly aggregated spherical particles, each of them mesoporous as presented in Figure 4.4.B, but also showing a high interparticle macroporosity. Finally, CoAPO-5 shows a hollow-balloon particle morphology, composed by aggregated crystals with certain mesoporosity among them.

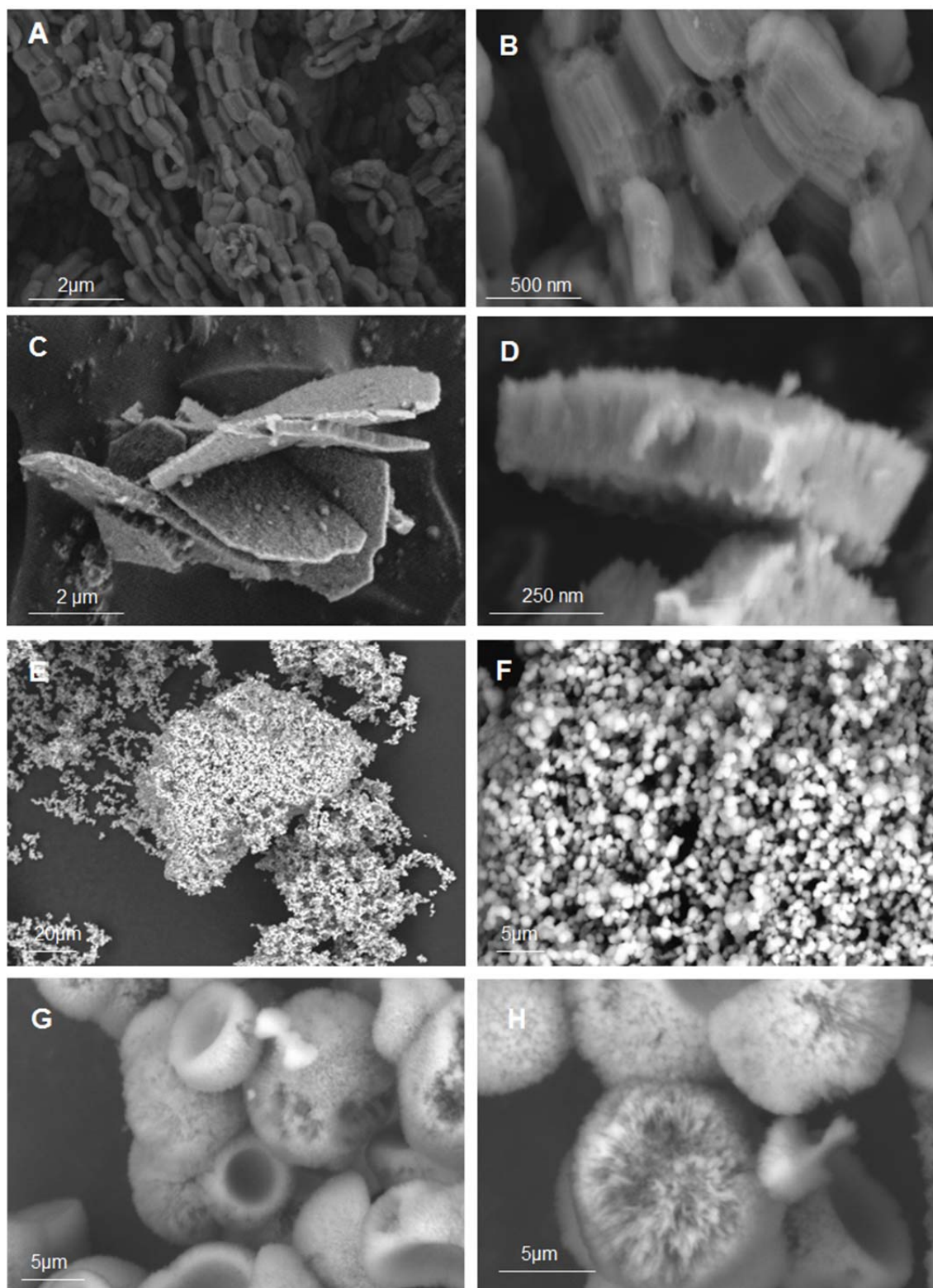


Figure 4.4: (A,B) SEM images of SBA-15-Z (C,D) SEM images of SBA-15-L (E,F) SEM images of mesoporous Ga₂O₃ (G,H) SEM images of CoAPO-5

4.3.1.3 Structural characterization

Neat AB, AB-Co, AB-L, AB-Z and AB-Ga, as well as the empty supports were characterized by X-ray diffraction (Figures 4.5A and 4.5B). Figure 4.5.A shows the diffraction pattern of neat AB with peaks at $2\theta = 23.88^\circ$ and $2\theta = 24.38^\circ$, typical of the tetragonal crystalline structure of this compound (JCPDS 74-894). X-ray diffraction patterns of all impregnated porous supports also show these characteristic peaks, which are indicative of the presence of crystalline AB particles outside the pores of the hosts [13]. Nevertheless, in the diffraction patterns of impregnated porous supports, these peaks are broadened and partially merged. This indicates a certain inhomogeneity in the properties of crystals and a reduction of crystallite size, which may be due to the coexistence of nanoconfined AB with crystalline particles outside the pores of the host.

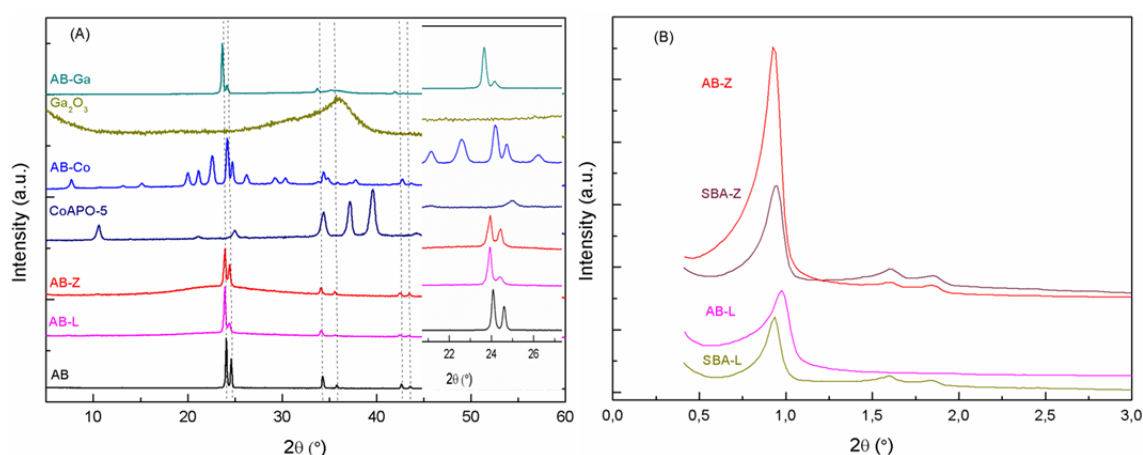


Figure 4.5: (A) X-ray Diffraction patterns of AB-Z, AB-L, neat AB, CoAPO-5, AB-Co, mesoporous Ga_2O_3 and AB-Ga (B) Low angle X-ray diffraction patterns of SBA-15-L, SBA-15-Z, AB-L and AB-Z. Vertical dashed lines indicate the position of characteristic AB peaks

Additional information can be obtained by analyzing each pattern in more detail. The XRD pattern of the mesoporous gallium oxide (Ga_2O_3) (Figure 4.5.A), already described in section 3.3.2, is formed by two broad peaks at 2θ below 40° and above 60° (easier to appreciate in Figure 3.4) corresponding to the (311) and (440) planes of spinel-type cubic Ga_2O_3 respectively [8]. The absence of other secondary XRD reflections typical of spinel structure may suggest that the mesostructure is not fully crystalline (which is supported by the Selected Area Electron Diffraction inset of Figure 4.5.A). AB-Ga exhibits the typical peaks of NH_3BH_3 . As previously described, the peaks of ammonia borane at $2\theta = 23.88^\circ$ and 24.38° are attenuated and partially merged, which may indicate a reduction of crystallinity by incorporation of ammonia borane inside the porous structure of the host material even if most of AB seems to be accumulated on Ga_2O_3 surface under aggregates as reported in chapter 3 [14].

CoAPO-5 exhibits the typical diffraction pattern of well-defined CoAPO-5 phase [4]; AB-Co sample pattern shows a combination of those of CoAPO-5 and NH_3BH_3 . While the peaks of AB remained unaltered and without any attenuation or displacement, those corresponding to the support appear shifted to higher angles, which suggest a deformation of the lattice structure of the CoAPO-5 support that may be due to the filling of its pores with a small fraction of AB.

In the case of silica supports, the NH_3BH_3 diffraction pattern remains apparent in AB-L and AB-Z, but with a certain attenuation and displaced to a lower diffraction angle of the band at $2\theta = 24.38^\circ$. This variation is more significant in the case of the AB-L sample than in the AB-Z sample. To further analyze possible structural variations in the silica supports, Figure 4.5.B shows the low angle diffraction patterns of SBA-15-L [5,12], used as the support for AB-L sample, and that of the impregnated sample. The most intense diffraction peak, corresponding to the 100 plane of a hexagonal structure at $2\theta = 0.93^\circ$, shifts in the pattern of the impregnated sample to slightly higher angles, appearing at $2\theta = 0.97^\circ$. Moreover, the less intense peaks of SBA-15-L pattern at $2\theta = 1.60^\circ$ and $2\theta = 1.84^\circ$ that correspond to 110 and 200 diffraction planes, respectively, disappear in the AB-L pattern. The weaker intensity in the low-angle diffraction patterns of SBA-15-L upon AB impregnation, suggests an effective filling of the pores structure by AB since the hexagonal array remains in the impregnated sample with two-dimensional $p6mm$ symmetry. In contrast, in the low-angle diffraction patterns of AB-Z the three reflection peaks, which are characteristic of SBA-15, are clearly detected and show no appreciable shift after NH_3BH_3 impregnation. This result agrees with the smaller modification of textural properties of SBA-15-Z upon loading with ammonia borane, detected in section 4.3.1.1.

4.3.1.4 Raman characterization of neat and supported ammonia borane

Figure 4.6 shows Raman spectra of neat and supported ammonia borane. As already detailed in section 3.3.2., neat NH_3BH_3 spectrum displays five vibrational zones: (i) N-H stretching region between 3150 cm^{-1} and 3350 cm^{-1} (not shown in Figure 4.6 due to excessive noise in the registered signal for AB-Ga); (ii) B-H stretching region between 2250 cm^{-1} and 2400 cm^{-1} ; (iii) N-H deformation modes between 1350 cm^{-1} and 1600 cm^{-1} ; (iv) B-H deformation modes around 1180 cm^{-1} ; and (v) B-N stretching modes close to 800 cm^{-1} [17]. The Raman band at 3313 cm^{-1} corresponds to asymmetric stretching N-H mode while the most intense bands at 3251 cm^{-1} and at 3175 cm^{-1} are characteristic of symmetric N-H stretching modes [15]. Asymmetric stretching B-H modes show an intense band at 2377 cm^{-1} and the stretch at 2281 and 2328 cm^{-1} , with higher intensity, corresponding to symmetric B-H vibrations [16,17]. At 1601 cm^{-1} , asymmetric scissors deformation modes of NH_3 group appear with low intensity. The band with very low intensity

centered at 1377 cm^{-1} is associated to umbrella deformation modes of NH_3 group. At 1189 cm^{-1} a broad band is observed that is characteristic of overlapping scissors and umbrella deformation modes of BH_3 group. B-N stretching modes occur at lower frequency shifts; 799 cm^{-1} and 783 cm^{-1} for ^{10}B y ^{11}B isotopes respectively. Finally, a weak band near 727 cm^{-1} appears and is assigned to an N-B-H rocking mode [15].

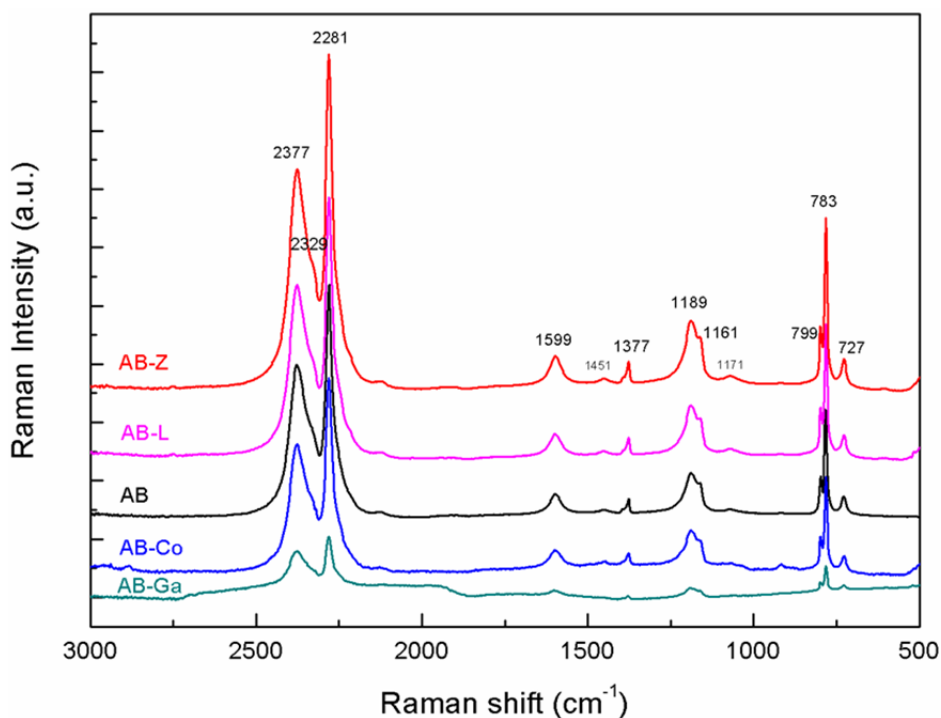


Figure 4.6: Raman spectra of AB-Ga, AB-Co, neat AB, AB-L and AB-Z

The Raman spectrum of AB-Co is similar to that of neat NH_3BH_3 , in terms of intensity and Raman shift for all vibrational modes. Thus, NH_3BH_3 phase is preserved through impregnation onto CoAPO-5. Similarly, the Raman spectra of NH_3BH_3 -supported on both silicates (AB-L and AB-Z) display the same vibrational modes than the spectra of the neat compound with no apparent shift, and NH_3BH_3 does not seem to be structurally modified upon impregnation into these two hosts. As shown in Figure 4.7 next, the silica hosts do not contribute to any modes of the Raman spectra.

In contrast, in the spectrum of NH_3BH_3 -supported Ga_2O_3 (AB-Ga), most of NH_3BH_3 vibrational modes are considerably weakened and broadened (see Figure 4.6), indicating an increased inhomogeneity of the crystal size of ammonia borane probably due to a higher interaction of AB with this support. Moreover, besides NH_3BH_3 typical bands, some other broad bands are visible in the range $2500\text{--}2000\text{ cm}^{-1}$ of the spectrum of NH_3BH_3 -supported Ga_2O_3 , probably corresponding to some vibrational modes of the support (Figure 4.7). Similarly, the weak peaks

observed in the AB-Co sample near 2800 cm^{-1} and below 1000 cm^{-1} can be attributed to the support.

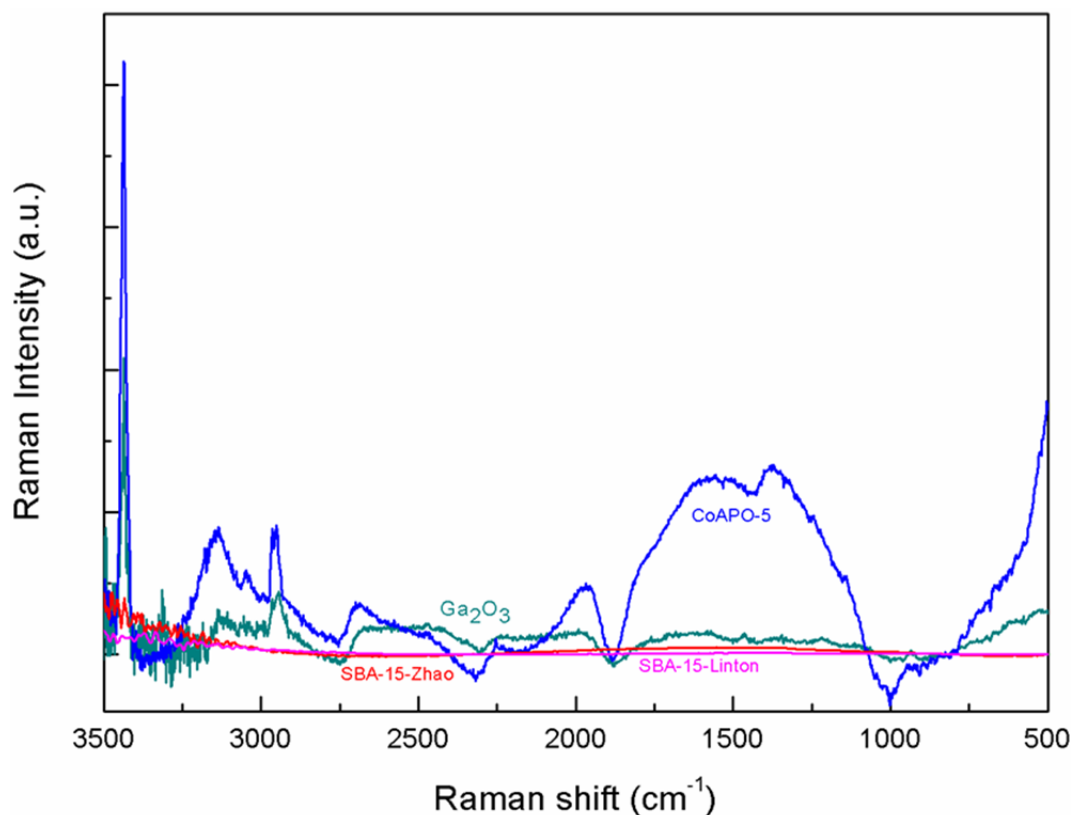


Figure 4.7: Raman spectra of CoAP-5, SAB-15-Z and SBA-15-L and mesoporous Ga_2O_3 used as host materials for ammonia borane

4.3.2 Operando Raman-Mass Spectrometry monitoring of the thermolysis of neat and porous-impregnated ammonia borane

4.3.2.1 Neat ammonia borane

Figure 4.8 illustrates the results of Raman – Mass Spectrometry monitoring of pure AB. As shown in Figure 4.8.C, hydrogen release from neat AB occurs in two stages, in agreement with the proposed mechanism of reactions (1) and (2) for AB thermal decomposition (see section 3.1), with a first decomposition peak near 109 °C, accompanied by strong bubbling and foaming of the sample as observed with the Raman system camera, and a second hydrogen release peak near 144 °C. These results are consistent with observations described in the literature [18,19,20]. Moreover, hydrogen release at 149 °C exhibits a concomitant release of borazine ($\text{B}_3\text{N}_3\text{H}_6$) while no traces of diborane (B_2H_6) or ammonia (NH_3) are detected up to 200 °C.

For easier understanding of structural changes in Figures 4.8.A to 4.12.A, Raman spectra acquired in temperature ranges where no hydrogen is evolved are plotted in brown, spectra

acquired when hydrogen evolution raises are plotted in blue, and spectra acquired when hydrogen evolution decreases are plotted in red. At room temperature, neat AB displays several Raman vibrational modes already described in sections 3.3.2 and 4.3.1.4. It can be seen that, under $1^{\circ}\text{C}\cdot\text{min}^{-1}$ ramp, spectral changes happen more suddenly and are more difficult to discern compared to Raman spectra evolution of AB samples acquired during isothermal decomposition at 90°C (see section 3.3.4). Figure 4.8.A shows how Raman modes maintain intensity and position until the sample approaches 98°C , when N-H stretching bands at 3313 and 3175 cm^{-1} and asymmetric H-N-H bending mode at 1601 cm^{-1} decrease slightly. As shown in Figure 4.8, as hydrogen evolution reaches maximum values, the mode at 1601 cm^{-1} of $-\text{NH}_3$ deformation [15] is lost, and a new mode becomes apparent at 1565 cm^{-1} , which is described as characteristic of $-\text{NH}_2$ species and can correspond to the formation of polymeric aminoborane (PAB) [21,22]. The intensity decrease becomes more evident as the temperature approaches 101°C , when the rest of vibrational modes, including those corresponding to B-H, H-B-H, B-N and N-B-H vibrations also weaken. As already reported for isothermal decomposition of neat AB at 90°C , early shifts can be observed for B-N stretching modes (see the inset in Figure 4.8). The vibrations for ^{10}B and ^{11}B near 799 and 783 cm^{-1} exhibit a slight redshift already between 38°C and 41°C . These two modes coalesce and dramatically weaken close to 106°C and are almost lost by 109°C . The mode near 783 cm^{-1} thus formed remains at higher temperatures, and is associated with the B-N vibrational mode in poliaminoborane ($-\text{[BH}_2\text{NH}_2\text{]}_n-$) [22], thus suggesting the formation of such phase. This band coexist with the very small shoulder at 853 cm^{-1} which is assigned to AB polymerization [23] and BH_2 modes from PAB [22]. In addition to a continuous loss of intensity and broadening of vibrational modes, a strong noise in the signal appears at Raman shifts higher than 3150 cm^{-1} above 100°C . The whole Raman spectrum suffers considerable transformations near 106°C , where all vibrational modes weaken and, concomitantly, hydrogen evolution becomes very intense at on line mass spectrometry reading (Figure 4.8.C).

The most apparent change in the $140\text{--}200^{\circ}\text{C}$ temperature range, during the second hydrogen release, happens in the B-H stretching mode region as the broad 2379 cm^{-1} band disappears and another band raises at 2509 cm^{-1} . This mode disappears above 150°C and is characteristic of B-H stretching modes in poliiminoborane ($-\text{[BHNH]}_n-$) [22], thus suggesting that the formation of such phase takes place.

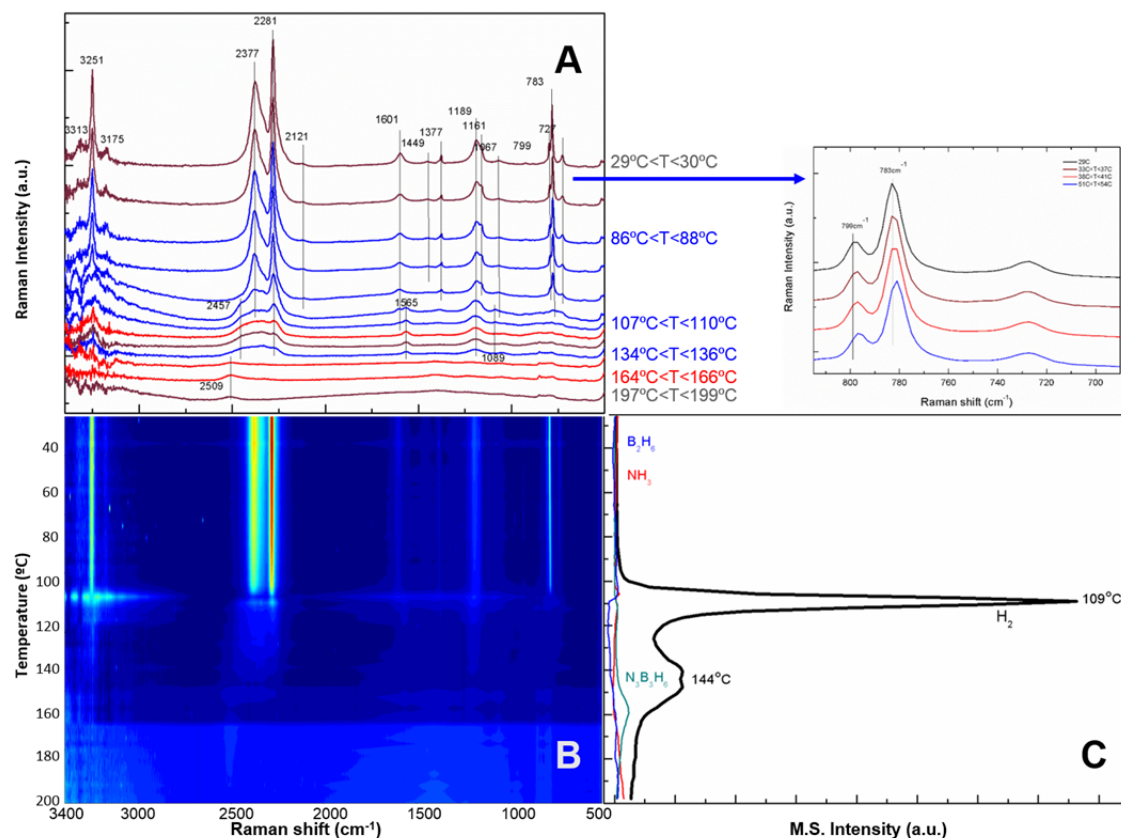


Figure 4.8: Representative Raman spectra (A), Raman intensity contour vs. temperature (B) and simultaneous MS profiles for H_2 and other volatile components (C) acquired during neat AB thermal decomposition under a ramp of $1^\circ\text{C}\cdot\text{min}^{-1}$. Inset shows early B-N stretching modes shift in Raman spectra for neat AB

4.3.2.2 Ammonia borane-impregnated CoAPO-5 (AB-Co) and gallium oxide (AB-Ga)

As shown in Figures 4.9 and 4.10, impregnation of AB over CoAPO-5 matrix or mesoporous Ga_2O_3 has little effect on hydrogen release behavior. Like in the case of neat AB, the release takes place through two main events. The maximum temperatures of the two hydrogen molecules release peaks observed in the samples confined in CoAPO-5 and Ga_2O_3 are practically identical to those observed with the neat hydride, with differences below 2°C (see Figure 4.13 next). However, some differences in the onset temperatures of hydrogen release can be observed: while in the case of neat AB no hydrogen release is observed at temperatures below 100°C , with the two confined samples some release is already appreciable at temperatures as low as 60°C , as indicated by the slow rise of the MS signal in this temperature range. This reduction in the temperature required to initiate H_2 release can be attributed to the destabilization of the fraction of AB that is nanoconfined within the pores of these hosts. It is also important to note how the second H_2 release step seems enhanced in AB-Co and AB-Ga MS profiles with respect to neat AB. In the case of AB-Co, the B_2H_6 MS profile shows a continuous but small increase from 80°C while no $\text{B}_3\text{N}_3\text{H}_6$ is detected. During AB-Ga decomposition, neither B_2H_6 nor $\text{B}_3\text{N}_3\text{H}_6$ are detected

by MS but only a small amount of NH_3 released simultaneously to H_2 as reported in section 3.3.4 (Figure 4.10).

Some minor differences are also observed in Raman spectra acquired during H_2 release. In the case of the AB-Co sample (Figure 4.9), H_2 release is already appreciable above 60 °C and considerable broadening of $\nu(\text{N-H})$ and $\delta(\text{N-H})$ modes can be observed between 73 °C and 79 °C, at about 25 °C lower temperatures than for the neat compound. The other Raman bands exhibit loss of intensity and broadening above 94 °C, when H_2 evolution gears up. From this point, the evolution of the Raman spectra is similar to that observed with the neat compound: during the first peak of hydrogen release, the NH_3 deformation mode at 1601 cm^{-1} is lost and the NH_2 mode at 1565 cm^{-1} becomes apparent, and the main event related to the second peak is again the evolution and disappearance of the broad peak near 2500 cm^{-1} , associated with B-H stretching modes in poliiminoborane [29] slight distortion of AB in the gallium matrix. Again, as hydrogen evolution reaches a maximum, the 1601 cm^{-1} vibration of $-\text{NH}_3$ groups shifts to 1565 cm^{-1} , which is characteristic of $-\text{NH}_2$ species [21,22] and decreases later. The 2377 and 2281 cm^{-1} $\nu(\text{BH})$ vibrations in NH_3BH_3 gradually weaken above 60 °C, when H_2 release slowly begins. From 97 °C, all the Raman bands exhibit a continuous decrease, just as H_2 reaches a maximum signal at the online analysis.

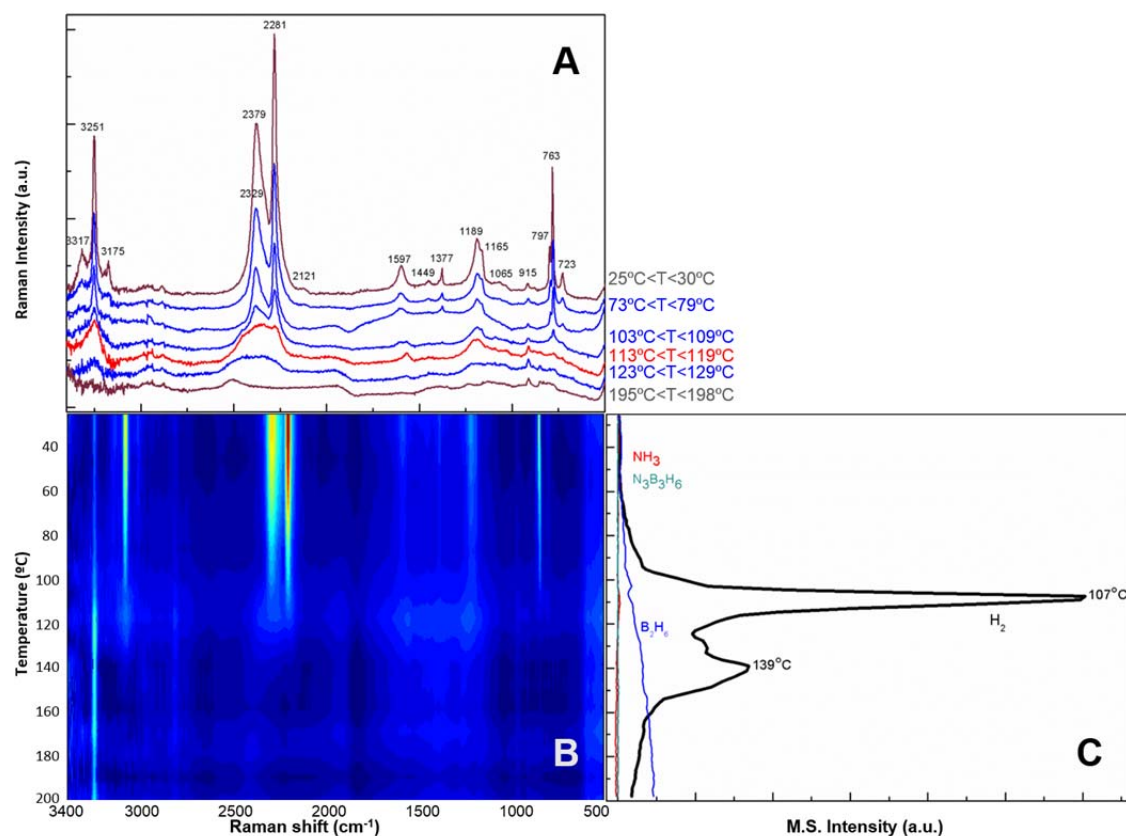


Figure 4.9: (A) Representative Raman spectra, (B) Raman contour vs. temperature and (C) mass spectrometry profiles for H₂ and other volatile components evolved during thermal decomposition of AB-Co under a ramp of 1 °C·min⁻¹

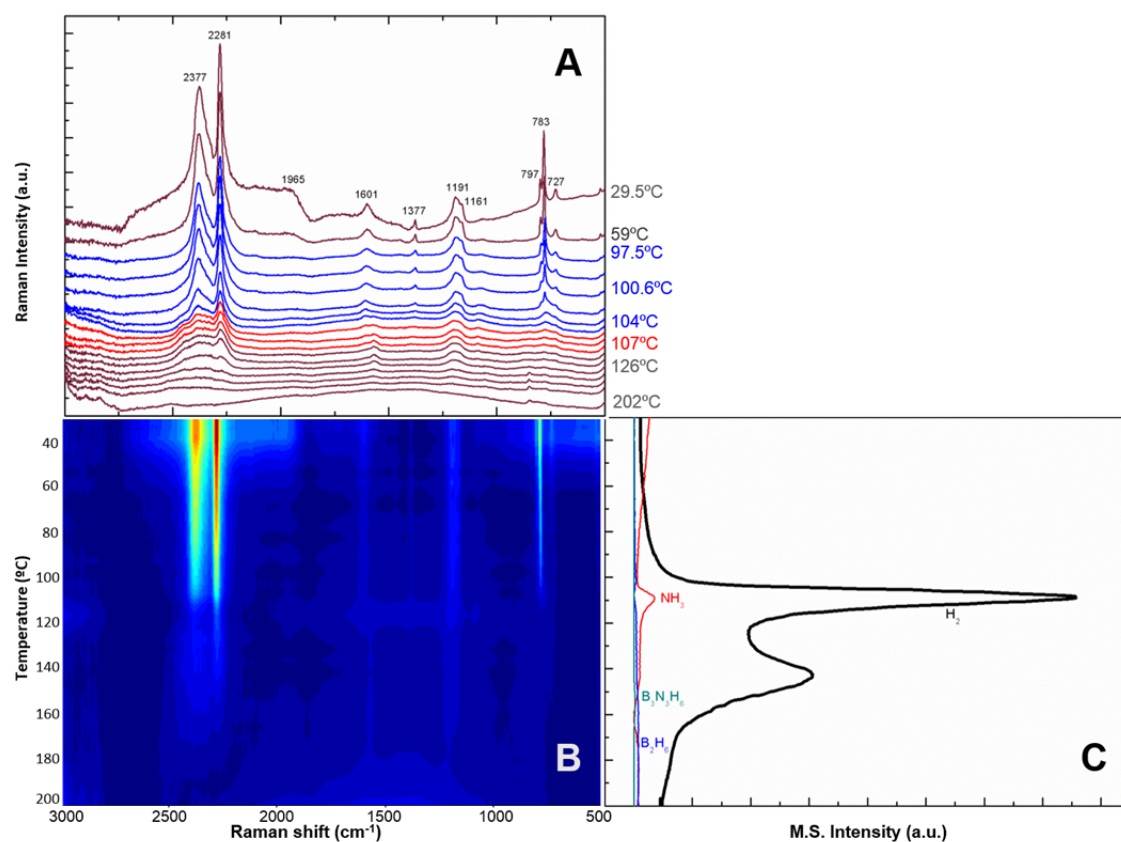


Figure 4.10: (A) Representative Raman spectra, (B) Raman contour vs. temperature and (C) mass spectrometry profiles for H₂ and other volatile components evolved during thermal decomposition of AB-Ga under a ramp of 1 °C·min⁻¹

4.3.2.3 Operando Raman-MS of ammonia borane-impregnated SBA-15 (AB-L and AB-Z)

As presented in Figures 4.11 and 4.12, and in contrast with the results obtained with the previous host materials, scaffolding ammonia borane into SBA-15 porous materials drastically decreases hydrogen desorption temperature with an onset of hydrogen release at temperatures as low as 40 °C, and makes the second hydrogen release peak hardly appreciable.

In particular, as shown in Figure 4.11, during the thermolysis of the AB-L sample, hydrogen mass profile exhibits a single desorption stage, consistently to what can be observed from Raman spectra and reported elsewhere [1]. Such a one-step H₂ release decomposition mechanism is similar to that described in section 3.4 for AB impregnated on Ga₂O₃ with 0.5:1 loading ratio. H₂ desorption occurs between 40 °C and 120 °C with a maximum at 97 °C although a shoulder can be observed between 120 °C and 160 °C in the MS profile. B₃N₃H₆ and NH₃ show completely flat

MS profiles during the decomposition of AB-L while B_2H_6 profile first starts raising slowly to suddenly decrease when hydrogen desorption gets quicker, probably due to dilution effects. Once hydrogen profile goes down, B_2H_6 curve begins raising again slowly up to 200 °C.

Raman spectra do not show significant changes until the samples reaches 86 °C, when all vibrational modes weaken at the same time. No change is apparent in the N-H modes ahead of the other vibrational modes. The Raman spectra intensity decreases from 97 °C to 112 °C, for all vibrational modes just when H_2 mass profile exhibits a deep decrease too. Raman spectra show very few bands above 112 °C. The only observable shift in the spectrum is the one suffered by $\nu(B-N)$ up to 800 cm^{-1} . The events of formation and extinction of the NH_2 characteristic peak near 1565 cm^{-1} , observed in Raman spectra of neat ammonia borane and in AB-Co and AB-Ga confined samples, are hardly appreciable in the Raman spectra of the AB-L sample. Similarly, the formation of a broad peak near 2500 cm^{-1} assigned to BH stretching modes in PIB, which was associated with the second hydrogen release peak from the former samples is not observed in the Raman spectra of AB-L.

As presented in Figure 4.12, these variations in the mechanism of AB decomposition and hydrogen release are even clearer in the case of the AB-Z sample. Online MS profiles show that H_2 desorption starts near 40 °C but Raman spectra do not show significant changes up to 66 °C. H_2 desorption occurs essentially through a single step peaking near 97 °C and a shoulder near 130 °C, practically the same temperature range that for AB supported on SBA-15-L. During AB-Z decomposition, none of the usual impurities from AB decomposition is detected by MS. There is a very sharp intensity loss for all Raman modes when the sample reaches 96 °C and the spectrum becomes almost flat, just as H_2 MS profile starts decreasing. Comparing the Raman spectra obtained with the two SBA-15 supports, the attenuation of the two characteristic peaks corresponding to B-H stretching at 2380 cm^{-1} and 2280 cm^{-1} is more symmetric in the case of SBA-15-Z as decomposition of the sample takes place, with no hints of formation of the broad B-H peak associated with polyiminoborane. At higher temperatures, the only change that can be observed is a shift of the one vibrational mode remaining, $\nu(B-N)$ to higher Raman shifts, up to 801 cm^{-1} .

The considerable differences between thermal behaviors of the five samples described here regarding H_2 release performance are evident if the corresponding H_2 MS profiles are gathered as in Figure 4.13 next. There, it can be seen how neat AB, AB-Co and AB-Ga release H_2 through two consecutive steps, the second one being enhanced in the cases of AB-Co and AB-Ga which also show a decrease in the onset temperature for the first H_2 release step, probably due to a small fraction of AB that may have been confined in the pores. In contrast, the unique H_2

desorption event for AB impregnated SBA-15 materials begins around 40 °C as reported earlier and is almost done when the first H₂ release from neat AB starts.

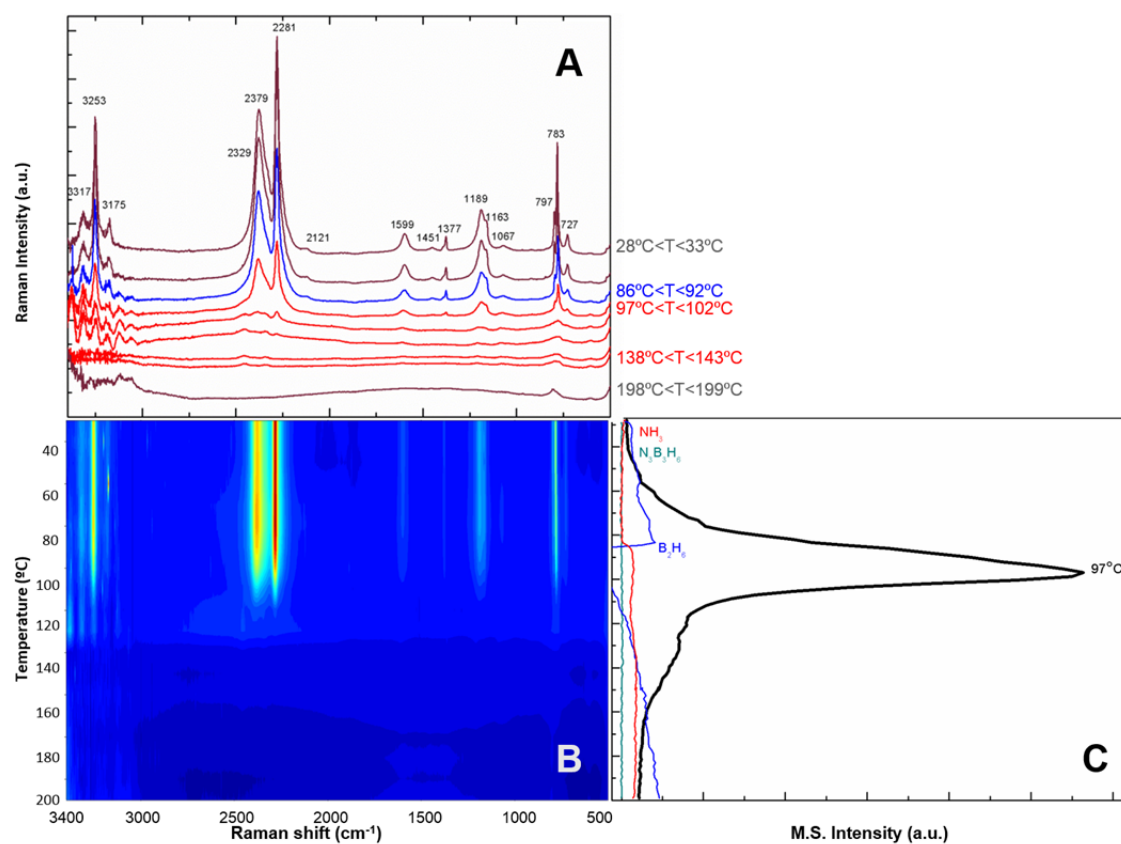


Figure 4.11: (A) Representative Raman spectra, (B) Raman contour vs. temperature and (C) mass spectrometry profiles for H₂ and other volatile components evolved during thermal decomposition of AB-L under a ramp of 1 °C·min⁻¹

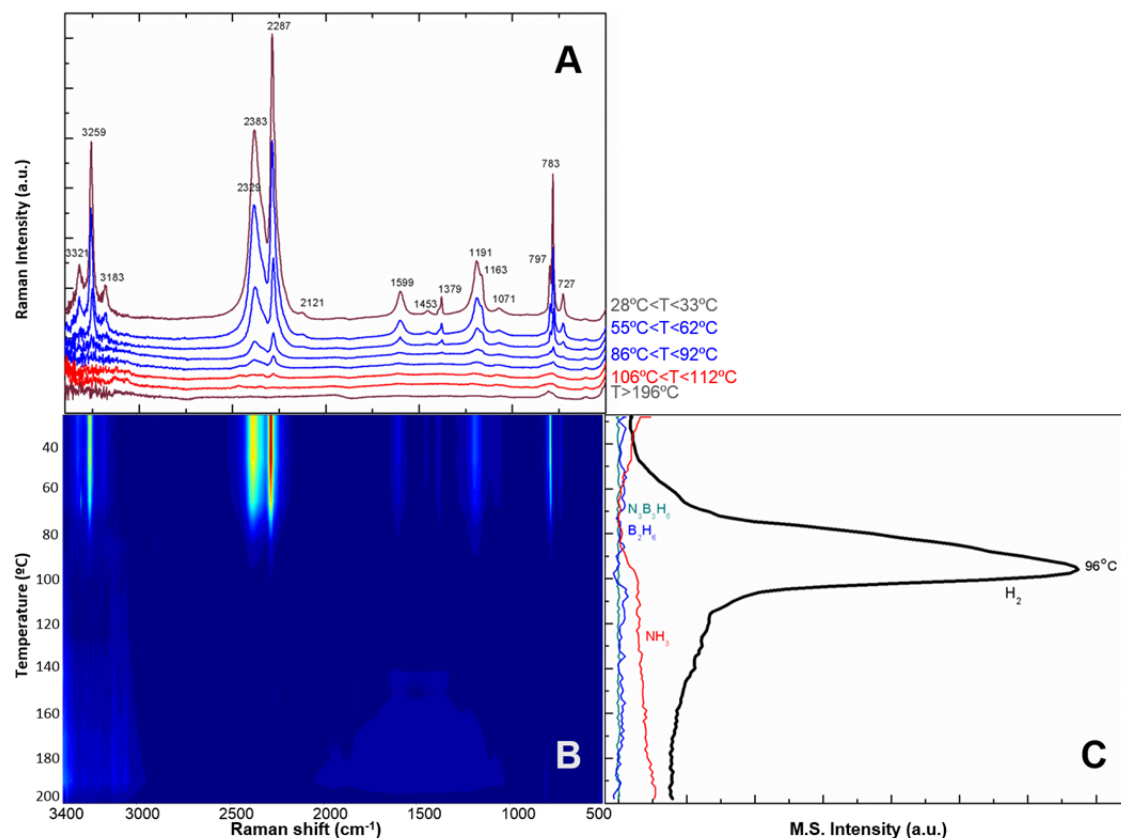


Figure 4.12: (A) Representative Raman spectra, (B) Raman contour vs. temperature and (C) mass spectrometry profiles for H₂ and other volatile components evolved during thermal decomposition of AB-Z under a ramp of 1 °C·min⁻¹

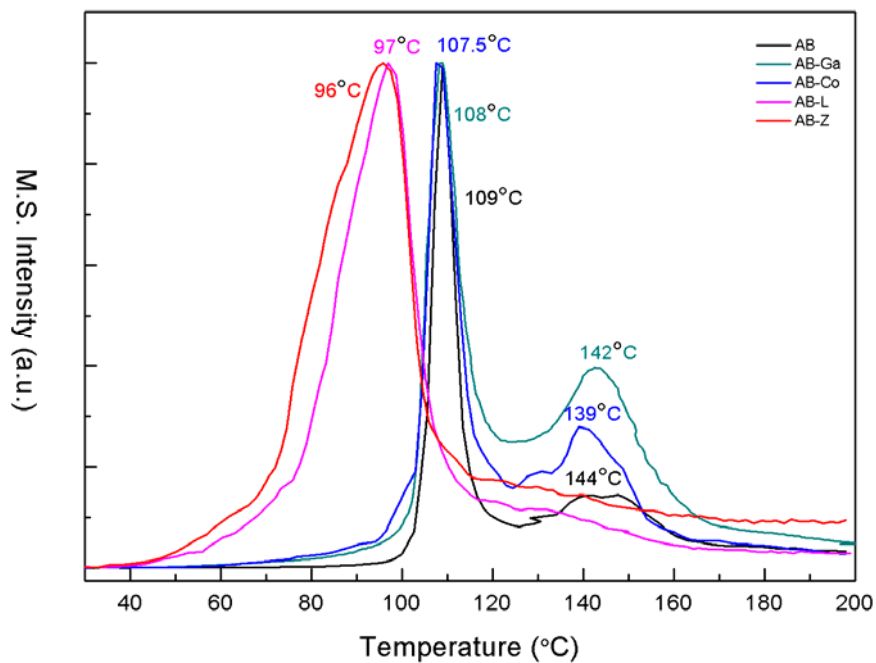


Figure 4.13: Normalized H₂ mass profiles corresponding to thermal decomposition of neat and impregnated AB samples under a ramp of 1°C·min⁻¹

4.4 Discussion

Ammonia borane has been impregnated into four different porous hosts. SBA-15 materials show pore volumes three to four times bigger than those of CoAPO-5 and Ga_2O_3 with homogeneous pore size distribution centered around 6.4 nm and 7.8 nm which have been confirmed by TEM and shown to offer a uniform distribution. Through impregnation, SBA-15-Z and Ga_2O_3 seem to conserve their initial structure while those of CoAPO-5 and SBA-15-L apparently suffer some distortion as their textural properties appear modified upon AB impregnation.

XRD confirm the existence of crystalline ammonia borane, but with a certain attenuation and broadening of AB diffraction peaks. These results suggest nanoconfinement of at least a fraction of this compound within the pores of the hosts. In the diffraction pattern for AB-Co, the AB peaks distortion seems less significant although the CoAPO-5 peaks appear shifted. This may indicate a smaller fraction of AB is confined in such support which however seems to cause a structural change in CoAP-5 framework, consistently to changes of this structure observed by N_2 adsorption isotherms.

Raman spectroscopy for AB-Co, AB-L and AB-Z show spectra very similar to that of neat AB. NH_3BH_3 phase is then preserved through impregnation process while AB Raman bands appear considerably distorted in AB-Ga spectrum. This could indicate some interaction between AB and Ga_2O_3 as already introduced in chapter 3.

Operando Raman-MS measurements under $1^\circ\text{C}\cdot\text{min}^{-1}$ appear as the key to confirm if AB confinement in the porous structure really takes place and to what extent it does. Neat AB analysis first reveals some structural changes concomitant to the two steps H_2 release mechanism already described in previous chapters. These changes reveal NH_3 stretching and deformation bands change previously to the collapse of the rest of Raman bands. The formation of PAB is observed through the appearance of small Raman characteristics of such phase when the first H_2 step reaches its maximum while no trace of DADB bands are seen as they are more difficult to discern under $1^\circ\text{C}\cdot\text{min}^{-1}$ ramp because spectral changes happen more suddenly compared to those detected during AB isothermal decomposition at 90°C (see section 3.3.4). The only observable change during the second H_2 release step from neat AB is the appearance of a B-N band from PIB. In addition, a blueshift of B-N bands from AB is observed to happen between 38°C and 41°C (see the inset in Figure 4.8) As already reported in section 3.4, the formation of a new phase of mobile AB (AB^*) which is essential for hydrogen release during AB thermal decomposition was demonstrated by means of *In situ* NMR and XRD data by Shaw et al. [24]. Such process would involve a relaxation of the extensive dihydrogen bonding structure allowing easy B-N axis rotation which is probably related to the early blueshift of the B-N. This

bond relaxation was reported to account for the facilitated hydrogen release from AB into MCM-41 pore structure [25] and seems to be detected here for dehydrogenation of neat AB as well by Raman spectroscopy.

AB impregnated on CoAPO-5 and mesoporous Ga_2O_3 shows H_2 release properties similar to those of neat AB with a mechanism which goes through two consecutive steps with the same maximum temperatures. The only observable differences are the lower onset temperatures for the first dehydrogenation step and the enhancement of H_2 yield during the second step with suppression of $\text{B}_3\text{N}_3\text{H}_6$ release. In the case of AB-Ga, a small NH_3 release is detected simultaneously to the first H_2 desorption. Such slight changes in AB decomposition may be due to only a small fraction of the compound being confined in CoAP-5 and Ga_2O_3 . As microscopy suggests and isotherms confirm, these materials possess poorly accessible mesopore structures. CoAPO-5 shows a modest intercrystalline mesoporosity and microporosity with a monodimensional channel array while Ga_2O_3 exhibits some mesoporosity, but its total pore volume is very limited. Thus, these two materials hardly exhibit capacity to host AB into nanoscaled porous structure, and so little nanoconfinement effects are detected. Nevertheless, the higher H_2 yield and suppression of $\text{B}_3\text{N}_3\text{H}_6$ release during the second H_2 desorption peak are quite relevant and could be related to a Lewis acid-base interaction of AB with the active species from the oxidic material surfaces. During AB-Ga decomposition, the destabilizing effect on the apparently small AB fraction that may be confined could probably take place through the formation of bounds between $\text{H}^\delta+$ species from the Ga_2O_3 surface and the hydridic H of BH_3 in AB as described elsewhere for other supports and which would favor NH_3 desorption [26,27,28].

Operando Raman-MS analyses for AB/SBA-15 material exhibit very different results. For AB-L and AB-Z, only one dehydrogenation is observed which gets started at temperatures as low as 40 °C with a maximum release around 97 °C. The spectral Raman changes described for neat AB are hardly appreciable in these cases as all the vibrational modes suddenly collapse when H_2 release is more intense and so, no previous intensity decrease is observed in $-\text{NH}_3$ bands for these materials. Besides the drastic changes in the main dehydrogenation event, neither second H_2 desorption nor impurities release are detected.

The results obtained with the four hosts reported here indicate that two main effects can take place during decomposition of impregnated AB. On one hand, physical nanoconfinement of AB within the porous structure of the host facilitates H_2 release during thermolysis, minimizing undesired BNH_x fragments. Comparison of pore structure shows that nanoconfinement is critical for such a change, resulting in a dramatic effect for two kinds of SBA-15 materials for 1:1 AB loading charges, giving similar results that those described in chapter 3 for half that amount of AB

impregnated on Ga₂O₃. Optimum AB loading level on the porous host depends then on the capacity of this material for holding AB in its pores. Therefore, confinement of AB onto porous materials offering easily accessible pores with diameters in the range of 7 nm produces considerable enhancement of dehydrogenation properties of AB as previously reported [1,3,29]. On the other hand, AB decomposition features seem to also be enhanced by chemical interactions between AB and active species from the host surface indicated by the evolution of Raman spectra which point to a different mechanism of decomposition of AB impregnated on SBA-15 materials. Such interactions were suggested to happen between AB and hydroxyl groups from the silica surface of the host by Lai et al [3]. These groups can interact with the BH₃ group, loosening the covalent bond between BH₃ and NH₃ groups of AB, thus destabilizing and promoting the decomposition of the compound. Furthermore, by this interaction BH₃ is kept bound to the scaffold reducing the production of borazine and precluding the formation of poliiminoborane consistently to what was observed during *operando* Raman-MS experiments. In the case of Ga₂O₃-supported AB, such interactions may be stronger as it would induce NH₃ release concomitantly to H₂ desorption.

4.5 Conclusions

Ammonia borane thermal decomposition has been studied when this compound is impregnated with 1:1 loading level on four porous materials displaying very different textural properties. For mesoporous Ga₂O₃ which pores volume is limited and microporous CoAPO-5 with poor intercrystalline mesoporosity, H₂ desorption performance are very similar to those from neat AB with some subtle improvements regarding the onset temperature for the first dehydrogenation step or the release of impurities despite some NH₃ desorption detected for AB-Ga. These effects indicate that only a small fraction of AB that is confined into these materials structures. In contrast, in the case of SBA-15 materials which possess highly ordered mesopores distribution, very important improvements are obtained. A single H₂ release peak at temperatures significantly lower and very different Raman spectra indicate a change in the mechanism of decomposition of AB that may be induced by all the impregnated AB being confined into the bigger pores of SBA-15 supports which porosity is more accessible than for CoAPO-5 and Ga₂O₃. The absence of impurities release also suggests some interactions between surface hydroxyl groups of silica matrixes with the BH₃ group of AB. These effects are very similar to those obtained in chapter 3 for Ga₂O₃ with an AB loading level of 0.5:1.

Based on this, we expect that an appropriate combination of nanoconfinement and chemical environment would facilitate tuning a cleaner hydrogen release by thermolysis of porous impregnated ammonia borane materials.

References

- [1] Gutowska A., Li L., Shin Y., Wang Ch.M., Li X.S., Linehan J.C., Smith R.S., Kay B.D., Schmid B., Shaw W., Gutowski M., Autrey T., *Angew. Chem. Int. Ed.* **44** (2005) 3578-3582
- [2] Nielsen T.K., Manickam K., Hirscher M., Besenbacher F., T.R. Jensen, *Nanoscale* **3** (2011) 2086- 2098
- [3] Lai S.W., Lin H.L., Yu T.L., Lee L.P., Weng B.J., *Int. J. Hydrogen Energy* **37** (2012) 14393–14404
- [4] Manjón-Sanz A., Sánchez-Sánchez M., Muñoz-Gómez P., García R., Sastre E., *Micropor. Mesopor. Mater.* **131** (2010) 331-34
- [5] Linton P., Alfredson V., *Chem. Mater.* **20** (2008) 2878-2880
- [6] Gascón V., Díaz I., Márquez-Álvarez C., Blanco R.M., *Molecules* **19** (2014) 7057-7071
- [7] Zhao D., Feng J., Huo Q., Melosh N., Fredrickson G.H., Chmelka B.F., Stucky G.D., *Science* **279** (1998) 548-552
- [8] Deshmane C.A., Jasinski J.B., Carreon M.A., *Eur. J. Inorg. Chem.* **22** (2009) 3275–3281
- [9] Sing K.S.W., Everett D.H., Haul R.A.W, Moscou L., Pierotti R.A., Rouquerol J., Siemieniowska T., *Pure Appl. Chem.* **57** (1985) 603–619
- [10] Brunauer S., Emmet P.H., Teller E., *J. Am. Chem. Soc.* **60** (1938) 309-319
- [11] Barrett E.P., Joyner L.G., Halenda P.P., *J. Am. Chem. Soc.* **73** (1951) 373-380
- [12] Linton P., Rennie A.R., Alfredsson V., *Solid State Sci.* **13** (2011) 793-799
- [13] Zhao Y., Zhang J., Akins D.L., Lee J.W., *Ind. Eng. Chem. Res.* **50** (2011) 10024–10028
- [14] Cullity D.B., Stock S.R. *Prentice-Hall* (3rd Edition), Upper Saddle River, NJ (2010)
- [15] Hess N.J., Bowden M.E., Parvanov M.V., Mundy C., Kathmann S.M., Schenter G.K., Autrey T., *J.Chem.Phys.* **128** (2008) 034508 1-11
- [16] Dillen J., Verhoeven P., *J. Phys. Chem. A* **107** (2003) 2570-2577
- [17] Trudel S., Gilson D.F.R., *Inorg. Chem.* **42** (2003) 2814-2816
- [18] Wolf G., Baumann J., Baitalow F., Hoffmann F.P., *Thermochim. Acta* **343** (2000) 19-25
- [19] Baitalow F., Baumann J., Wolf G., Jaenicke-Röbler K., Leitner G., *Thermochim. Acta* **391** (2002) 159-168
- [20] Baumann J., Baitalow F., Wolf G., *Thermochim. Acta* **430** (2005) 9-14
- [21] Dresser M.J., Taylor P.A., Wallace R.M., Choyke W.J., Yates J.T. Jr., *Surf. Sci.* **218** (1989) 75–107
- [22] Chellappa R.S., Autrey T., Somayazulu M., Struzhkin V.V., Hemley R.J., *Chem. Phys. Chem.* **11** (201) 93-96
- [23] Frueh S., Kellett R., Mallery C., Molter T., Willis W.S., King'ondeu C., Suib S.L., *Inorg. Chem.* **50** (2011) 783–792
- [24] Shaw W.S., Bowden M., Karkamkar A., Howard C.J., Heldebrandt D.J., Hess N.J., Linehan J.C., Autrey T., *Energy Environ. Sci.* **3** (2010) 796–804
- [25] Kim H., Karkamkar A., Autrey T., Chupas P., Proffen T., *J. Am. Chem. Soc.* **131** (2009) 13749–13755
- [26] Moussa G., Bernard S., Demirci U.B., Chiriac R., Miele P., *Int. J. Hydrogen Energy* **37** (2012) 13437-13445

[27] Li L., Yao X., Sun C., Du A., Cheng L., Zhu Z., Yu C., Zou J., Smith S.C., Wang P., Cheng H.M., Frost R.L., Lu G.Q., *Adv. Funct. Mater.* **19** (2009) 265–271

[28] Li S.F., Tang Z.W., Tan Y.B., Yu X.B., *J. Phys. Chem. C* **116** (2012) 1544–1549

[29] Park J.H., Kim S.K., Kim H.S., Cho Y.J., Park J., Lee K.E., Yoon C.W., Namb S.W., Kang S.O., *Chem. Commun.* **49** (2013) 10832–10834

Chapter 5

Dehydrogenation of Ethane 1,2-diamineborane

Summary

Ethane 1,2-di-amineborane ($\text{BH}_3\text{NH}_2\text{CH}_2\text{CH}_2\text{NH}_2\text{BH}_3$, EDAB hereafter) samples have been synthesized by reacting ethylenediamine dihydrochloride with sodium borohydride in tetrahydrofuran solution. Structural and bonding properties of EDAB have been characterized by means of liquid-state Nuclear Magnetic Resonance, X-ray Diffraction and Raman spectroscopy. The thermolytic decomposition of EDAB has been investigated by means of combined thermogravimetry, differential thermal analysis and mass spectrometry measurements, both under vacuum and inert gas flow conditions. These experiments allow determining the enthalpies and activation energies of two hydrogen-desorption stages below 250 °C as well as the yields and purity of the released gases. These results show that EDAB presents a thermal stability, both under vacuum and under inert gas flow, higher than that of its parent counterparts methylamine borane ($\text{BH}_3\text{NH}_2\text{CH}_3$) and ammonia borane (BH_3NH_3). Contrary to those compounds, EDAB releases pure hydrogen when heated under inert flow. In contrast, moderate fractions of diborane, residual tetrahydrofuran, and volatile B–N–C–H species are released when conducting the experiments under dynamic vacuum.

Operando Raman-mass spectrometry experiments provide insight into the EDAB thermolysis reaction mechanism.

5.1. Introduction

In the frame of solid-state materials potentially useful for hydrogen storage, a great research activity has been devoted to a number of hydride systems with particular interest in boron-nitrogen-hydrogen compounds such as NH_3BH_3 (ammonia borane, AB). But, as already mentioned in previous chapters, the practical use of AB for hydrogen storage applications is impeded by the concurrent release of contaminant gases such as diborane or borazine. In addition, the obtained polymeric iminoborane product ($[\text{NHBH}]_n$) is very stable and difficult to regenerate to yield AB by direct hydrogen gas sorption. Different possibilities for overcoming the intrinsic limitations of AB were summarized in chapter 1. Chapters 3 and 4 described the confinement of AB in porous materials for enhancing AB dehydrogenation properties. Another alternative for tuning AB hydrogen desorption properties consist in performing chemical modification of AB molecules. This approach has led to the synthesis of novel compounds such as the alkali amidoboranes, which present improved characteristics from the point of view of hydrogen storage applications [1]. Carbon derivatives of AB such as methylamine borane ($\text{BH}_3\text{NH}_2\text{CH}_3$, MeAB hereafter) and ethane 1,2-di-amineborane ($\text{BH}_3\text{NH}_2\text{CH}_2\text{CH}_2\text{NH}_2\text{BH}_3$, EDAB hereafter) were firstly synthesized in the 60's and have experienced a renewed interest in the framework of hydrogen storage applications. Both compounds are crystalline solids at room temperature, quite stable in air and release high yields of hydrogen at moderate temperatures. From the point of view of its hydrogen desorption properties MeAB presents some disadvantages as compared to AB as that it sublimates at moderate temperatures [2]. This fact has discouraged further research on MeAB for hydrogen storage applications. By contrast, EDAB possesses some advantages over AB and, therefore, further research on that compound should be desirable. Indeed, as far as we know, there are only few works investigating the hydrogen desorption properties of EDAB [3-5]. In particular, there is only one previous contribution on the thermolysis of pure EDAB samples [4]. According to that work, EDAB releases *ca.* 10 wt% of pure hydrogen below 200 °C in a two-step process. Moreover, the enthalpy of hydrogen release from EDAB is less exothermic than that of AB. Such a difference can be relevant regarding handling of the corresponding heat release during hydrogen desorption processes in hydrogen storage reservoirs.

Several synthetic routes have been reported so far in the literature to obtain EDAB. The first work by Kelly and Edwards reported the synthesis of EDAB by reacting ethylenediamine with diborane under vacuum [6]. However, this reaction is highly exothermic and must be accomplished at low temperatures. The same authors reported another method, which consists in reacting a tetrahydrofuran (THF) solution of ethylene diamine with borane-THF adduct [4,6]. That synthesis route was more convenient to produce larger quantities of EDAB, although it remains still quite sophisticated, including a rather high number of steps, some of them at low temperature. In this study we have followed a different approach to obtain EDAB samples using a synthesis route reported in the early works on EDAB. It consists of the reaction of ethylene diamine dihydrochloride and sodium borohydride in THF [7,8]. This synthetic approach has the advantage of being simpler than those

previously mentioned and it can be accomplished at room temperature. A similar approach has also been reported to prepare MeAB, using methylamine hydrochloride and sodium borohydride in THF solution [2]. The previous works reporting this EDAB synthesis method identified the reaction product using infrared (IR) spectroscopy [8]. Here we present additional evidence on the successful synthesis of EDAB through this route, based on its characterization by liquid-state Nuclear Magnetic Resonance (NMR), X-ray diffraction (XRD) and Raman spectroscopy.

In this chapter, the thermolysis of EDAB has been investigated under both inert gas flow and vacuum conditions by means of Differential Thermal Analysis (DTA) coupled to Thermal Gravimetric Analysis (TGA) and Mass Spectrometry (MS). Insight on the reaction pathways for hydrogen release has been obtained by combining real-time Raman spectroscopy during thermolysis with simultaneous online mass spectrometry (MS) of the effluents (*operando* Raman-MS investigation [9]). This experimental approach has already been used in chapters 3 and 4 to get high-quality Raman spectra during thermal decomposition of the material under study with simultaneous mass spectrometric analysis of outlet gas stream. This represents a suitable approach for monitoring the bonding properties of EDAB during its thermolytic decomposition, thus giving information on the reaction products and the mechanism for hydrogen desorption.

5.2. Experimental section

5.2.1 Synthesis of EDAB

EDAB samples were synthesized by reaction of ethylene diamine dihydrochloride and sodium borohydride. In a typical experiment, to a suspension of sodium borohydride (37 mmol) in anhydrous THF (250 mL), ethylene diamine dihydrochloride (18 mmol) was added and the reaction mixture was stirred, at room temperature, for 24 h. Subsequently, the residual solids were filtered off and the solvent removed in vacuo yielding EDAB as a white crystalline solid (1.36 g; 86 %). Such preparations were made in collaboration with prof. Elena Pérez Mayoral at the Department of Inorganic Chemistry (UNED, Madrid).

EDAB was isolated as a totally pure sample as demonstrated by NMR, XRD and Raman spectroscopy as shown below.

5.2.2 Characterization of EDAB

To get insight into the chemical bonds forming EDAB molecule, NMR spectroscopic experiments were performed in D₂O solution, at 20 °C on a Bruker Avance spectrometer (500 MHz for ¹H). These measurements were made in collaboration with prof. Elena Pérez Mayoral at the Department of Inorganic Chemistry (UNED, Madrid). Chemical shifts (δ) in D₂O were referenced to CDCl₃ in the case of ¹H and ¹³C signals and to BF₃OEt₂ for ¹¹B experiments. The corresponding NMR Data were given in section 2.2.10. NMR measurements were completed with XRD analyses for further understanding EDAB molecular structure. XRD was accomplished in

a Philips X'PERT apparatus using the Cu-K α (wavelength 1.5406 Å) radiation with a data collection in the 2 θ range of 16.00°-90.00° applying 2 θ steps of 0.04° and accumulation times of 5 s. The obtained diffraction pattern was refined by the Rietveld method using FullProf software [10,11].

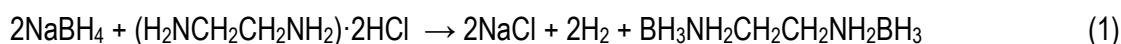
Combined DTA-TGA-MS measurements were performed as described in section 2.2.7.

The *operando* Raman- MS analyses were run fitting an online mass spectrometer downstream the *operando* cell located in the Raman spectrometer, which is described in chapters 3 and 4 for AB thermolysis studies. Each sample was confined in the spectroscopic cell, SiC was placed upstream and downstream the sample bed and this system was introduced in the *ad-hoc* oven described above. Tests were made using 0.03 g of sample sieved to 250-420 μ m particle size range and Raman acquisition consisted of 10 scans of 6 s each. Thus, the described system allows following hydrogen and other possible volatile components evolution with online mass spectrometry analysis of the outlet gas stream during EDAB decomposition in the Raman cell.

5.3 Results

5.3.1 Synthesis and characterization of EDAB

EDAB was synthesized from ethylene diamine dihydrochloride ((H₂NCH₂CH₂NH₂)·2HCl) and sodium borohydride (NaBH₄) in anhydrous THF (C₄H₈O), at room temperature, according to the following reaction [7,8]:



NMR measurements reveal that the obtained EDAB samples are phase-pure as can be seen in Figure 5.1 next. ¹H NMR spectra show a single resonance at δ 2.95 and a quadruplet signal between 1.13 and 1.67 ppm exhibiting a coupling constant $J_{\text{B-H}}$ of 86 Hz. These resonances are characteristic of CH₂ and BH₃ groups, respectively. Solution ¹¹B coupled NMR spectra show a quadruplet signal between -20.04 and -21.76 ppm, which is consistent with a tetrahedrally coordinated boron. Finally, solution ¹³C decoupled NMR spectra show a single resonance at 45.66 corresponding to the CH₂ groups. Both ¹¹B and ¹³C NMR data are in good accordance with those reported by Neiner et al. [4].

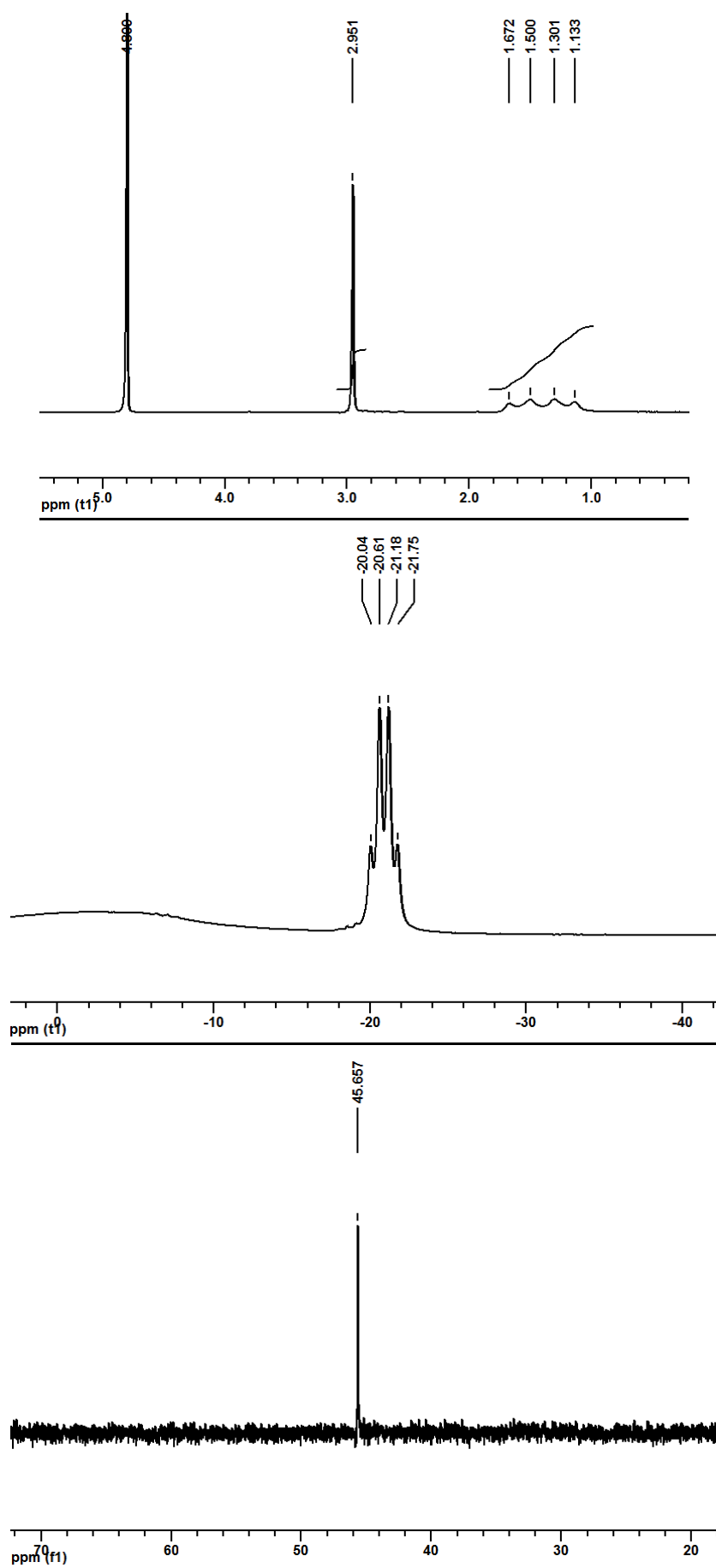


Figure 5.1: ^1H (top), coupled ^{11}B (middle) and decoupled ^{13}C (bottom) NMR spectra for EDAB

The typical XRD pattern of the as-prepared sample is shown in Figure 5.2. The peak positions and relative intensities of all diffraction peaks in this pattern are in good agreement with those previously reported for EDAB [4,10]. Rietveld refinement of the experimental data points (red line in Figure 5.2) has been done by considering an orthorhombic cell of the *Pbca* space group. The obtained lattice parameters are $a = 10.700$ (1) Å, $b = 8.134$ (1) Å and $c = 8.081$ (1) Å, which are in good agreement with previously reported values [12]. This result confirms that the product of reaction (1) is EDAB, as it was previously reported based on IR characterization [8].

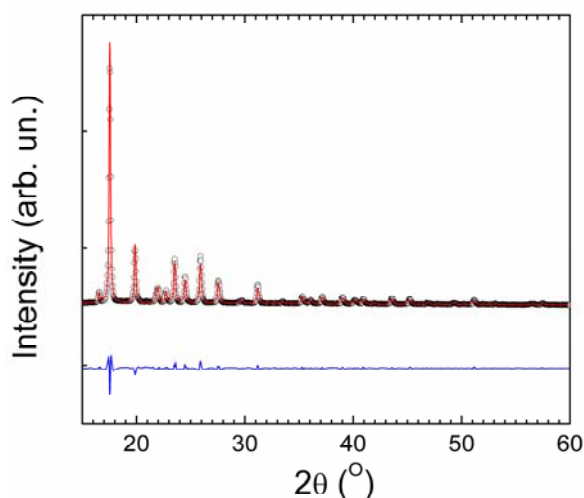


Figure 5.2: XRD pattern of fresh made EDAB samples at room temperature. Open symbols represent experimental data points whereas the red and blue lines are the calculated profile by using Rietveld refinement and the difference between experimental and calculated profiles, respectively

Raman spectra for EDAB at room temperature are depicted in Figure 5.3 while the peak positions are listed in Table 5.1. It must be noticed that in literature, only assignment of the vibrational spectrum of EDAB which was done on the basis of a cyclic structure for EDAB molecules with *gauche* conformation was found [7]. However, later studies revealed that EDAB presents an open-chain structure with *trans* conformation [12]. Therefore, the assignment of IR and Raman bands in EDAB should be reexamined. However, the spectra present a very rich structure and their proper interpretation would require detailed *ab initio* or DFT calculations. Here, a tentative assignment of Raman peaks has been done based on their comparison with those previously reported for IR spectrum of EDAB [7] as well as for Raman spectra of AB [13] and MeAB ($\text{CH}_3\text{NH}_2\text{BH}_3$) [14], as shown in Table 5.1. The frequencies of the N-H stretching vibration modes decrease following the sequence $\text{AB} > \text{MeAB} > \text{EDAB}$. This feature indicates a progressive weakening of the N-H bond from AB to EDAB. By contrast, there is a slight blueshift of the B-H stretching bands in EDAB and MeAB as compared to AB. This points out that MeAB and EDAB present a B-H bond that is slightly stronger than that of AB. On the other

hand, the B-N stretching band appears at wavenumber values in EDAB and MeAB lower than those in AB, indicating a softening of B-N bonds. However, in spite of this softening, MeAB and EDAB molecules present a relatively higher thermal stability as compared to that of AB (this aspect will be further discussed) because of the existence of strong C-N and C-C bonds.

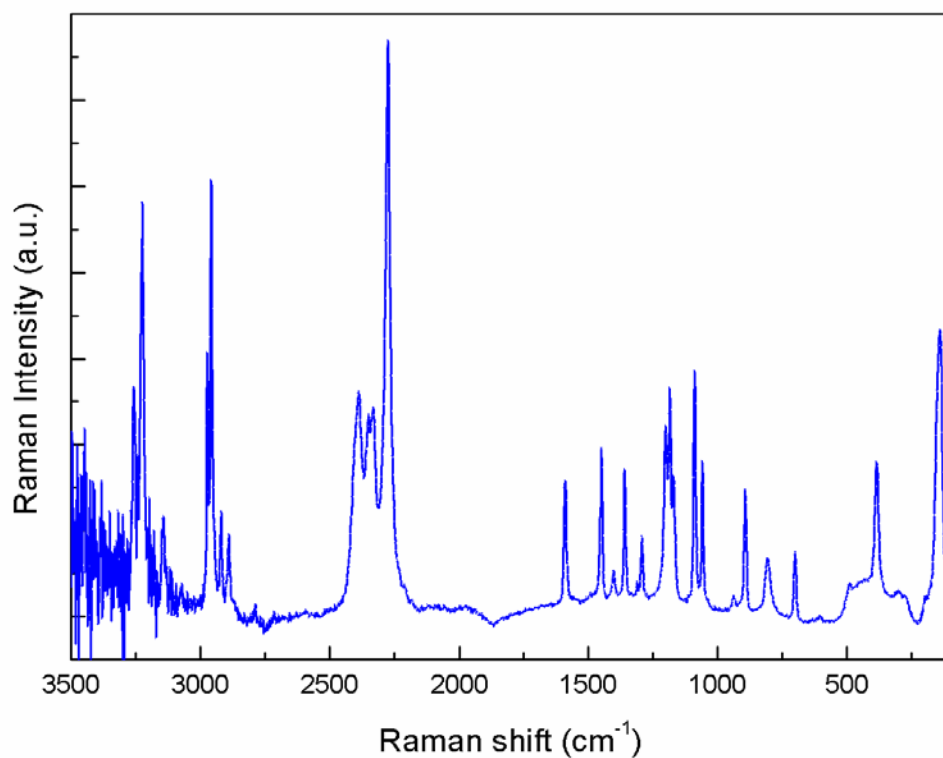


Figure 5.3: Room temperature Raman spectrum of EDAB

Table 5.1: Position of Raman peaks (cm^{-1}) and their tentative assignment for AB (NH_3BH_3), MeAB ($\text{CH}_3\text{NH}_2\text{BH}_3$) and EDAB ($\text{BH}_3\text{NH}_2\text{CH}_2\text{CH}_2\text{NH}_2\text{BH}_3$)

NH_3BH_3		$\text{CH}_3\text{NH}_2\text{BH}_3$		$\text{BH}_3\text{NH}_2\text{CH}_2\text{CH}_2\text{NH}_2\text{BH}_3$	
Peak	Ass. [13]	Ass.	Peak [14]	Peak	Ass. [this study]
3316	N-H str.	N-H asym. str.	3267	3257s	N-H asym. str.
3250	N-H str.		3241	3225s	N-H asym. str.
3176	ov?	N-H sym. str.	3161	3145m	N-H sym. str.
		C-H str.	3020 ^a	2973s	C-H asym. str.
		C-H str.	2960 ^a	2959vs	C-H asym. str.
			2905 ^a	2921m	ov. (2x1462)
			2820 ^a	2891m	C-H sym. str.
					C-H sym. str.
2375	?	B-H str.	2405 ^a	2389s	B-H str.
2328	B-H str.	B-H str.	2375 ^a	2351s	B-H str.
		B-H str.	2350 ^a	2331s	B-H str.
2279	B-H str.	ov	2275 ^a	2275vs	B-H str.
1600	N-H ds	N-H ds	1600 ^a	1593s	N-H ds
1450	ov?	C-H ds	1470 ^a	1493vw	C-H ds
		C-H ds		1455sh	C-H ds
				1449s	C-H ds
				1403m	
1357	N-H du		1320 ^a	1361s	N-H d
				1311w	C-H twist
				1295m	ov. 489+807
		N-H d	1250 ^a	1203s	C-H d
					N-H twist
1189	B-H ds	B-H d	1200 ^a	1187s	B-H d
1155	B-H du	B-H d		1171s	B-H d
		B-H d	1135 ^a	1125vw	B-H d
				1091s	C-C str.
1065	NBH r				
		C-N str.	1030 ^a	1059s	C-N str.
		B-H r	925 ^a	937w	$\gamma\text{-NH}_2$, vRing [7]
		-		893m	
				807m	$\gamma\text{-NH}_2$, vRing [7]
			755 ^a	755vw	pCH ₂ [7]
800	¹⁰ B-N str.			721w	¹⁰ B-N str.
784	¹¹ B-N str.	B-N str.	695 ^a	701m	¹¹ B-N str.
727	NBH r	N-H r			
		-		605vw	
				489vw	Lattice modes
				385m	
				197vw	
				141s	
				117vw	

^a: data obtained from reported spectra figures (with an uncertainty of about 15 cm^{-1})

5.3.2 Hydrogen desorption properties of EDAB

Simultaneous DTA-TGA-MS measurements of EDAB recorded at a constant heating rate of 1 $^\circ\text{C}\cdot\text{min}^{-1}$ under Ar flow are presented in Figure 5.4. The DTA signal (Figure 5.4.b) exhibits two exothermic events with maxima at 121 $^\circ\text{C}$ and 171 $^\circ\text{C}$, respectively. These exothermic processes are accompanied by two H_2 desorption peaks detected by MS (Figure 5.4.a), in accordance with previous results [4]. Integration of MS and DTA signals

(after subtracting the corresponding baselines) allows the calculation the H₂ desorption yields as well as the enthalpies of each desorption step. Mean values and standard deviations obtained from six measurements at different heating rates (ranging from 0.5 to 5 °C·min⁻¹) are given in Table 5.2, together with the mass losses accompanying the desorption processes determined by TGA. The H₂ desorption yields are in agreement with previously reported values [4]. Apart from H₂, MS detects no other species in desorption experiments under flowing gas conditions, confirming what reported elsewhere [4]. The enthalpies for both hydrogen-desorption steps are also in good agreement with those previously reported for EDAB [4].

This implies that the stability of the prepared EDAB samples does not depend on the synthesis route used to prepare them. However, enthalpy values obtained in this work have a higher standard deviation than those previously reported, particularly for the second desorption step. Previous works on the thermolysis of polymeric aminoborane [15] and some related compounds [16,17] have reported an influence of the applied heating rate on the enthalpy of H₂ desorption, suggesting that several parallel reactions with different kinetics proceed simultaneously during their thermal decomposition, as already mentioned in chapter 3. Indeed, such compounds desorb other gases in addition to H₂ and their amounts would depend on the heating rate. According to our results, in line with previous reports [4], EDAB releases pure H₂ during its thermolysis at ambient pressure. Therefore, the observed scattering in desorption enthalpies cannot be ascribed to desorption of other gaseous species. Alternatively, it may be due to the dependence of the structural and chemical properties of the obtained polymeric product (such as exact stoichiometry, degree of branching, and degree of cyclization) on the applied heating rate. However, sample contamination with traces of residual gases during the TPD-DTA-TGA measurements can also play a role in the obtained enthalpy values, as will be discussed below. It is worth noting that the enthalpy of the second desorption step is less exothermic than that of the first step, as expected, indicating that the product of the first decomposition step is relatively more stable than EDAB similarly to what was observed during the decomposition of AB under a temperature ramp in chapter 3, the lower exothermicity of the second hydrogen release indicates that there is a more discrete increase of stability in the second step, which reversibility should be higher.

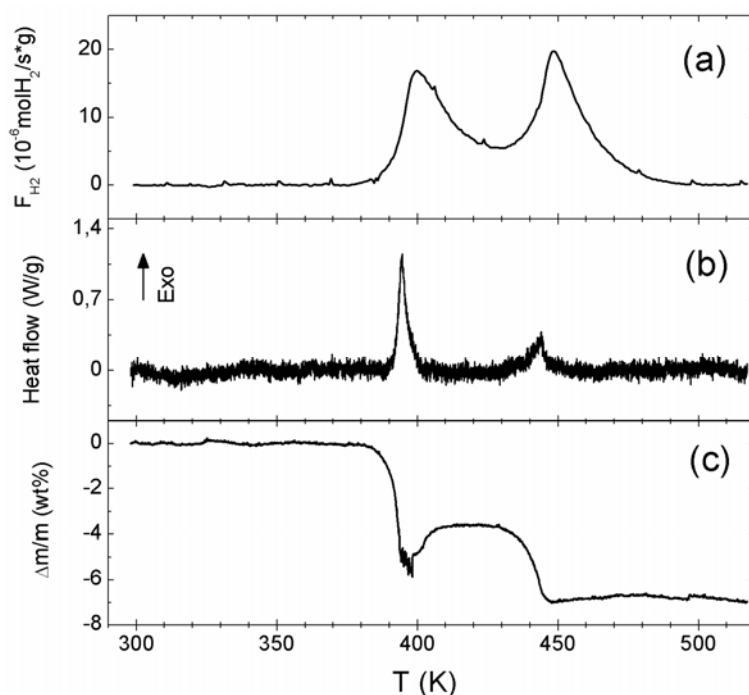


Figure 5.4: DTA-TGA-MS curves (baseline subtracted) of EDAB obtained under flowing Ar conditions at a heating rate of 1 K·min⁻¹. (a) H₂ desorbed flow obtained from the i₂ MS signal; (b) Heat flow recorded by the DTA apparatus; (c) relative mass loss calculated from the TGA signal

Table 5.2: Weight loss, H₂ desorption yields, enthalpies and activation energies for H₂ desorption from EDAB

Process	Weight loss (wt%)	Equivalents H ₂ (mol H ₂ ·mol EDAB ⁻¹)		ΔH (kJ·molEDAB ⁻¹)		E _{act} (kJ·molH ₂ ⁻¹)	
	This work	This work	Ref.[4]	This work	Ref.[4]	This work	Ref.[4]
Step 1	5.3±0.5	2.3±0.4	2.3±0.3	-26±4	-20.0±1.2	185±7	172
Step 2	4.1±0.5	2.3±0.4	~3	-9±3	-9.3±1.8	180±3	-

The TGA signal (Figure 5.4.c) clearly shows two mass loss events occurring concomitantly to DTA and MS peaks. The TGA signal of the first desorption process presents some fluctuations above 120 °C. This effect is tentatively ascribed to H₂ desorption from the liquid phase of EDAB (which melts at 119 °C [7]). H₂ desorption from the molten phase should account for the observed foaming; this foaming must generate the fluctuations in the mass signal. An increase in the mass signal recorded by TGA is observed after the first desorption event. A similar effect was observed in AB, which showed a mass increase following H₂ desorption due to sample contamination with residual atmospheric gases [18]. Therefore, the observed mass increases after the first H₂ evolution step in Figure 5.4.c has been ascribed to sample contamination with residual gases (O₂, H₂O) in the DTA chamber. This effect can be also responsible for the observed scattering in the enthalpy values, in particular for the second desorption step. In any case, it seems that sample contamination does not exert a

dramatic influence on the H₂ desorption yields and desorption enthalpies, since such values possess relatively good reproducibility and are consistent with previously reported ones. The amount of H₂ desorbed at each desorption step are also in good agreement with the mass losses determined by TGA. This observation supports the conclusion that EDAB desorbs only pure hydrogen, at least within the detection limits of our experimental apparatus and our temperature interval. This implies that EDAB presents improved characteristics with respect to its parent AB compound, which releases small quantities of gaseous poisons such as borazine or diborane during its thermal decomposition under flowing inert gas conditions as already mentioned [19].

The influence of pressure conditions on the thermolysis of EDAB has been investigated by performing additional DTA-TGA-MS measurements under dynamic vacuum. In such experiments, DTA signals are not reliable because of the poor thermal conductivity between the sample and the heat detector under vacuum conditions. Therefore, Figure 5.5 shows only TPD-MS and TGA data. As a general trend, H₂ desorption occurs at lower temperatures in vacuum than at ambient pressure and exhibits maxima at 107 °C and 155 °C when heating at 1 °C·min⁻¹. The decomposition behavior of EDAB under vacuum presents some other differences with respect to flowing gas conditions. The TGA curve shows a mass decrease well below the onset of H₂ desorption. The MS spectra profiles of the gases evolved below 77 °C are very similar to that of *n*-hexane, a molecule isoelectronic to EDAB as shown in Figure 5.6. This suggests that EDAB molecules would sublime under vacuum before H₂ desorption starts. However, EDAB sublimation competes with its thermolysis and is suppressed with increasing temperature due to EDAB decomposition. This aspect will be further discussed below. Besides, there are a number of mass spectrometric signals presenting peaks at the same temperature ranges than the two first H₂ desorption peaks. The observed *m/q* values, together with the presumed species being desorbed according to these MS signals are listed in Table 5.3. Residual THF signal in the samples is apparent during the first H₂ desorption peak, whereas diborane desorbs concomitantly to the two first H₂ desorption peaks. In addition, there are some unassigned *m/q* signals during both desorption steps that are tentatively ascribed to volatile B-N-C-H species. Finally, a weak H₂ desorption peak is observed above 197 °C, which is not present in the desorption experiments under Ar flow.

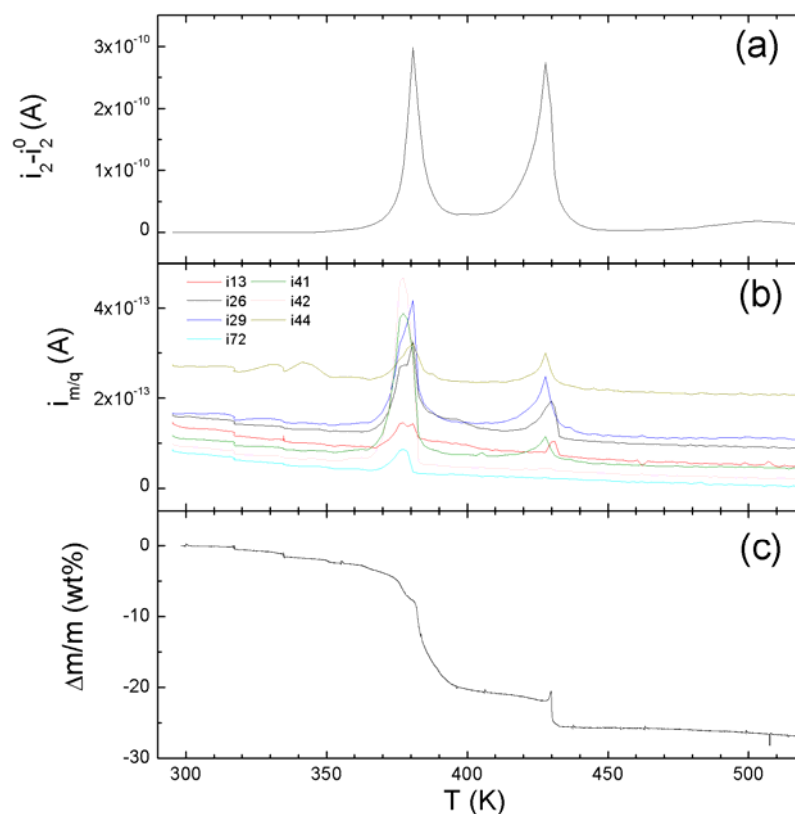


Figure 5.5: TPD-MS-TGA measurement obtained under dynamic vacuum conditions at a heating rate of $1\text{ }^{\circ}\text{C}\cdot\text{min}^{-1}$. (a) i_2 mass spectrometric signal corresponding to the H_2 desorbed flow; (b) several mass spectrometric signals ($i_{m/q}$) characteristic of diborane, THF and volatile B-C-N-H species; (c) relative mass loss calculated from the TGA signal

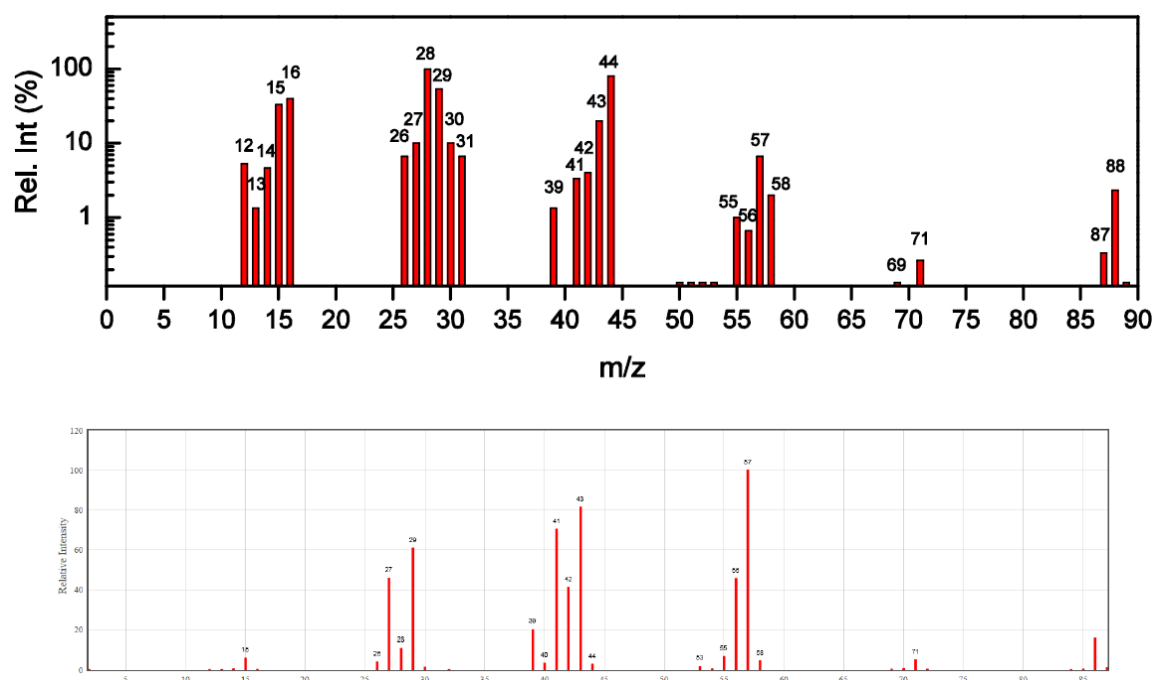


Figure 5.6: Mass spectra of the gases evolved from EDAB under vacuum TPD-MS experiments below $80\text{ }^{\circ}\text{C}$ (top) and n-hexane (bottom, according to NIST database: <http://webbook.nist.gov/chemistry>)

Table 5.3: Mass spectrometric peaks identified in the vacuum thermolysis experiments of EDAB

Temperature range (°C)	m/q signals	Presumable Species	
50-90	12, 13, 14, 15, 16, 26, 27, 28, 29, 30, 31, 39, 41, 42, 43, 44, 55, 56, 57, 58, 69, 71, 87, 88	EDAB	
90-120	2	H ₂	Volatile B-C-N-H species
	10, 11, 12, 13, 21, 22, 23, 24, 25, 26, 27	B ₂ H ₆	
	14, 15, 25, 26, 27, 28, 29, 30, 31, 32, 37, 38, 39, 40, 41, 42, 43, 44, 45, 71, 72	THF	
	20, 33, 36, 55, 56, 57		
150-160	2	H ₂	Volatile B-C-N-H species
	10, 11, 12, 13, 21, 22, 23, 24, 25, 26, 27	B ₂ H ₆	
	20, 28, 29, 30, 33, 41, 43, 44, 45, 55, 56, 57		
200-250	2	H ₂	

Our results indicate that there is a clear influence of pressure conditions on the yield of volatile species released during EDAB thermolysis. A similar phenomenon has also been observed in AB. In fact, whereas the thermolysis of AB at ambient pressure yields small amounts of monomeric aminoborane (H₂BNH₂), borazine (B₃N₃H₆) and diborane (B₂H₆) [20], pure H₂ is released when conducting AB thermolysis at high pressures [21]. According to these observations, the release of volatile species other than H₂ can be suppressed by increasing the applied pressure; the pressure necessary to suppress this desorption depends on the compound. This suggests that desorption of these volatile species is reversible and therefore must be an endothermic process, which is also in accordance with the observed dependence of desorption enthalpies with the applied heating rate in PAB [15]. The TGA curve shows that the final mass loss at 247 °C (*ca.* 27 wt.%) is higher than that expected from H₂ desorption. This is ascribed to the simultaneous evolution of other species in addition to H₂. However, it must be noticed that the observed mass loss is much lower than that of AB under similar conditions. In fact, AB sublimates under vacuum at much lower temperatures [22]. MeAB also presents a much higher mass loss when heated at 247 °C, even under flowing gas conditions, due to sublimation of MeAB molecules [2]. Therefore, the present results imply that EDAB exhibits much higher thermal stability than its parent compounds AB and MeAB, under both vacuum and flowing gas conditions.

5.3.3 Reaction mechanism for the thermolysis of EDAB

The pathway for the thermolytic decomposition of EDAB has been investigated by ¹¹B NMR by Neiner *et al.* [4]. This technique gives information on the boron environments in the obtained decomposition products after the first and second H₂ loss. According to that characterization, only a broad resonance at $\delta = -20$ ppm is observed at room temperature, which is due to sp³ BH₃ groups in EDAB. During the first loss of H₂, a sharp resonance appears at $\delta = -39$ ppm, which is characteristic of BH₄⁻ groups. This is followed by the emergence

of additional resonances at $\delta = -5$ ppm and $\delta = -18$ ppm, suggesting the presence of sp^3 BH and BH_3 groups in a different environment. Finally, the samples obtained after the second loss of hydrogen present two broad resonances at $\delta = +24$ ppm and $\delta = -15$ ppm, which were ascribed to trigonal boron (sp^2) and sp^3 BH_2 groups.

In order to further elucidate the thermolytic decomposition pathway of EDAB, *operando* Raman-MS measurements have been performed. These measurements are complementary to the previous NMR characterization and deliver molecular information on the chemical bonds in B-H, N-H, C-H, B-N, C-N and C-C groups. *Operando* Raman-MS results are shown in Figure 5.7. The initial changes which become evident in the Raman spectra on increasing the temperature are the disappearances of the lattice modes at 140 and 386 cm^{-1} , as well as the B-N stretching band at 701 cm^{-1} , which start losing intensity at around 77 °C until disappearing at 117 °C. These changes are accompanied by the emergence of a novel lattice mode at 424 cm^{-1} as well as a broad band around 790 cm^{-1} . All these features are indicative of chain formation through polymerization of EDAB molecules. A decrease in intensity and a broadening of the N-H deformations and B-H deformation and stretching modes is concomitant to the first loss of H_2 ; this must be related to H_2 elimination. Unfortunately, Raman spectra are highly noisy above 3100 cm^{-1} due to the characteristics of the CCD detectors, hampering the Raman analysis of the N-H stretching modes. The emergence of a new band at 1204 cm^{-1} , related to cyclic BH_2 groups, is apparent during the second H_2 desorption step. The broad band at 784 cm^{-1} gradually loses intensity and a new band develops at 1334 cm^{-1} , due to B=N bond formation. In addition, there are two new bands in the B-H stretching region, at 2494 and 2582 cm^{-1} , indicating the presence of H bonded to sp^2 boron. It is also interesting to note that the bands corresponding to C-H deformation and stretching modes remain in the spectra. Only a temperature-induced broadening is apparent. This result indicates that C-H groups are not essentially modified during EDAB thermolysis at moderate temperatures (below 197 °C). In fact much higher temperatures would be needed in order to eliminate H atoms from C-H groups.

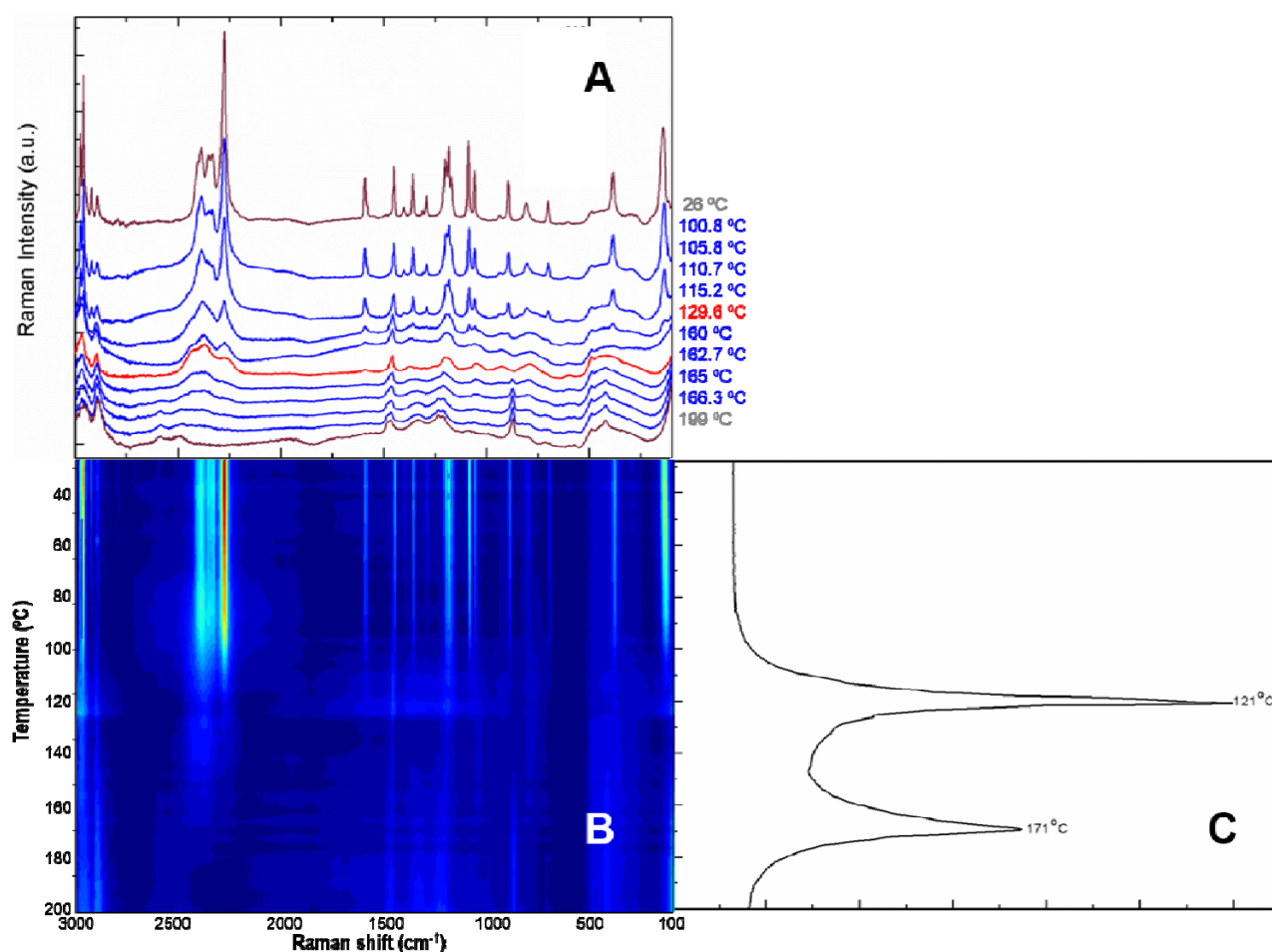
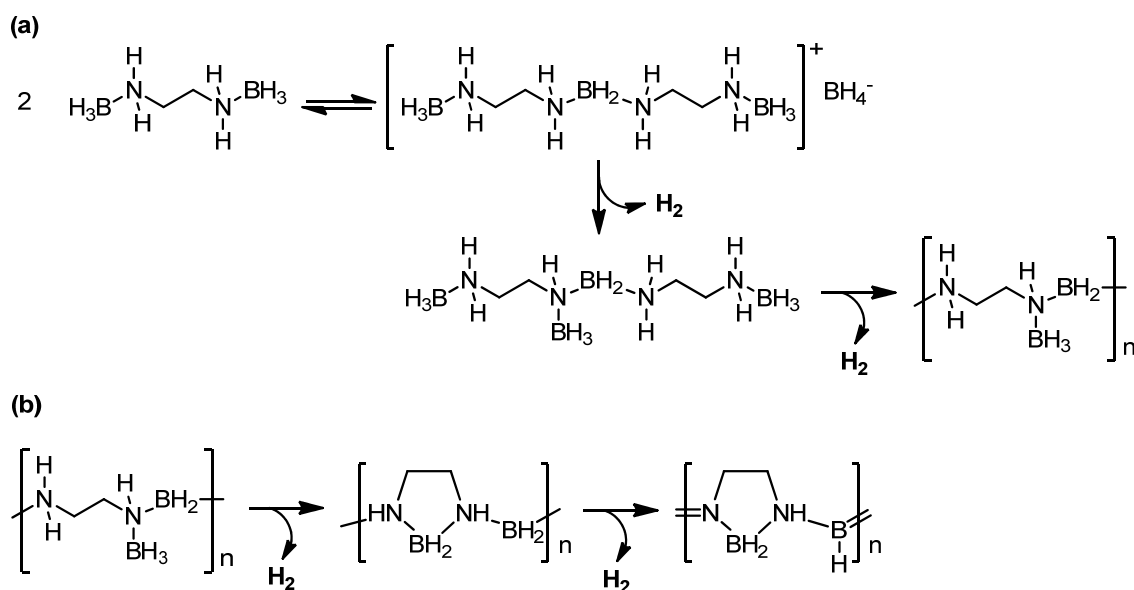


Figure 5.7: Representative Raman spectra (A), Raman intensity contour vs temperature (B) and simultaneous MS profile for H₂ (C) acquired during thermal decomposition of EDAB under a ramp of 1 K·min⁻¹

5.4. Discussion

On the basis of the *operando* Raman-MS measurements and previous ¹¹B NMR characterization of the reaction products [4], a reaction mechanism for the thermolysis of EDAB can be proposed, as shown in Scheme 5.1. This reaction mechanism presents slight differences with the one previously proposed [4]. In particular, the present reaction scheme differs in the number of H atoms present in some B and N groups. According to the proposed reaction mechanism, the first H₂ desorption process is due to an initial dimerization of EDAB molecules, which subsequently polymerize forming larger chains. This polymerization process may be related to the appearance of early Raman changes in the B-N stretching zone prior to any other intensity or Raman shift modification during *operando* Raman-MS, similarly to what was observed during AB decomposition. Then, a second H₂ desorption event is observed due to H₂ elimination from the formation of BH₂ cyclic groups and double B=N bonds as temperature increases. The proposed reaction mechanism may explain the exothermicity of H₂ desorption in EDAB, which is related to the formation of stable B-N bonds upon H₂ release to yield polymeric-like products.



Scheme 5.1: Proposed reaction mechanism for the first (a) and second (b) hydrogen desorption steps observed during the thermolysis of EDAB below 200 °C

According to what previously reported on EDAB thermal decomposition to deliver H₂, a higher exothermicity would be expected for the decomposition of the product obtained after the first H₂ release reaction compared to PAB. But these compounds decomposition reactions depict very similar enthalpy values when run under 1 °C·min⁻¹ temperature ramp as, apparently the ethylene bridge could destabilize the product from the first EDAB decomposition reaction by decreasing the ability to form di-hydrogen bonds, thus favoring the second H₂ release reaction.

The dependence of EDAB thermal stability on the ramp temperature under gas flow conditions seems to point out other physical processes take place simultaneously to the first decomposition reaction at 121 °C as already mentioned. EDAB is known to melt around 119 °C under ambient pressure and melting apparently has an effect on H₂ release and foaming; it is then possible that the dependence on the ramp temperature relies on the appearance of melting before, simultaneously or after the first decomposition reaction. Therefore, it may then be possible to separate EDAB melting and decomposition under certain ramp temperatures as was the case for AB [15]. Again, melting seems to be a key factor in the thermal behavior and H₂ release.

Finally, with respect to the activation energies the previously reported value for the first desorption step was 172 kJ·mol⁻¹, based on the analysis of the isothermal desorption kinetics at various temperatures [4]. As far as we know, no data have been reported for the second step. Here, we have obtained the activation energies for both H₂ desorption stages following the Kissinger method [23,24], which uses the H₂ release maxima of the DTA curves at different heating rates (ranging from 0.5 to 5 °C·min⁻¹). These Kissinger plots are shown in Figure 5.8 while the thus calculated activation energies are listed in Table 5.2. The activation energy for the first H₂ desorption peak is in reasonable agreement with the previously reported value [4]. Actually, our results

indicate that both desorption steps have similar activation energies. According to the proposed reaction mechanism, EDAB thermolysis kinetics are governed by the formation of novel bonds between B and N atoms; thus, exhibiting similar activation energy values for either desorption step.

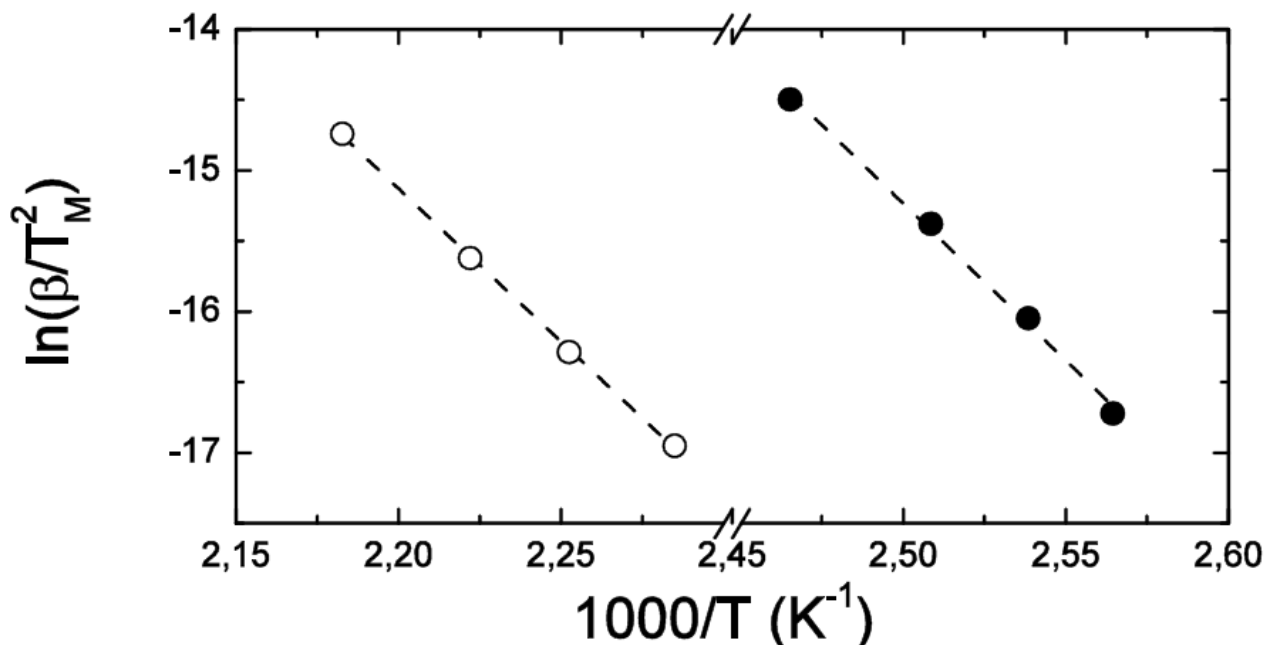


Figure 5.8: Kissinger plots of the first (full symbols) and second (open symbols) hydrogen desorption steps in EDAB under flowing Ar atmosphere

EDAB was demonstrated to have larger temperature dependence than AB for the rate of H₂ release which implies its higher stability at relatively high storage temperatures and a more rapid H₂ release at lower temperatures [4]. These are both highly desirable features besides the absence of impurities in the released H₂ compared to AB decomposition described in previous chapters, in particular the no detection of borazine, ammonia, aminoborane or diborane.

5.5. Conclusions

Ethane 1,2-di-amineborane (EDAB) samples have been successfully synthesized by reacting ethylenediamine dihydrochloride with sodium borohydride in tetrahydrofuran solution following a synthesis route reported in the early works on this compound. Structural and bonding properties of the samples have been characterized by means of XRD, NMR and Raman spectroscopy, confirming that the obtained EDAB samples are phase pure. The thermolysis of EDAB has been investigated by calorimetric and vibrational spectroscopic methods. Combined DTA-TGA-MS measurements allow the determination of H₂ desorption yields and enthalpies under flowing inert gas conditions. The obtained values are in agreement with those previously reported for EDAB samples prepared using a different synthetic route. EDAB thermolysis has been also investigated under

dynamic vacuum conditions. In this case, concomitant desorption of THF, diborane and some unidentified volatile compounds (presumably B-N-C-H molecules) is observed in addition to H₂. In either case, EDAB samples exhibit thermal stability higher than that of their parent counterparts, ammonia borane and methylamine borane with purer release of H₂.

Finally, the *operando* Raman-MS and NMR studies of the thermolytic decomposition of EDAB defines the bonding properties of the reaction products and propose a reaction scheme for the thermolysis of EDAB.

References

- [1] Xiong Z.; Yong C.K.; Wu G.; Chen P.; Shaw W.; Karkamkar A.; Autrey T.; Jones M.O.; Johnson S.R.; Edwards P.P.; David W.I.F., *Nat. Mater.* **7** (2008) 138-141
- [2] Bowden M.E.; Brown I.W.M.; Gainsford G.J.; Wong H., *Inorg. Chim. Acta* **361** (2008) 2147-2153
- [3] Groshens T.J.; Hollins R.A., *Chem. Commun.* (Cambridge, U.K.) (2009) 3089-3091
- [4] Neiner D.; Karkamkar A.; Bowden M.; Choi Y.J.; Luedtke A.; Holladay J.; Fisher A.; Szymczak N.; Autrey T., *Energy Environ. Sci.* **4** (2011) 4187-4193
- [5] Sahler S.; Konnerth H.; Knoblauch N.; Precht M.H.G., *Int. J. Hydrogen Energy* **38** (2013) 3283-3290
- [6] Kelly H.C.; Edwards J.O., *J. Am. Chem. Soc.* **82** (1960) 4842-4846
- [7] Goubeau J.; Schneider H., *Chem. Ber.* **94** (1961) 816-821
- [8] Kelly H.C.; Edwards J.O., *Inorg. Chem.* **2** (1963) 226-227
- [9] Bañares M.A., *Catal. Today* **100** (2005) 71-77
- [10] Rodríguez Carvajal J., *Phys. B: Condensed Matter* **192** (1993) 55-69
- [11] FullProf program can be downloaded at: <https://www.ill.eu/sites/fullprof/>
- [12] Ting H.-Y.; Watson W.H.; Kelly H.C. *Inorg. Chem.* **11** (1972) 374-377
- [13] Hess N.J.; Bowden M.E.; Parvanov V.M.; Mundy C.; Kathmann S.M.; Schenter G.K.; Autrey T., *J. Chem. Phys.* **128** (2008) 034508
- [14] Yang Z.; Cheng F.; Tao Z.; Liang J.; Chen, J., *Int. J. Hydrogen Energy* **37** (2012) 7638-7644
- [15] Baumann J.; Baitalow F.; Wolf G., *Thermochim. Acta* **430** (2005) 9-14
- [16] Yang Y.; Liu Y.; Li Y.; Gao M.; Pan H., *J. Phys. Chem. C* **117** (2013) 16326-16335
- [17] Wang P., *Dalton Trans.* **41** (2012) 4296-4302
- [18] Frueh S.; Kellett R.; Mallery C.; Molter T.; Willis W.S.; King'onde C.; Suib S.L., *Inorg. Chem.* **50** (2011) 783-792
- [19] Huang Z.; Autrey T., *Energy Environ. Sci.* **5** (2012) 9257-9268
- [20] Baitalow F.; Baumann J.; Wolf G.; Jaenicke-Rößler K.; Leitner G., *Thermochim. Acta* **391** (2002) 159-168
- [21] Baitalow F.; Wolf G.; Grolier J.-P.E.; Dan F.; Randzio S.L., *Thermochim. Acta* **445** (2006) 121-125
- [22] Palumbo O.; Paolone A.; Rispoli P.; Cantelli R.; Autrey T. *J. Power Sources* **195** (2010) 1615-1618
- [23] Kissinger H.E., *J. Res. Natl. Bur. Stand. (U.S.)* **57** (1956) 217-221
- [24] Kissinger H.E., *Anal. Chem.* **29** (1957) 1702-1706

Chapter 6

Ammonia Borane dehydrogenation enhancement in ionic liquids

Summary

Ammonia borane is a promising hydrogen storage material that liberates hydrogen by thermolysis at moderate temperatures. But ammonia borane also presents major limitations for practical applications including a long induction time before the initiation of hydrogen release and a difficult regeneration. Previous works have demonstrated that the induction period at the beginning of the thermolysis is eliminated by dissolving ammonia borane into several ionic liquids, and particularly in 1-butyl-3-methylimidazolium chloride bmimCl; some problems persist though, including foaming and the formation of a residue after thermolysis that is insoluble in the ionic liquid. In this chapter, the release of hydrogen from ammonia borane dissolved in different ionic liquids has been analyzed, measuring the kinetics of hydrogen release, visually following the evolution of the sample during the process using pressure glass tube reactors, and analyzing the residue by spectroscopic techniques. While dissolutions of ammonia borane in most ionic liquids analyzed show similar properties as dissolutions in bmimCl, using ionic liquids with bis(trifluoromethylsulfanyl) imide Tf₂N anion the foaming problem is reduced, and in some cases the residue remains dissolved in the ionic liquid, while with ionic liquids with choline cation higher hydrogen yields are achieved which indicate that the decomposition of ammonia borane proceeds through a different path.

6.1. Introduction

Previous chapters described dehydrogenation of AB when confined into porous material as an approach to destabilize it for improving its H₂ release properties. Since several of AB thermolysis limitations for its use as hydrogen storage material are related to the solid-gas nature of hydride decomposition reactions, a possible strategy to avoid them is to employ a dissolution instead of the solid compound. However, conventional volatile solvents cannot be used to this purpose, because the solvent would evaporate during the heating process required to decompose the hydrides, causing a contamination of the gaseous hydrogen that could damage fuel cells. Furthermore AB decomposition in organic solvent has been shown to favor the formation of cyclic products as cyclotriborazane or borazine, which is volatile, from diammonate of diborane (DADB) [1], the intermediate through which AB decomposition proceeds as reported in previous chapters, thus further contaminating the released H₂. In order to circumvent these problems, Bluhm et al. proposed to use ionic liquids as solvents [2]. Ionic liquids are substances entirely composed of ions, which are liquid near ambient temperature and offer very interesting properties that make them extremely useful in many chemical reactions. Ionic liquids can dissolve a wide range of compounds and offer a great chemical inertia as they provide an inert reaction medium which stabilizes polar transition states. This is important to promote the formation of oligomers of DADB like species with AB thus impeding the formation of cyclic products during AB decomposition [1]. Another of their most remarkable properties is their negligible vapor pressure [3] and so by using ionic liquids, the problem of hydrogen contamination by evaporation of the solvent would be avoided. Ionic liquids are stable to high temperature which allows operating at fuel cells working conditions and they offer the possibility of recycling with little loss of activity in general. They are often air and moisture stable though many are hygroscopic, needing drying before use in reactions. Some of the most common ionic liquids are composed of inorganic anions, X⁻, BF₄⁻, PF₆⁻, and nitrogen-containing organic cations, such as RN, R'⁺N-imidazolium or RN-pyridinium.

In their seminal work, Bluhm et al. observed a considerable enhancement of the kinetics of hydrogen release from ammonia borane dissolved in the ionic liquid 1-butyl-3-methylimidazolium chloride (bmimCl) with respect to solid ammonia borane [2]. In particular, the long induction period characteristic of hydrogen release from solid ammonia borane was not observed in the ionic liquid solutions. Based on this observation and on NMR analyses of reaction products, authors hypothesized that the ionic liquid participated in the decomposition reaction inducing the formation of diammoniate of diborane, $[(\text{NH}_3)_2\text{BH}_2^+]\text{BH}_4^-$ and BH₄⁻ ionic species. On a subsequent work, Himmelberger et al. [4] observed that the dehydrogenation rate enhancement

was still produced in mixtures of ammonia borane and bmimCl when the concentration of ionic liquid was reduced down to a 80:20 AB:ionic liquid ratio. These authors determined a decomposition mechanism based on the conversion of ammonia borane into the more reactive diammoniate of diborane ion, that was converted into polyaminoborane polymers and, finally, into polyborazylene, a mechanism that was not observed in the decomposition of AB from solutions in organic solvents such as tetraglyme (6). In this work, Himmelberber et al. [5] also tested other ionic liquids besides bmimCl, observing that the release of hydrogen was accelerated by dissolution in a variety of ionic liquids, especially during the release of the first hydrogen equivalent from ammonia borane. However, important differences were observed during the release of the second equivalent according to reaction (1) described in section 3.1: while some ionic liquids such as bmimCl or 1-butyl-3-methylimidazolium tetrafluoroborate (bmimBF₄) yielded over two hydrogen equivalents at 85 °C with accelerated rates, only one hydrogen equivalent was released from AB solutions in 1-propyl-2,3-dimethylimidazolium trifluoromethanesulfonate (pmmimTf₃C) at the same temperature. Basu et al. [5] also investigated the decomposition of ammonia borane in bmimCl and proved that the dissolution of the hydride in the ionic liquid not only increased the hydrogen release rate, but also the gravimetric yield, which was higher in 80:20 wt% mixtures of AB and ionic liquid than in neat AB when temperature was above 107 °C. They also observed that foaming, a problem in the utilization of ammonia borane for hydrogen storage, was partially suppressed by the addition of the ionic liquid. Wright et al [6] added ruthenium catalysts to AB solutions in bmimCl and 1-ethyl-3-methylimidazolium ethyl sulphate (emimESO₄), observing that this approach gave enhanced initial rates at low temperatures.

These previous studies have demonstrated the advantages of employing ammonia borane - ionic liquid mixtures, having tested a small range of different ionic liquids. The objective of this study is to explore the possibilities for using alternative ionic liquids as solvents for AB. With this purpose, the hydrogen release from AB dissolved in 13 ionic liquids has been systematically investigated. Results of hydrogen release rate and yield are reported, together with a characterization of the foaming and solubilization behavior of the solutions observed during hydrogen release experiments in high pressure glass tubes, and with a characterization of the reaction mixtures by FT-IR spectroscopy.

6.2 Experimental section

Dissolution of AB in the 13 ionic liquids detailed in section 2.1, which acronyms are given in Table 6.1 and that are represented in Figure 6.1 next were prepared and their thermal decomposition was investigated following the method summarized in section 2.2.9.

Table 6.1: Ionic liquids from Iolitec Ionic Liquids Technologies GmbH tested in this study

Name	Abbreviate name	Purity	M.P.
1-butyl-3-methylimidazolium chloride	bmimCl	99 %wt	~70 °C
1-allyl-3-methylimidazolium chloride	amimCl	98 %wt	~50 °C
1-(2-hydroxyethyl)-3-methylimidazolium chloride	HOemimCl	99 %wt	~95 °C
1-ethyl-3-methylimidazolium chloride	emimCl	98 %wt	77-79 °C
1-ethyl-3-methylimidazolium acetate	emimAc	95 %wt	> 30 °C
Tetrabutylphosphonium chloride	TbPhCl	95 %wt	80-83 °C
Choline dihydrogen phosphate	ChdHPh	95 %wt	~120 °C
Choline acetate	ChAc	98 %wt	80-85 °C
Choline bis(trifluoromethylsulfonyl)imide	ChTf ₂ N	99 %wt	30 °C
1-ethyl-3-methylimidazolium triflate	emimTfO	99 %wt	-13 °C
1-ethyl-3-methylimidazolium bis (trifluoromethylsulfonyl)imide	emimTf ₂ N	99 %wt	-9 °C
1-ethyl-3-methylimidazolium ethyl sulfate	emimESO ₄	99 %wt	< -30 °C
1-ethyl-3-methylpyridium bis(trifluoromethylsulfonyl)imide	empyTf ₂ N	99 %wt	15 °C

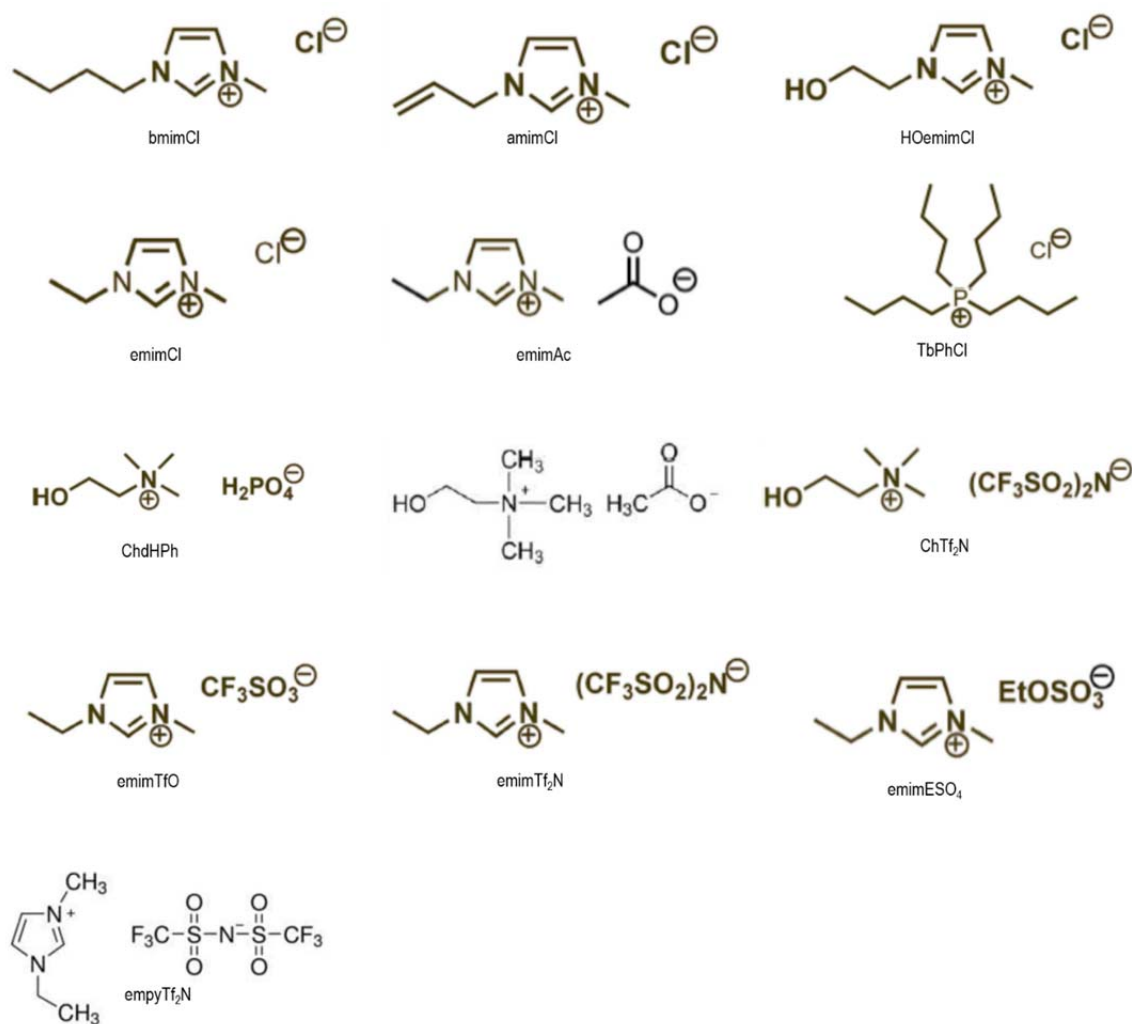


Figure 6.1: Ionic liquids from Iolitec Ionic Liquids Technologies GmbH tested in this study

6.3. Results

6.3.1 Thermolysis of solid ammonia borane

As a preliminary result, Figure 6.2 presents FT-IR spectra of neat AB and of the solid residue obtained after thermolysis of AB at 85 °C. The AB pattern shows peaks corresponding to N-H bonds at wave numbers near 3300 cm⁻¹, B-H bonds in the range 2000 – 2500 cm⁻¹, and B-N bonds at 1600 cm⁻¹ and 1350 cm⁻¹, in good agreement with literature data [7]. On the other hand, after thermolysis the peaks corresponding to B-H and N-H bonds appear attenuated in comparison with the large peaks formed near 1400 cm⁻¹ and 1120 cm⁻¹, which correspond to B-N bonds constituting the backbone of the polymeric polyaminoborane species formed by hydrogen release during AB thermolysis [8]. It can be observed that these peaks are broad, indicating the inhomogeneity of the product obtained after AB thermolysis, both in terms of the dispersion of the molecular weights of the polymeric species, and in terms of the variability of particle size and crystallinity.

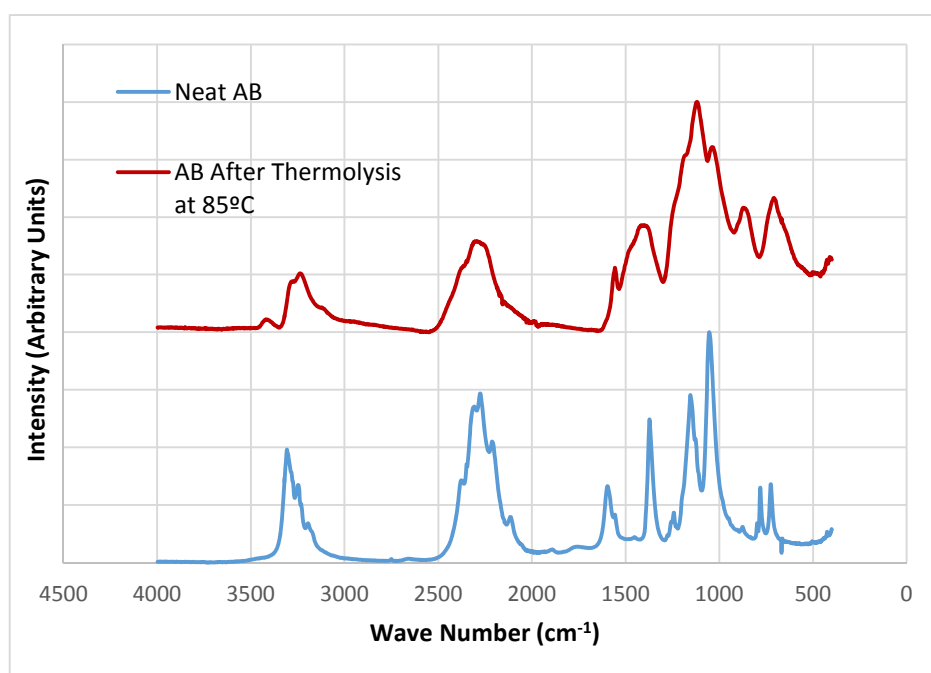


Figure 6.2: FT-IR spectroscopy patterns of neat AB and decomposition products after AB thermolysis

6.3.2 Release of hydrogen from ammonia borane dissolved in bmimCl

Figure 6.3 presents the release profile of hydrogen by thermolysis of ammonia borane from a 10 wt.% solution of AB in bmimCl at 85 °C. The results of two independent replications of the experiment are reported in this figure. It can be observed that the results of these two independent experiments were nearly identical, demonstrating the reproducibility of results.

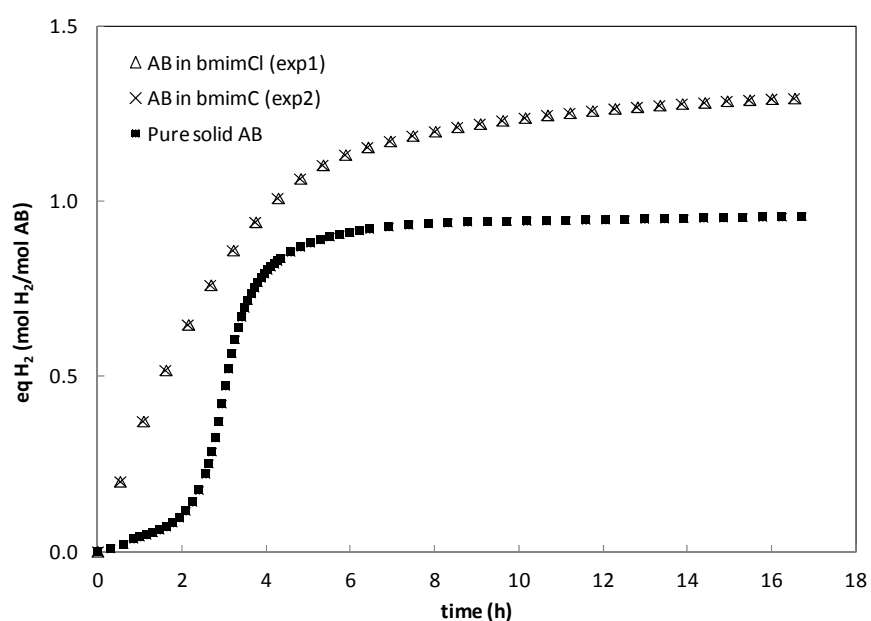


Figure 6.3: Hydrogen release rate for ammonia borane thermolysis at 85 °C from neat solid particles and from 10 wt% solutions of AB in the ionic liquid bmimCl

The hydrogen release curve from neat, solid ammonia borane is also presented in Figure 6.3. It can be seen that a long induction time of about 3 h is required to initiate the decomposition reaction, a well-known characteristic of the thermolysis of this compound that has been amply described in the literature [4,5,9]. The reaction is practically completed (95 % of final conversion) after 6 h, releasing almost one equivalent of H₂. This hydrogen yield, corresponding to the decomposition of AB to polyaminoborane according to the first step of reaction (1) from section 3.1, agrees with the yield expected at the temperature of 85 °C used in experiments [10,11].

In contrast, the release curves from AB solutions in the ionic liquid do not show any induction period, and the H₂ yield increases to 1.3 equivalents, reaching a 95 % of final conversion after 9.5 h. The increase of the hydrogen yield indicates a participation of the ionic liquid in the reaction mechanism, as observed by Bluhm et al. [2] and Himmelberger et al. [4]. FT-IR spectroscopy assays of the initial solution and the reaction products, shown in Figure 6.4, are also consistent with the reaction mechanism proposed by these authors. In the FT-IR pattern of the initial AB solution in bmimCl, characteristic peaks at wave numbers of 2300 - 2400 cm⁻¹ corresponding to symmetric and asymmetric B-H bond stretch [8] can be observed due to the presence of AB in this solution. It is important to note that N-H characteristic peaks observed for neat AB around 3300 cm⁻¹ are not detected for the AB/bmimCl dissolution. The B-H peaks also disappear after the AB decomposition reaction, and new peaks are observed at wavenumbers of 1400, 1300, 900 and 740 cm⁻¹ that, as presented in Figure 6.2, can correspond to B-N bond stretch of linear and cyclic polyaminoborane and B=N in polyborazylene [11,12], the main decomposition reaction products identified by Himmelberger et al. [4].

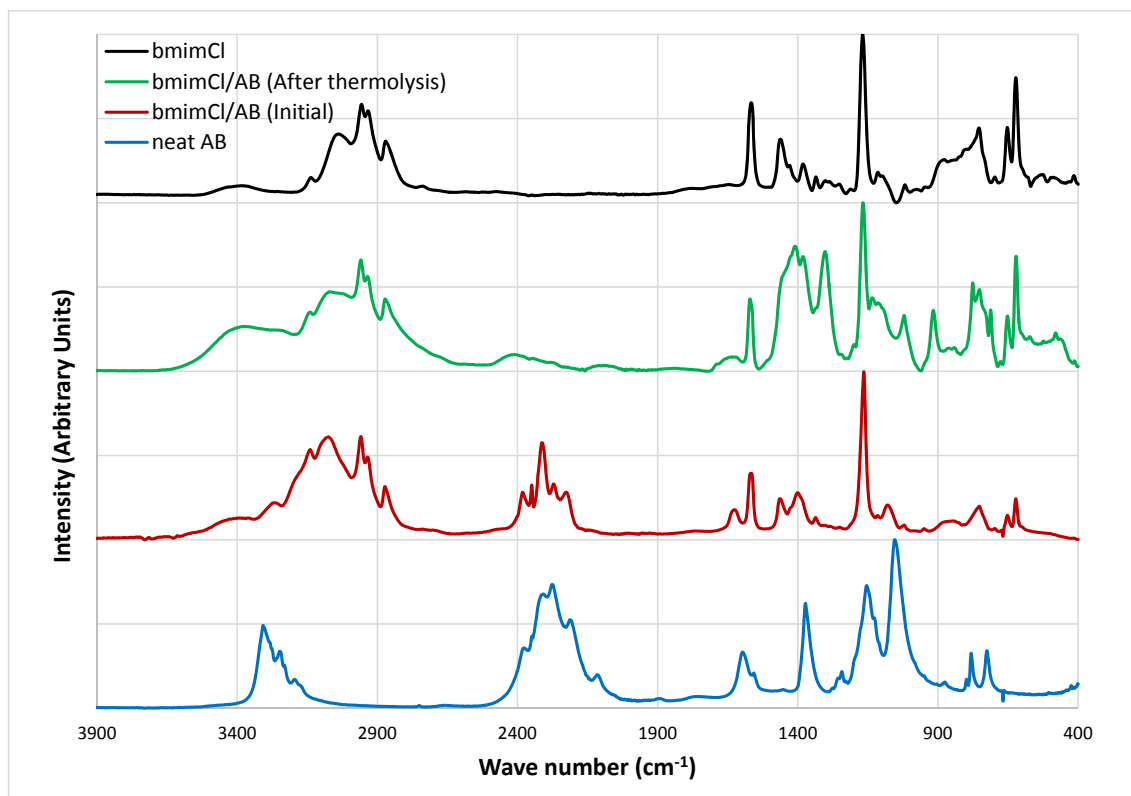


Figure 6.4: FT-IR spectroscopy patterns of pure AB, pure bmimCl ionic liquid, 10 wt% solution of AB in bmimCl, and 10 wt% solution of AB in bmimCl after thermolysis

Visually analyzing the reaction products, as presented in Figure 6.5, it can be seen that, after decomposition of neat AB, a solid foam was formed. In agreement with the observations of Basu et al. [5], by dehydrogenation of AB dissolved in bmimCl a similar foam was obtained that became solid even maintaining a temperature of 85 °C (above the melting temperature of the bmimCl ionic liquid that is, 60 °C), indicating that the reaction products were not soluble in this ionic liquid, which is a non-desired feature for the regeneration of this material. Therefore, by dissolution of AB in bmimCl, results indicate the suppression of the induction time in the decomposition reaction of AB, an enhanced yield of the reaction that advanced to the formation of polyborazylene even at a low temperature of 85 °C, with foaming after thermolysis, agreeing with the general conclusions reported in previous studies [2,5,6].

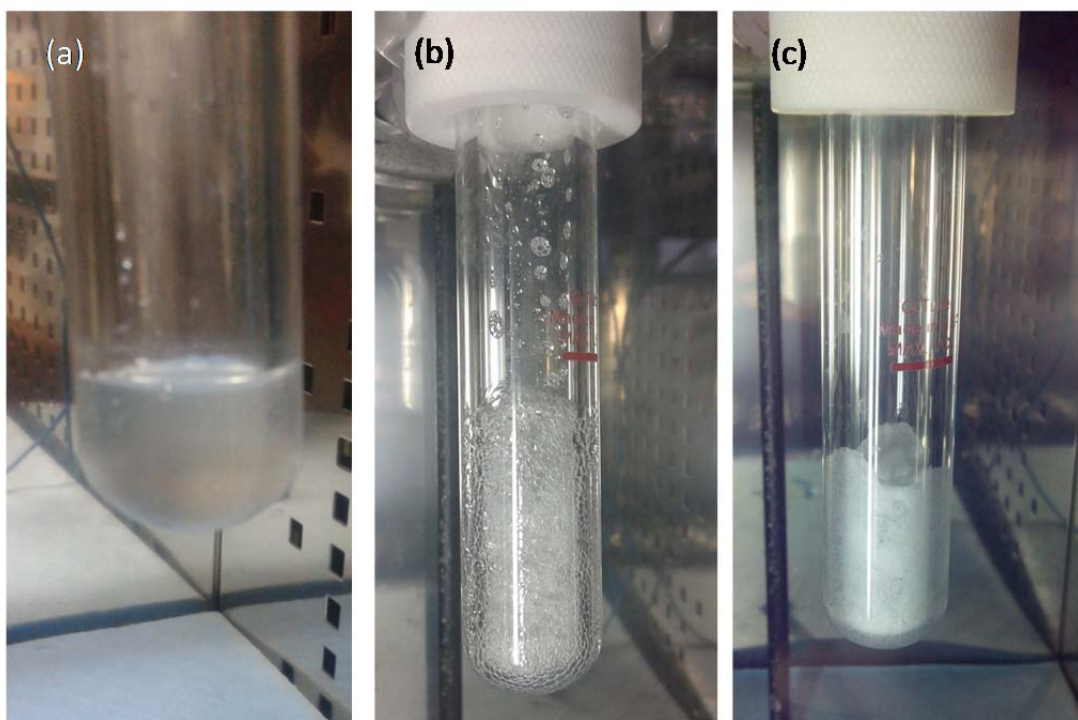


Figure 6.5: Photographs of samples: a) 10 wt% solution of AB in bmimCl before thermolysis. b) 10 wt% solution of AB in bmimCl after thermolysis. c) Neat AB after thermolysis

6.3.3 Release of hydrogen from ammonia borane dissolved in different ionic liquids

As previously indicated, the release of H_2 by thermolysis of AB dissolved in 13 different ionic liquids was investigated. Table 6.2 summarizes some of the main results obtained, while Figure 6.6 presents H_2 release curves of AB dissolutions in some selected ionic liquids.

Table 6.2: Thermolysis of AB in different ionic liquids, summary of results: H_2 released at equilibrium, time required to release 0.5 equivalents of H_2 , and time required to release 95 % of the amount of H_2 liberated at the equilibrium

Ionic liquid	H_2 release in equilibrium (H_2 equivalents)	t for 0.5 H_2 eq (h)	t for 95 % of equilibrium H_2 (h)
- (Neat AB)	0.96	3.2	6.0
bmimCl	1.30	1.5	9.5
amimCl	0.49	-	8.1
HOemimCl	1.54	0.5	10.8
emimCl	1.75	1.4	6.5
emimAc	0.70	3.0	4.0
TbPhCl	1.78	0.3	3.9
ChdHPh	1.28	1.1	4.0
ChAc	2.29	1.9	15.8
ChTf ₂ N	2.90	0.7	7.2

emimTfO	1.58	0.5	4.5
emimTf ₂ N	1.50	0.3	15.2
emimESO ₄	1.85	0.6	2.3
empyTf ₂ N	1.23	0.1	1.0

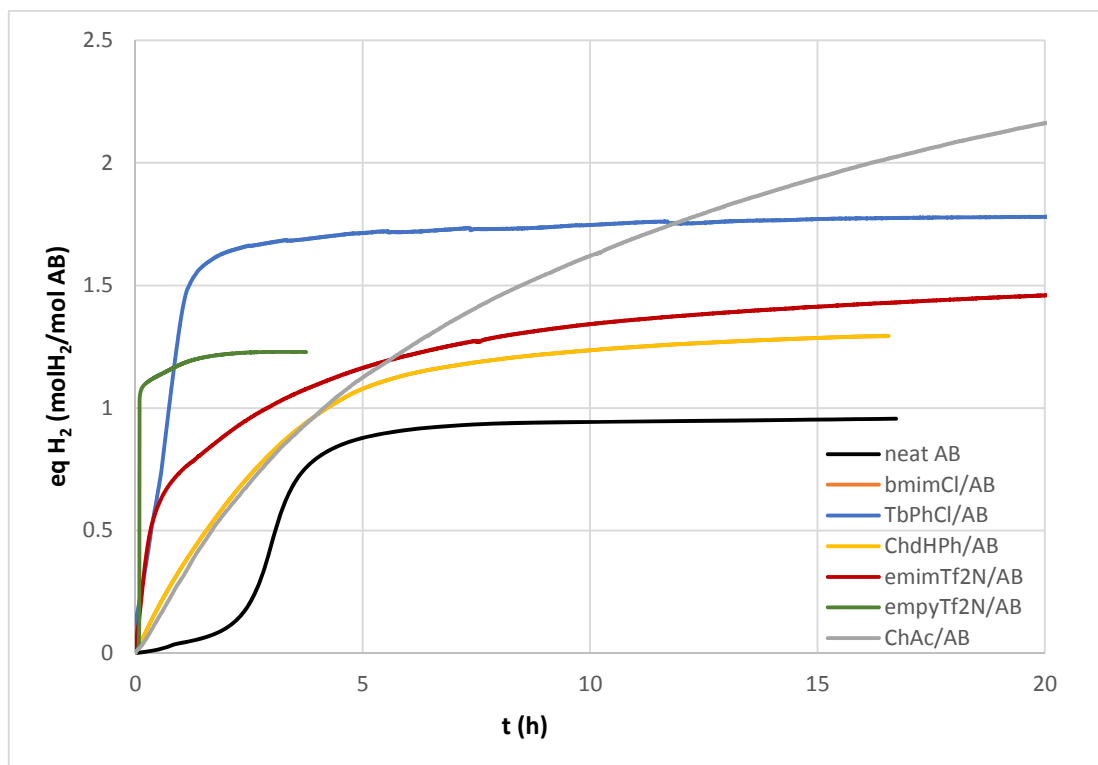


Figure 6.6: Hydrogen release rate for ammonia borane thermolysis at 85 °C from neat solid particles and from 10 wt% solutions of AB in different ionic liquids

From a qualitative point of view, the release curves in different ionic liquids share similar characteristics: a considerable reduction or suppression of the induction time, with an accelerated release of H₂ that in many cases allows reaching a higher yield than the release experiments from neat AB.

From a quantitative point of view, several ionic liquid/AB solutions tested also present similar characteristics to the bmimCl/AB solutions discussed in section 6.3.2, with a total H₂ yield in the range of 1.3- 1.5 equivalents, of which the first 0.5 equivalent is released in approximately 1 h. A typical example is the case of AB solutions in ChdHPh that release 0.5 H₂ equivalents after 1 h and 1.3 H₂ equivalents at equilibrium. As presented in Figure 6.7, in this case characteristic AB peaks in the low wave number range are clearly visible in the initial AB-IL solutions thanks to a lower superposition with IL characteristic peaks. After thermolysis, these peaks disappear and are replaced by broad peaks characteristic of B-N bonds, indicating that the mechanism of AB

decomposition in ChdHPh solutions proceeds through the formation of polyaminoborane/polyborazylene polymers, as in the case of bmimCl/AB solutions.

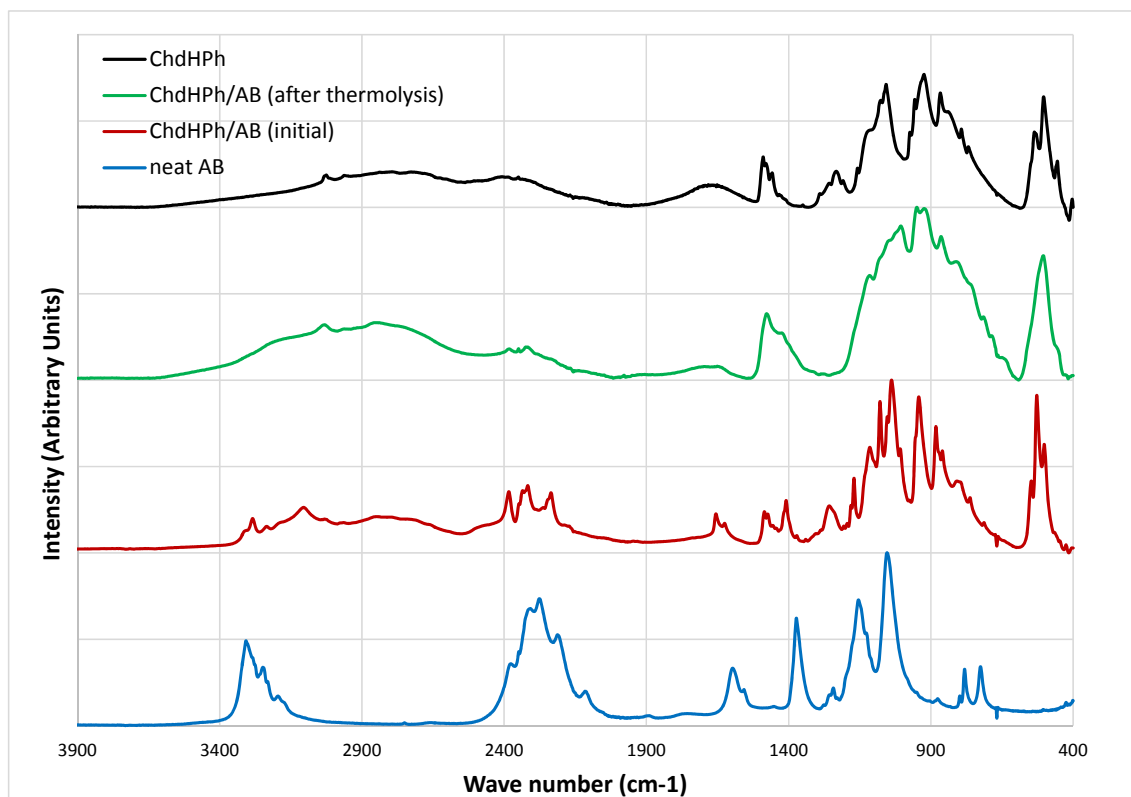


Figure 6.7: FT-IR spectroscopy patterns of pure AB, pure ChdHPh ionic liquid, 10 wt% solution of AB in ChdHPh, and 10 wt% solution of AB in ChdHPh after thermolysis

However, in some cases, important differences can be observed between the different ionic liquids. In particular, experiments with emimTf₂N ionic liquid show a considerable acceleration of the H₂ release, with 0.5 H₂ equivalents released in just 0.3 h, compared to the 1.5 h and 3.2 h needed to release the same H₂ amount from bmimCl solutions and neat AB. The final H₂ yield achieved is approximately 1.5 equivalents. This yield and the results of FT-IR assays, presented in Figure 6.8, are compatible with the same mechanism of partial conversion to polyborazylene reported for bmimCl-AB solutions. In these spectrograms, B-H characteristic peaks of AB in the range 2300 - 2400 cm⁻¹ can be observed in the initial AB-IL solution, although with a lower intensity than in the case of bmimCl-AB solutions. In the case of the solution after thermolysis, B-N peaks appear merged with IL characteristic peaks and are less noticeable than in the case of bmimCl-AB solutions, but still the broad peak near 1400 cm⁻¹ can be clearly observed, and smaller peaks near 900 and 740 cm⁻¹ are also noticeable. Another interesting characteristic of this ionic liquid is its lower hygroscopicity compared with most other ionic liquids tested,

manifested in FT-IR assays in the absence of a broad peak around 3000 cm^{-1} characteristic of OH groups and due to adsorbed humidity, which in contrast is clearly visible in the FT-IR assays of bmimCl ILs reported in Figure 6.4. Another interesting characteristic of ionic liquids with Tf_2N anion and short cation chains is its lower viscosity compared to other types of ionic liquids [13], which can facilitate the release of hydrogen gas bubbles with less foaming. Indeed, as shown in Figure 6.9, practically no foam is formed during the thermolysis experiment. However, as it can also be seen in Figure 6.9, the polymeric residue formed after thermolysis is insoluble in emim Tf_2N , which is an unfavorable characteristic for the regeneration of ammonia borane from this residue.

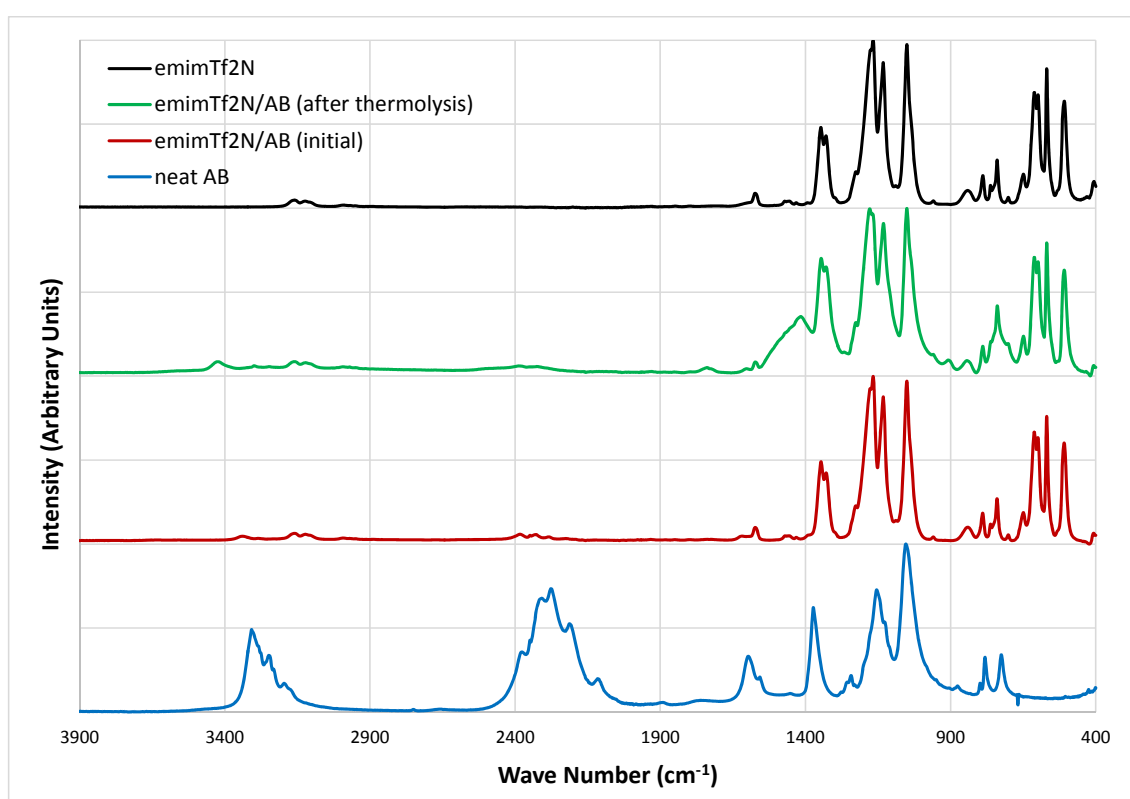


Figure 6.8: FT-IR spectroscopy patterns of pure AB, pure emim Tf_2N ionic liquid, 10 wt% solution of AB in emim Tf_2N , and 10 wt% solution of AB in emim Tf_2N after thermolysis

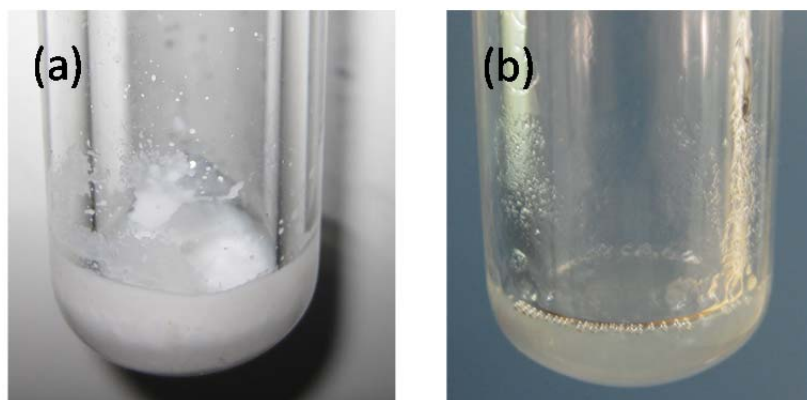


Figure 6.9: Photographs of samples: a) 10 wt% solution of AB in emimTf₂N after thermolysis. b) 10 wt% solution of AB in empyTf₂N after thermolysis

As reported in Table 6.2 and Figure 6.6, even more noticeable are the results obtained with another IL with Tf₂N anion: the empyTf₂N ionic liquid. In this case, the release of H₂ by thermolysis is drastically accelerated, and more than one H₂ equivalent is released in less than 0.5 h. As presented in Figure 6.10, the FT-IR spectra exhibit similar characteristics to the case of emimTf₂N/AB solutions presented in Figure 6.8: weak peaks near 2300 cm⁻¹ in the initial solution, corresponding to B-H bonds of the dissolved AB, that disappear after the thermolysis being replaced by a broad peak near 1400 cm⁻¹ and a small peak at 900 cm⁻¹. This result and the total H₂ yield of 1.5 equivalents indicate that in this case the decomposition also proceeded through the polyaminoborane/polyborazylene route. No foam is produced during H₂ release from solutions of empyTf₂N/AB, although naturally an important increase of the apparent volume can be observed during the periods of more intense H₂ bubbling. However, as it can be observed in Figure 6.9, in this case the polymeric compounds produced during AB thermolysis remain dissolved in the ionic liquid. This is a very unique property that, of all ionic liquids tested in this study, has only been observed in the case of empyTf₂N, and that to the best of authors' knowledge has not been reported for any of the different ionic liquids tested in previous works. This property is relevant because it can facilitate the regeneration of the spent AB and thus the reutilization of the solution over a number of hydrogen cycles, which could be performed in a homogeneous solution without addition of auxiliary solvents, whose removal after the regeneration could be costly and problematic.

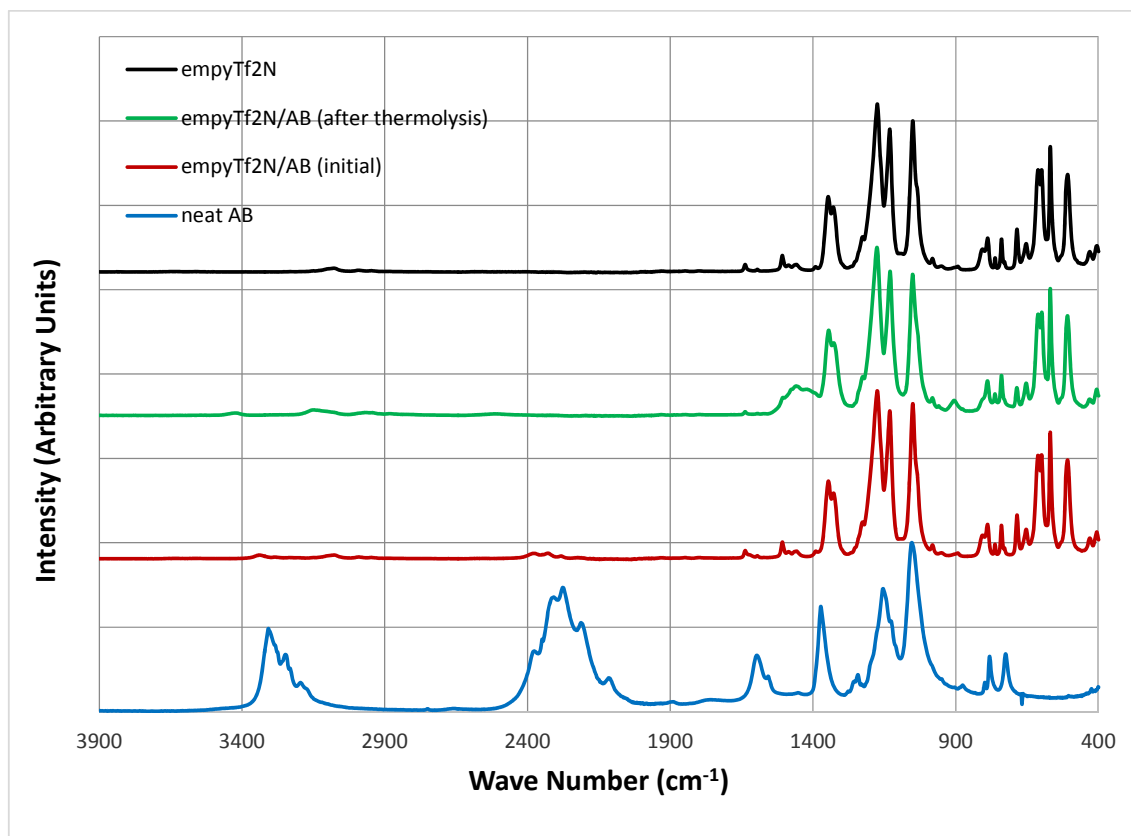


Figure 6.10: FT-IR spectroscopy patterns of pure AB, pure emptyTf₂N ionic liquid, 10 wt% solution of AB in emptyTf₂N, and 10 wt% solution of AB in emptyTf₂N after thermolysis

Another prominent group of results reported in Table 6.2 and Figure 6.6 are the cases where very high H₂ yields are obtained, above 2 H₂ equivalents. This is the case of ChAc-AB or ChTf₂N-AB solutions. As presented in Figure 6.11, in this case FT-IR assays also yield different results: after thermolysis, a group of well-defined peaks in the range 2400 – 2200 cm⁻¹ is observed, which is characteristic of B-H bonds, but differs from the B-H bond peaks observed in this range in the AB spectrum. This result suggests that, in this case the thermolysis of AB proceeded through the alternative route of dehydropolymerization to borazine and formation of cyclotriborazane (H₂BNH₂)₃ [1,14], as the latter compound may be responsible for the B-H peaks observed in the FT-IR spectrogram after thermolysis. This reaction path releases a higher number of H₂ equivalents than the polymeric ammonia-borane cycle observed with the other ionic liquids, but it is hindered by a more difficult regeneration of AB from these reaction products [15], and by the concomitant release of gaseous borazine, which is toxic and can damage fuel cells as already reported in previous chapters.

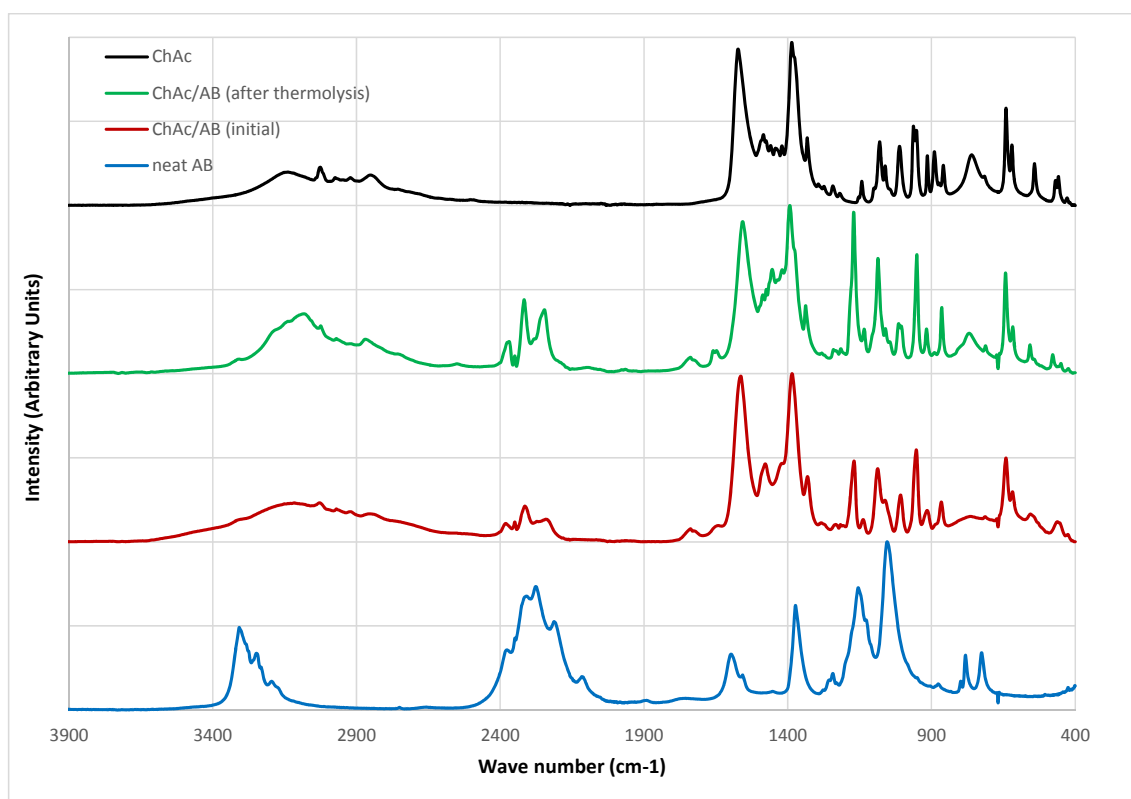


Figure 6.11: FT-IR spectroscopy patterns of pure AB, pure ChAc ionic liquid, 10 wt% solution of AB in ChAc, and 10 wt% solution of AB in ChAc after thermolysis

6.4. Discussion

The main ionic liquid used up to now to study possible improvement of AB decomposition has been 1-butyl-3-methylimidazolium chloride (bmimCl) as it initially showed good activity and is inexpensive and easy to handle. Some of the ionic liquids studied in this chapter have shown similar effects on AB dehydrogenation in terms of H₂ release rate and suppression of the initial induction period and in terms of H₂ yield. But some other ionic liquids-AB mixtures showed a quite different behavior regarding H₂ release rate and yield. The melting point of bmimCl is above room temperature as shown in Table 6.1 but once molten it remains in metastable liquid form at lower temperatures and forms a stirrable liquid at room temperature when mixed with AB. It was reported in the pioneering work of Himmelberger et al. [4] that when studying AB/bmimCl mixture, H₂ release began immediately after the solution melted and it was observed for AB/ionic liquid mixtures in general that H₂ release was not observed until the ionic-liquid/AB mixture melted. This is in consonance with what was already reported for thermally-induced AB H₂ release reactions in the solid state in chapter 3 as results there detailed suggested that AB dehydrogenation may be favored in the melted phase in general. Thus, the differences in terms of H₂ release rate observed from some ionic liquids AB dissolutions with respect to bmimCl/AB mixtures may be due to the

temperature needed for such dissolutions to melt. The mixtures needing smaller temperatures for melting than bmimCl/AB would then give rise to higher H₂ release rate.

As described in previous chapters for the solid-state H₂ release reactions, initial formation of DADB has also been proposed as the key step in thermally-induced AB H₂ release reactions in ionic liquids and organic solvents. But in previous ¹¹B NMR and H₂ release studies on AB decomposition in ionic liquids, it was shown how the highly polar medium provided by ionic liquids promotes DADB formation and appears to be the key activating feature of these ionic liquid reactions [2,4]. The results obtained by combining solid-state and solution ¹¹B NMR studies of AB/ionic-liquid and DADB/ionic-liquid supported an AB dehydrogenation pathway in ionic liquids involving: (1) ionic-liquid promoted conversion of AB into its more reactive ionic DADB form, (2) further intermolecular dehydrocoupling reactions between hydridic B-H hydrogens and protonic N-H hydrogens on DADB and/or AB to form polyaminoborane polymers and (3) polyaminoborane dehydrogenation to unsaturated cross-linked polyborazylene materials. This mechanism would be quite similar to that described for solid-state H₂ release reactions (see section 3.4) but precluding the induction period during which AB gives rise to a more mobile ammonia borane species AB* according to what reported by Shaw et al. [16]. By increasing the speed of formation of DADB, ionic liquids dramatically improve the H₂ release rate from AB and this phenomenon seems common to many of the ionic liquids tested in this study and many others [2,4]. As previously mentioned, ionic liquids exhibit the ability to provide an inert reaction medium which stabilizes polar transition states and would be expected to promote the formation of oligomers of DADB like species with AB thus impeding the formation of cyclic products from DADB as would happen in organic solvents [1]. But it has been shown in previous works and in this study how some ionic liquids favor the cyclic products-route instead of the mechanism based on oligomerization of PAB [4] thus giving rise to significant differences in terms of H₂ yield as already reported in section 6.3.3 regarding dehydrogenation of ChAc/AB and ChTf₂N/AB. Thermal decomposition of these AB dissolutions produced significantly higher H₂ yields compared to the rest of AB/ionic liquids which is detrimental considering that the main product through such decomposition is borazine which is poisonous for the fuel cell and that the cyclic products hinder residue regeneration to AB as mentioned earlier.

6.5 Conclusions

The release of hydrogen by thermolysis of AB dissolved in 13 different ionic liquids has been analyzed. In most cases, the results observed are similar to those obtained in the study of

ammonia borane solutions in bmimCl ionic liquids and reported in previous works: a drastic reduction of the induction time and a slight increase of the hydrogen yield, but with foaming problems and formation of a solid residue, insoluble in the ionic liquid, at the end of the thermolysis. The results obtained with some ionic liquids with bis(trifluoromethylsulfanyl) imide anion (emimTf₂N and empyTf₂N) are more promising, as dissolutions of ammonia borane in these ionic liquids do not form foams during thermolysis, probably due to the relatively lower viscosity of these ionic liquids, and show the greatest enhancement in hydrogen release kinetics. Indeed, using solutions in those ionic liquids, the time needed to release 0.5 equivalent of hydrogen at 85 °C is in the range of 5–15 min, compared to more than 3 h needed to obtain the same amount of hydrogen from neat AB. Moreover, in the case of empyTf₂N dissolution, the residue formed by thermolysis of AB remains dissolved in the ionic liquid. This is a unique property that has not been reported for any other ammonia borane/ionic liquid pair and that could facilitate the recycling of the material by rehydrogenation of AB. Finally, some ionic liquids with Choline cation show very high hydrogen yields, but IR results indicate that AB thermolysis proceeded through an alternative route with concomitant production of ammonia and borazine gaseous by-products, similar to that happening in organic solvent.

References

- [1] Shaw W.S.; Linehan J.C.; Szymczak N.K.; Heldebrant D.J.; Yonker C.; Camaioni D.M.; Baker R.T.; Autrey T., *Angew. Chem. Int. Ed.* **47** (2008) 7493-7496
- [2] Bluhm M.E.; Bradley M.G.; Butterick R.; Kusari U.; Sneddon L.G., *J. Am. Chem. Soc.* **128** (2006) 7748-7749
- [3] Marsh K.N.; Boxall J.A.; Lichtenthaler R., *Fluid Phase Equilib.* **219-1** (2004) 93-98
- [4] Himmelberger D.W.; Alden L.R.; Bluhm M.E.; Sneddon L.G., *Inorg. Chem.* **48** (2009) 9883-9889
- [5] Basu S.; Zheng Y.; Gore J.P., *J. Power Sources* **196** (2011) 734-740
- [6] Wright W.R.H.; Berkeley E.R.; Alden L.R.; Baker R.T.; Sneddon L.G., *Chem. Commun.* **47** (2011) 3177-3179
- [7] Smitha B.; Sridhar S.; Khan A.A., *J. Membrane Sci.* **259** (2005) 10-26
- [8] Jash P.; Meaux K.; Trenary M., *J. Undergraduate Research* **5** (2012) 1-5
- [9] Pretsch E.; Bühlmann P.; Badertscher M., *Structure Determination Of Organic Compounds*, 4th Edition. Springer, Zürich (2009)
- [10] Hamilton C.W.; Baker R.T.; Staubitz A.; Manners I., *Chem. Soc. Rev.* **38-1** (2009) 279-293
- [11] Peng B.; Chen J., *Energy and Environmental Science* **1** (2008) 479-783
- [12] Weismiller M.R.; Wang S.Q.; Chowdhury A.; Thynell S.T.; Yetter R.A., *Thermochim. Acta* **551** (2013) 110– 117
- [13] Ahosseini A.; Ortega E.; Sensenich B.; Scurto A.M., *Fluid. Phase Equilib.* **286** (2009) 72-78
- [14] Miranda, C.R.; Ceder G., *J. Chem. Phys.* **126** (2007) 1-11

- [15] Sutton A.D.; Burrell A.K.; Dixon D.A.; Garner E.B.; Gordon J.C.; Nakagawa T.; Ott K.C.; Robinson J.P.; Vasiliu M., *Science* **331** (2011) 1426-1429
- [16] Shaw W.J.; Bowden M.; Karkamkar A.; Howard C.J.; Heldebrandt D.J.; Hess N.J.; Linehan J.C.; Autrey T., *Energy Environ. Sci.* **3** (2010) 796–804

General conclusions

Thermal decomposition of Ammonia Borane (AB) has been investigated in different environments.

1) Chapters 3 and 4 study the thermolysis of AB after recrystallization in two solvents and after impregnation onto different mesoporous materials by incipient wetness impregnation. All these samples were characterized through different techniques and it was observed that:

1.1 Small differences regarding H_2 yield are observed between neat AB and recrystallized AB while some changes in the thermal behavior for AB-Met suggest AB particles suffer some surface transformation.

1.2 The melting temperature seems to be a key parameter for understanding AB thermal decomposition under 100 °C as it seems to be favored in the molten phase in general.

1.3 Structural changes appear much quicker in the case of AB-THF, which melting event proved to be a smaller barrier at 90 °C while they take a little longer for AB-Met and much longer for neat AB. The three materials present the same unique H_2 desorption event at 90 °C and the *operando* Raman-MS results corroborate a nucleation and growth mechanism for AB decomposition samples.

1.4 For Ga_2O_3 -supported AB materials, there is a considerable enhancement in H_2 desorption properties in terms of lowered temperature and kinetics for the 0.5:1 AB/ Ga_2O_3 samples in which decomposition proceeds through a one-step mechanism. Dehydrogenation temperature is specially lowered in the case of AB/ Ga_2O_3 0.5:1 (Met). All the AB/ Ga_2O_3 materials induce NH_3 desorption simultaneously to dehydrogenation during thermal decomposition which may be caused by interactions between the support surface and AB molecules.

1.5 When AB loading level is raised to 1:1, thermal properties of AB depend on which support it is used. For mesoporous Ga_2O_3 which pores volume is limited and microporous CoAPO-5 with poor intercrystalline mesoporosity, H_2 desorption performance are very similar to those from neat AB with some subtle improvements regarding the onset temperature for the first dehydrogenation step or the release of impurities despite some NH_3 desorption detected for AB-Ga.

1.6 For SBA-15 materials which possess highly ordered mesopores distribution, very important improvements are obtained. A single H₂ release peak at temperatures significantly lower and very different Raman spectra indicate a change in the mechanism of decomposition of AB that may be induced by all the impregnated AB being confined into the bigger pores of SBA-15 supports which porosity is more accessible than for CoAPO-5 and Ga₂O₃. No impurities release is observed. These effects are very similar to those obtained in chapter 3 for Ga₂O₃ with an AB loading level of 0.5:1.

2) In chapter 5, the thermal decomposition of ethane 1,2-di-amineborane (EDAB), a derivative compound from AB, is investigated. EDAB samples have been successfully synthesized as shown by structural and bonding properties characterization. The thermolysis of EDAB has been investigated by calorimetric and vibrational spectroscopic methods which show that EDAB samples exhibit thermal stability higher than that of AB with purer release of H₂. Finally, the *operando* Raman-MS and NMR studies of the thermolytic decomposition of EDAB defines the bonding properties of the reaction products and propose a reaction scheme for the thermolysis of EDAB which proceed through an initial dimerization of EDAB molecules, which subsequently polymerize forming larger chains. Subsequent formation of BH₂ cyclic groups and double B=N bonds as temperature increases give rise to the second hydrogen release step.

3) Finally, chapter 6 studies the release of hydrogen by thermolysis of AB dissolved in 13 different ionic liquids. In most cases, the results observed are similar to those obtained in the study of ammonia borane solutions in bmimCl ionic liquids and reported in previous works: a drastic reduction of the induction time with a slight increase of the hydrogen yield. Furthermore, foaming problems and formation of a solid residue that is insoluble in the ionic liquid are still observed in general. However, some exceptions are detected:

3.1 In the case of some ionic liquids with bis(trifluoromethylsulfanyl) imide anion, it seems that no foams are formed with greatest enhancement in hydrogen release kinetics.

3.2 In the case of empyTf₂N dissolution, the residue formed by thermolysis of AB remains dissolved in the ionic liquid which is a unique property that has not been reported for any other ammonia borane/ionic liquid pair.

3.3 Finally, some ionic liquids with Choline cation show very high hydrogen yields, but IR results indicate that AB thermolysis proceeded through an alternative route with concomitant

production of ammonia and borazine gaseous by-products, similar to that happening in organic solvent.

Conclusiones generales

Esta tesis estudia la descomposición térmica del borano de amoníaco (AB) en diferentes entornos.

1) En los capítulos 3 y 4, se estudia la termólisis del AB tras ser recristalizado en dos disolventes diferentes y también tras una sucesiva impregnación sobre varios materiales porosos por impregnación húmeda incipiente. Todas estas muestras fueron caracterizadas por medio de varias técnicas y se observó que:

1.1 Leves diferencias en cuanto al rendimiento de H_2 se producen entre el AB másico y recristalizado mientras que algunos cambios en el comportamiento térmico del AB-Met sugieren que las partículas de AB sufren transformaciones superficiales en esta muestra.

1.2 La temperatura de fusión de cada muestra para ser un factor determinante para comprender la descomposición térmica del AB por debajo de $100\text{ }^{\circ}\text{C}$ ya que parece que este fenómeno se ve favorecido tras la fusión en general.

1.3 Los cambios estructurales detectados por espectroscopía Raman se observan mucho más rápido en el caso del AB-THF cuya fusión muestra un pico considerablemente más pequeño por DSC a $90\text{ }^{\circ}\text{C}$. Estos cambios son un poco más largos en el caso del AB-Met y mucho más largos aún en el caso del AB másico. Estos tres materiales presentan un único pico de desorción de hidrógeno a $90\text{ }^{\circ}\text{C}$ y los resultados de Operando Raman-MS corroboran el mecanismo de nucleación y crecimiento para la descomposición térmica de las tres muestras.

1.4 En el caso de las muestras de AB soportado sobre Ga_2O_3 , se produce una mejora considerable de las propiedades de desorción en cuanto a la temperatura que disminuye y la cinética del proceso para las muestras con carga AB:soporte de 1:5 para las que la descomposición procede a través de un mecanismo de una etapa. La disminución de temperatura de desorción es especialmente acusada para la muestra de AB/Ga_2O_3 0.5:1 (Met). Todos los materiales de AB/Ga_2O_3 inducen desorción de NH_3 simultánea a la deshidrogenación durante la descomposición térmica, probablemente debido a interacciones de moléculas de AB con la superficie del soporte.

1.5 Cuando la carga de AB:soporte se eleva a 1:1, las propiedades de descomposición varían según el soporte considerado. En el caso de Ga_2O_3 cuyo volumen de poros es limitado y el de CoAPO-5 que muestra una reducida mesoporosidad intercrystalina, el proceso de deshidrogenación es muy similar al del AB másico a pesar de que se observe una leve disminución de la temperatura umbral de la primera etapa de desorción de hidrógeno y una disminución de impurezas volátiles a pesar de la liberación de NH_3 en las muestras de AB-Ga.

1.6 Para los materiales a base de SBA-15 que ofrecen una distribución de mesoporos muy ordenada, se obtienen importantes mejoras. Se detecta una única desorción de H_2 que comienza a una temperatura que, junto con la distinta evolución de los espectros Raman, indica un cambio en el mecanismo de descomposición del AB que probablemente se deba a que se encuentre confinado en los poros de las SBA-15, mucho más accesibles que los de CoAPO-5 y Ga_2O_3 . No se detectan además impurezas en la corriente efluente. Estos efectos son similares a los que se observaron para las muestras AB/ Ga_2O_3 con carga 0.5:1.

2) En el capítulo, se estudia la descomposición térmica del etano 1,2-di-amineborano (EDAB), un derivado del AB. Las muestras de EDAB se sintetizaron con éxito como demuestran los resultados de caracterización estructural y molecular. Se estudió la termólisis de este compuesto por técnicas calorimétricas y métodos espectroscópicos que demostraron que el EDAB ofrece una mayor estabilidad estructural que el AB y una liberación de hidrógeno más puro. Los resultados de Operando Raman-MS y RMN permitieron definir la naturaleza de los enlaces de los productos de reacción y proponer un mecanismo reacción para la termólisis del EDAB basado en una dimerización inicial de moléculas de EDAB que a continuación polimerizan formando cadenas más largas. Seguidamente se produciría formación de grupos BH_2 cíclicos y enlaces dobles $\text{B}=\text{N}$ al aumentar la temperatura dando lugar a la segunda desorción de hidrógeno.

3) Por último, se estudia en el capítulo 6 la descomposición de AB disuelto en 13 líquidos iónicos diferentes. La mayoría de las muestras daba lugar a resultados similares a los ya descritos en bibliografía para disoluciones de AB en bmimCl con una reducción drástica del periodo de inducción y un aumento del rendimiento de H_2 con respecto al AB másico. Se detectaron además formación de espuma y de un residuo sólido insoluble en el líquido iónico en general. Sin embargo, se encontraron algunas excepciones:

3.1 En el caso de líquidos iónicos que contienen el anión bis(trifluorometilsulfanil) imida, parece que no se forma espuma y se da un mayor aumento de la cinética de liberación de hidrógeno.

3.2 El residuo formado a partir de la disolución de AB en empyTf_2N se queda disuelto en el líquido iónico lo cual no se ha observado hasta el momento para otro par AB/líquido iónico.

3.3 Finalmente, algunos líquidos iónicos con el catión colina muestran rendimientos de hidrógeno mayores que los restantes líquidos iónicos. Los resultados de IR demuestran que para estos materiales, la descomposición térmica transcurre a través de un mecanismo alternativo con liberación de amoníaco y borazina de manera similar a lo que se observa durante la descomposición térmica del AB en disolventes orgánicos.